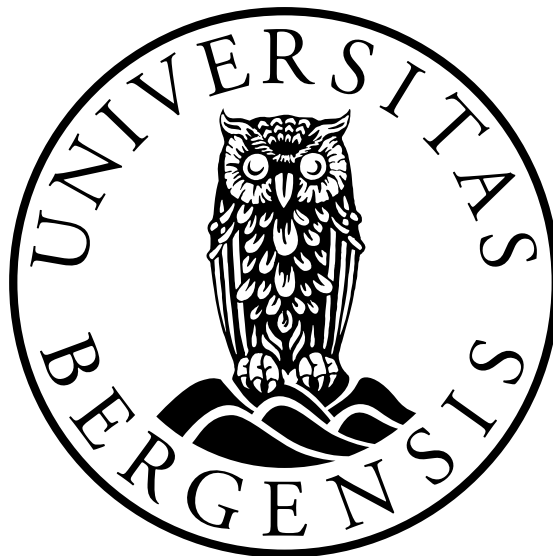


# On the use of a new mathematical formulation for loads- and motion analysis of a mooring line

Petter Veseth



Master's thesis in Energy  
Geophysical Institute  
University of Bergen, Norway

November 20, 2023

©Copyright Petter Veseth

The material in this publication is protected by copyright law.

Year: 2023

Title: On the use of a new mathematical formulation  
for loads- and motion analysis of a mooring line

Author: Petter Veseth

# Acknowledgements

This 60 ECT master thesis is written as a part of the 2-year Masters program in Energy at the Geophysical institute at the University of Bergen. I would like to make a special thank you to my supervisor, professor Cristian Gebhardt, for your support, guidance and help during this project. Your knowledge of wind turbines and Kirchhoff's rods are superior, and I thank you for sharing your wisdom with me. I would also like to make a special thank you to my co-supervisor Bruno Rocca, you always take time to guide and support me when needed. Last but not least, I would like to thank my co-supervisor Marte Godvik. Your input on the industry's perspective has been very helpful.

"Das höchste Ziel, welches die Naturwissenschaften zu erstreben haben, ist die Verwirklichung der eben gemachten Voraussetzung, also die Ermittlung der Kräfte, welche in der Natur vorhanden sind, und des Zustandes, in dem die Materie in einem Augenblicke sich befindet, mit einem Worte, die Zurückführung aller Naturerscheinungen auf die Mechanik."

"The highest object at which the natural sciences are constrained to aim, but which they will never reach, is the determination of the forces which are present in nature, and of the state of matter at any given moment — in one word, the reduction of all the phenomena of nature to mechanics."

*Gustav Robert Kirchhoff* (1865)

# Abstract

This master thesis investigates the use of a new mathematical model for calculating loads and dynamic motion of a mooring line. Current industry standard mooring analysis tools uses a lumped parameter modelling approach. The new model utilizes an advanced rod model, which in nature is a continuous model able to capture nonlinear behaviour. If this new model succeeds it has the potential to give a better understanding of the loads and dynamics of a mooring line, and can potentially aid in cost-reduction for future floating offshore wind turbine farms. The thesis compares the results from the new model versus a lumped parameter mooring model for a limited number of load cases. This thesis has lead to improvements for the new model, such as introducing a barrier function for seafloor interaction and investigated the FEM discretization form, which has improved the new models capability to be used for mooring line analysis tool.

# Contents

<b>Acknowledgements</b>	<b>ii</b>
<b>Abstract</b>	<b>iv</b>
<b>1 Introduction</b>	<b>1</b>
1.1 Background . . . . .	2
1.2 Research question . . . . .	3
<b>2 Theoretical Background</b>	<b>5</b>
2.1 Properties of a wind turbine . . . . .	5
2.2 Extraction of energy . . . . .	5
2.2.1 Power curve and power coefficient . . . . .	6
2.3 Support structures for offshore wind turbines . . . . .	7
2.3.1 Bottom fixed wind turbines . . . . .	7
2.3.2 Floating wind turbines . . . . .	8
2.4 Forces on a floating structure . . . . .	9
2.4.1 Equation of motion for a floating structure . . . . .	10
2.5 Properties of mooring . . . . .	11
2.5.1 Catenary shape . . . . .	12
2.5.2 Mooring line materials . . . . .	13
2.5.3 Anchors . . . . .	13
2.6 Model description . . . . .	13
2.6.1 The 15 MW wind turbine . . . . .	14
2.6.2 The VoltturnUS-S sub-body . . . . .	15
2.6.3 Mooring line specification for VoltturnUS-S . . . . .	16
2.7 Mooring analysis . . . . .	16
2.7.1 Static analysis - zero offset . . . . .	17
2.7.2 Quasi-static analysis - static offset . . . . .	17
2.7.3 Dynamic analysis . . . . .	17
2.7.4 Current coupled dynamic analysis tools for FWT . . . . .	18
2.7.5 Lumped parameter modelling approach . . . . .	18
2.7.6 Seafloor contact problem . . . . .	19
2.8 Mathematical properties used in the new advanced model . . . . .	20
2.8.1 Kirchhoff rod theory . . . . .	20
2.8.2 Elastic modulus . . . . .	21
2.8.3 Elastic deformation and hyperelasticity . . . . .	22
2.8.4 Moment of area and inertia . . . . .	22
2.8.5 Lagrangian mechanics . . . . .	23
2.8.6 Equation of motion in Lagrangian configuration . . . . .	24

2.8.7	Finite Element Method . . . . .	26
2.8.8	Isogeometric discretization in FEM solving technique . . . . .	27
<b>3</b>	<b>Methodology</b>	<b>28</b>
3.1	Table of load cases . . . . .	28
3.1.1	Explanation to table . . . . .	29
3.2	Static Solver . . . . .	30
3.2.1	Inelastic catenary equations . . . . .	30
3.2.2	Elastic catenary solver . . . . .	32
3.3	OpenFAST v.3.5.0 . . . . .	34
3.4	Advanced rod model . . . . .	35
3.4.1	From advanced rod model to a mooring line analysis tool . . . . .	35
3.4.2	Mathematical formulation . . . . .	36
3.4.3	Forces in ARM . . . . .	39
3.4.4	Derivation of the barrier function . . . . .	40
3.4.5	Tuning of the barrier function . . . . .	41
<b>4</b>	<b>Results</b>	<b>44</b>
4.1	Static simulation . . . . .	44
4.2	Model verification in OpenFAST . . . . .	47
4.2.1	Load case 1 to 6 - Natural frequencies and damping ratio's . . . . .	47
4.3	Simulations for comparison of OpenFAST and ARM . . . . .	49
4.3.1	Load case 7 - dynamic relaxation . . . . .	49
4.3.2	Load case 8 - Step-wind . . . . .	53
4.3.3	Load case 9 - rated wind speed without waves . . . . .	55
4.3.4	Load case 10 - rated wind speed with waves . . . . .	63
4.3.5	Load case 11 - 50-year EWM . . . . .	67
<b>5</b>	<b>Conclusion and future work</b>	<b>71</b>
5.1	Conclusion . . . . .	71
5.2	Future work . . . . .	72
<b>A</b>	<b>Mathematical derivation of the new advanced model</b>	<b>73</b>
A.1	Mass operator . . . . .	73
A.2	Strain Operator . . . . .	74
A.3	Equation of motion . . . . .	77
<b>B</b>	<b>OpenFAST</b>	<b>78</b>
B.1	Filestructure for OpenFAST simulation . . . . .	79

# List of Figures

1.1	Predicted growth in offshore wind, adapted from DNV report ( <i>DNV, 2022</i> ). . . . .	1
1.2	Wind turbine growth in size, adapted from Wind Europe statistics. . . . .	2
2.1	Curves for the IEA 15MW wind turbine. . . . .	6
2.2	Most common substructures for bottom fixed. A: Gravity-based, B: Monopile, C: Tripod, D: Jacket . . . . .	7
2.3	Different mooring systems for FWT. A: Ordinary catenary mooring. B: Tension leg mooring. . . . .	8
2.4	DOF for a FWT . . . . .	8
2.5	Forces on a FWT, adapted from <i>Silva et al. (2021)</i> . . . . .	9
2.6	ICE quasi-static simulation showing platform horizontal offset -40m to +40m in 10m steps. . . . .	11
2.7	a) Catenary curve for a selection of steepness coef. b) Comparing a catenary and a parabolic curve. . . . .	12
2.8	Various mooring line materials. a) Studless chain, b) Studded chain, c) Example of the cross section of steel wire rope, d) Example of synthetic fibre rope. Courtesy: Lankhorst Gama98. . . . .	13
2.9	Mooring setup for the VoltturnUS-S . . . . .	15
2.10	Lumped mass schematic . . . . .	19
2.11	MAP++ line definitions with seafloor contact, courtesy NREL/MAP++. . . . .	19
2.12	MoorDyn vertical spring-dampener approach. . . . .	20
2.13	Sketch showing different elastic modulus. Adapted from <i>agilescientific.com</i> . . . . .	21
2.14	Stress-Strain relationship for elastic and hyper-elastic deformation. . . . .	22
2.15	Example of 2 <sup>nd</sup> moment of area. . . . .	23
2.16	Example of moment of inertia. . . . .	23
2.17	Sketch of a pendulum swinging. . . . .	25
3.1	Figure showing the static inelastic solution for line 1. . . . .	32
3.2	Flowdiagram showing the ICE procedure. . . . .	33
3.3	Figure showing the comparison between ICE and OpenFAST for mooring line 1. . . . .	33
3.4	OpenFAST Modules, adapted from NREL / OpenFAST. . . . .	34
3.5	Simple drawing showing the original configuration and the deformed configuration. . . . .	37
3.6	Comparison of OpenFAST static results and ARM hinged at fairlead and at anchor. . . . .	41
3.7	Comparison of barrier functions, original and alternative 1 and 2. . . . .	42
3.8	Comparison of barrier functions effect on line distribution. . . . .	43
4.1	Static solvers, with distance between nodes on right axis. . . . .	45



4.2	Static solvers, with distance between nodes on right axis. Increased polynomial degree. . . . .	46
4.3	Natural frequencies and damping ratio for 6 DOF . . . . .	48
4.4	OpenFAST results. . . . .	50
4.5	Comparison of 4 different ARM simulations with same force input. . . . .	51
4.6	Comparison of OpenFAST results versus ARM with org. discretization and increased polynomial degree. . . . .	52
4.7	Step-wind platform motion and turbine response from OpenFAST simulation of load case 8. . . . .	53
4.8	Platform motion with step-wind only. . . . .	54
4.9	Nodal comparison for load case 8, node 140 position over time. . . . .	54
4.10	Nodal comparison for load case 8, fairlead position over time. . . . .	55
4.11	Platform motion with wind only. . . . .	56
4.12	MoorDyn mooring line distribution from load case 9. . . . .	57
4.13	ARM mooring line distribution from load case 9. . . . .	57
4.14	Nodal comparison for load case 9, node number 150. . . . .	58
4.15	Nodal comparison for load case 9, fairlead. . . . .	58
4.16	OpenFAST line tension variation, lines 1 through 3. . . . .	59
4.17	ARM line tension variation, lines 1 through 3. . . . .	59
4.18	ARM line tension variation, increased frequency, lines 1 through 3. . . . .	60
4.19	Figure showing noise on tension data from ARM. . . . .	60
4.20	Low pass filtering, cutoff at 1 Hz. . . . .	61
4.21	The results from the Butterworth filtering. . . . .	61
4.22	ARM line tension variation, lines 1 through 3. . . . .	62
4.23	Platform motion with wind and waves. . . . .	63
4.24	MoorDyn mooring line distribution from load case 10. . . . .	64
4.25	ARM mooring line distribution from load case 10. . . . .	64
4.26	Nodal comparison for load case 10, node number 150. . . . .	65
4.27	Nodal comparison for load case 10, fairlead. . . . .	65
4.28	OpenFAST line tension variation, lines 1 through 3. . . . .	66
4.29	ARM line tension variation filtered, lines 1 through 3. . . . .	66
4.30	Platform motion with wind and waves, EWM 50-year model. . . . .	67
4.31	MoorDyn mooring line distribution from load case 11. . . . .	68
4.32	ARM mooring line distribution from load case 11. . . . .	68
4.33	Nodal comparison for load case 10, node number 150. . . . .	69
4.34	Nodal comparison for load case 10, fairlead. . . . .	69
4.35	OpenFAST line tension variation, lines 1 through 3. . . . .	70
4.36	ARM line tension variation, lines 1 through 3. . . . .	70
B.1	Sketch of OpenFAST capabilities, courtesy of NREL . . . . .	78
B.2	Flow diagram of the filestructure and modules of OpenFAST, courtesy of NREL	79

# Chapter 1

## Introduction

The world needs to switch to renewable energy, and offshore wind energy has the potential to become one of the main energy suppliers in the near future. More and more countries recognize the need to reduce their CO<sub>2</sub> emissions. For example, the European commission has introduced the European Green Deal, in which all 27 members have committed to become the first climate neutral continent by 2050. To reach this goal, the member countries pledged to reduce emissions by at least 55% by 2030, compared to 1990 levels (*EU Commission, 2018*). One important factor in reducing CO<sub>2</sub> emission is to switch the electric energy production from fossil fuel to renewable energy. The current installed capacity of offshore wind turbines in the EU is 14.6 GW (*EU Commission, 2020*). To reach climate neutral by 2050, another 275 GW needs to be installed in the EU alone (*EU Commission, 2020*), and if including Norway and Uk, the total capacity required in 2050 would be 450 GW.

The DNV report (*DNV, 2022*) predicts a growth in the global offshore wind energy production from 29 GW in 2019 to 1748 GW in 2050, as shown in figure 1.1. DNV expects that floating offshore wind will contribute with 264 GW, or 15% of the total offshore wind energy, in 2050. 264 GW is equivalent to 3000 HyWind Tampen farms, which is currently the worlds largest floating offshore wind farm at 88 MW (*Equinor, 2023*).

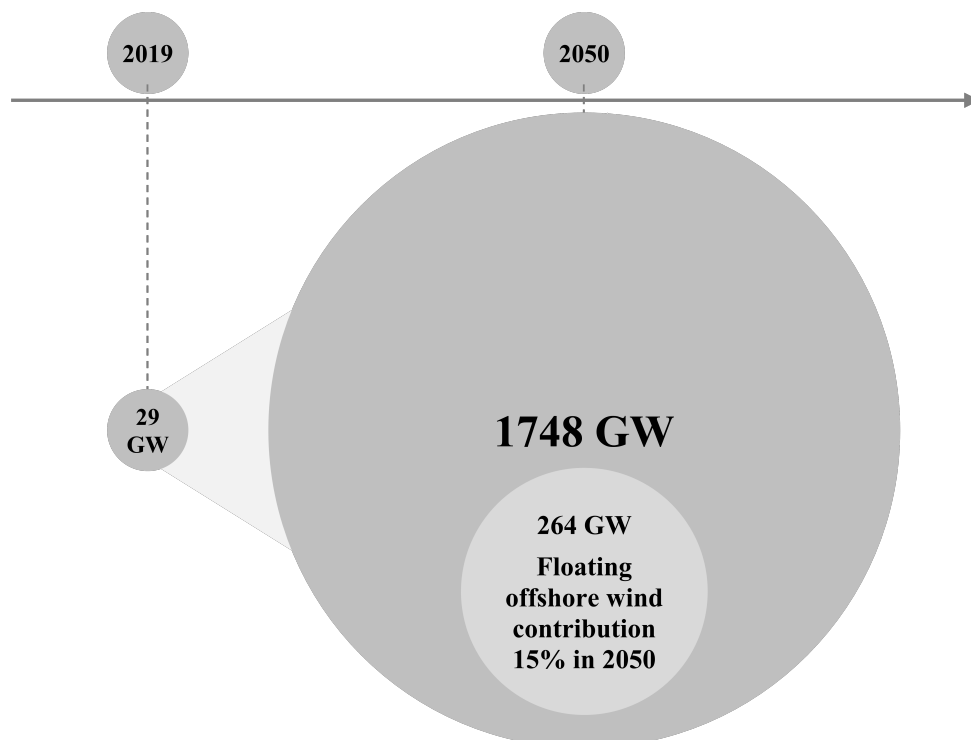


Figure 1.1: Predicted growth in offshore wind, adapted from DNV report (DNV, 2022).

## 1.1 Background

Mankind has for a long time harvested kinetic energy from wind. The first wind turbines were made to grain corn or transport water. Later wind turbines were made to generate electric power. Since the start of electricity production by wind energy in 1883, (*Leonhardt*, 1883), the wind turbines have continuously grown in size and power. Figure 1.2 shows how the turbine size has evolved during the last 40 years, and what is expected in near future.

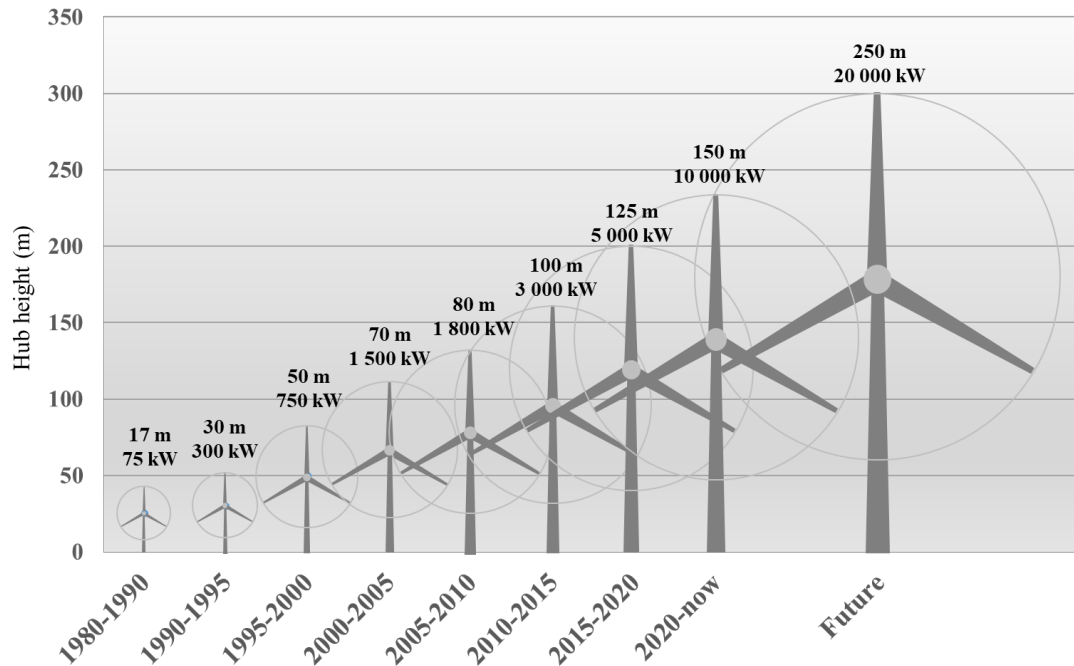


Figure 1.2: Wind turbine growth in size, adapted from Wind Europe statistics.

In 1991 the first offshore wind turbine was installed, at Vindeby in Denmark (*Ørsted*, 2019). It was first thought of as ludicrous to install turbines at sea due to the harsh environment. A few years later this all changed, as it could be shown that offshore turbines produced more energy compared to their onshore siblings due to better wind conditions. Through the Vindeby project and later offshore wind projects it was shown that offshore wind turbines has a higher capacity factor,  $C_f$ , than onshore turbines. This is supported by Wind Europe's annual report for 2020 (*WindEurope*, 2021), which shows an average onshore wind capacity factor of 25% and average offshore wind capacity factor of 42%.

There exists a large number of bottom-fixed offshore wind farms, where the largest ones have more than 170 wind turbines (*Ørsted*, 2022) covering an area of 407 km<sup>2</sup>. Existing wind farms using floating wind turbines (FWT) are still small, typically ranging from 3 to 11 FWT (*Equinor*, 2023). Even though the cost of installation and maintenance is higher for offshore wind turbines compared to onshore wind turbines, the increased capacity factor yields a higher return in energy.

According to ESMAP (Energy Sector Management Assistance Program) there is potentially over 71 TW of technically extractable wind power offshore, but most of this (70%) is on deeper waters, requiring floating technology (*WBG ESMAP*, 2023a). For Norway ESMAP estimates the potential extractable offshore wind power to 1467 GW, whereas 1416 GW (96%) from FWT (*WBG ESMAP*, 2023b).

As previously mentioned, the wind turbines are continuously growing in size. A wind turbine with an increased rotor size will be able to harvest more energy, since the energy captured is proportional to the square of the rotor diameter. That means that doubling the diameter,

quadruples the power capacity. The increase in size has also generated some logistics challenges. Transportation of rotor blades in lengths of more than 50m is extremely difficult and time-consuming on land. For offshore wind turbines, transportation is much simpler, since the rotor blades can quite easily be transported as deck cargo on boats. This means offshore wind turbines can easily accommodate larger rotor size.

## 1.2 Research question

In light of the required turn in energy production towards renewable energy, it is important to reduce the cost of renewable energy to make it more competitive versus fossil fuels. I believe that floating offshore wind turbines have the potential to become a major clean energy producer if the LCOE can be reduced. Along this path, *Bjoerni et al. (2023)* showed that for the Equinor project, TrollVind, the LCOE would be  $\approx 100\$ / \text{MWh}$ . Today, this is too high compared to for example natural gas, which is  $\approx 40\$$  (*Us Energy Information Administration, 2022*).

One of the induced costs due to the nature of FWT is mooring lines. In this master thesis, I will investigate the use of a rather new rod model based on a nonlinear torsion-free and shear free Kirchhoff rod model (*Gebhardt and Romero, 2021; Romero and Gebhardt, 2020*) for static and dynamic analysis of mooring lines. Due to the formulation of this new model, it has the potential to reach a better understanding of the loads and motion response that a mooring line will undergo for a given scenario. Norway's Prime Minister, Jonas Gahr Støre, announced on May, 11<sup>th</sup>, 2023 that Norway aims to allocate 30 GW of offshore wind capacity by 2040. If estimating a  $C_f$  of 0.5, this would produce 131.4 TWh, which is almost as much new electricity as Norway consumes annually today. Even if only half of this will be FWT, it will require a huge amount of mooring lines, and if it is possible to reduce the cost of each mooring line, even by a small fraction, it will contribute to great cost-savings.

The modeled FWT in my master thesis utilizes 3 studless chain mooring lines. Each with a length of 850m and weight pr. meter of 685 kg. This is equivalent to  $\approx 1750$  tons of steel. If by using an advanced rod model it can be shown that the chain size, or chain length, can be reduced while still keeping the loads within the required safety region, it will yield large savings in both steel quantity and cost for handling and installing the mooring lines.

### Thesis overview

My thesis will attempt to utilize a new advanced rod model to study the static and dynamic loads and positional data of mooring lines. To do this, I will use OpenFAST simulation tool to simulate the movement of a floating wind turbine for a selection of different wind and wave conditions as described in table 3.1. The results from the simulations will be used as input data in the new advanced rod model, and also for comparison.

### Aim

The aim of this thesis is to investigate whether a new rod model can give an increased insight in a mooring line's dynamic loading and motion. To achieve this, I will use a new advanced rod model based on the work by (*Gebhardt and Romero, 2021; Romero and Gebhardt, 2020*). The model is a special case of the Kirchhoff rod model. Mooring lines are large contributors to the cost of floating wind turbines, and if new analysis methods are able to reduce the cost of these, it can contribute to development of large commercial farms of floating wind turbines in the future.

**Objective**

I will use OpenFAST simulation software to simulate the motion of a floating wind turbine. The turbine considered will be subjected to a reduced number of load cases with different wind and wave conditions. Then, the force at the fairlead will be transferred as an input for the new advanced rod model, which will be used to calculate the dynamic behavior and the corresponding loads of the mooring lines. Moreover, the loads on the mooring lines will be compared to those provided by OpenFAST for the sake of verification.

**Contribution**

This thesis contributes on a personal level to increase my knowledge of simulation tools (OpenFAST, Matlab) and also my knowledge of analysis tools (Python, Matlab). In addition, it contributes to increase my understanding of the complexity in mooring analysis. On a general level, this thesis provides insight in the use of an advanced rod model for mooring line analysis, and the use of a barrier function to model the seafloor contact. Comparisons made with a lumped-parameter mooring model gives insights on the performance of the new model.

Parts of the results from this thesis will be presented at the DeepWIND conference in 2024. In addition, some of the results will be included in an article being written for the Journal of marine structures.

# Chapter 2

## Theoretical Background

In this chapter, I will describe the principles used in the mathematical formulation for the new advanced rod model, and also the theoretical background necessary for understanding the dynamics of a floating structure and a mooring line. The mathematical formulation for mooring line modeling proposed in this thesis can potentially be used for all floating structures requiring mooring, but for this thesis the chosen model for simulation will be a floating offshore wind turbine. Hence, I will start by describing the basics of a wind turbine.

### 2.1 Properties of a wind turbine

A typical horizontal axis wind turbine consists of a tower with a rotor nacelle assembly (RNA) on top. It is vital that the tower bottom is securely fastened and that the structure is strong enough to withstand the forces and overturning moments generated by the rotor's interaction with the wind. The RNA consists of a rotor assembly and the nacelle. The rotor assembly is most often designed as 3 blades connected to a hub. The Nacelle contains the gearbox, if not direct drive, the generator, and all control systems. As the wind interacts with the blades, it creates a force on the blades which makes the rotor turn. The rotor is connected to the generator through the main shaft, such that the generator starts spinning, and generates electricity. The RNA usually has the capability to yaw, which means to rotate around the z-axis. This gives the wind turbine the ability to align the rotor directly upwind to maximise the power production. The blades of the turbine will in most cases have the capability to pitch, meaning to adjust the angle of attack to increase or reduce the energy taken from the wind (*Bhattacharya, 2019*). The pitch and yaw controls are part of the control system for the wind turbine. It is important to avoid damage to the wind turbine in strong winds. As the wind speed increases above the "rated wind speed", the blades are pitched to reduce the energy taken from the wind, and keep optimum rotational speed. If the wind speed increases above the maximum for the wind turbine, the controller will shut down the wind turbine by first pitching the blades to  $90^\circ$ , before applying the brakes on the rotor to stop the rotation.

### 2.2 Extraction of energy

The idea of a wind turbine is to take some of the kinetic energy from the wind and turn it into usable energy, nowadays this is electricity. The max power output from a wind turbine is given by the swept area of the blades,  $A$ , the wind speed,  $u$ , and the power coefficient,  $C_p$ . In 1920 Betz found that the maximum power that could be extracted from the wind was  $\approx 59\%$  (*Betz, 1920*). This is called Betz's limit ( $\frac{16}{27} \approx 0.59$ ), and is the highest possible  $C_p$  a wind turbine can have before the wind will be deflected passed the rotor instead of passing through the rotor.

This is due to the fact that the rotor will reduce the wind velocity such that the velocity behind the rotor is too slow to let any more air molecules through, and the remaining molecules will be deflected to pass on the outside of the rotor.  $C_p$  is given by the blade properties, like twist, width and profile. In addition, the controller can adjust the blade pitch to adjust  $C_p$  to the given wind condition.

$$P = \frac{1}{2} \rho_{air} A u^3 \cdot C_p \quad (2.1)$$

Equation 2.1 shows how the power output of a wind turbine can be calculated, where  $P$  is the power output and  $\rho_{air}$  is the density of the air, usually  $1.225 \text{ kg/m}^3$ .

The location or site that the wind turbine is installed is important for the energy production. Each site has different wind conditions, and it is vital to match the site with the wind turbine design. The capacity factor,  $C_f$ , is the ratio between the maximum energy a turbine can generate in a year and the actual energy production. It is a value describing both wind conditions for a site and how well it is matched with the wind turbine installed.

$$C_f = \frac{\text{Annual energy production [kWh]}}{P[\text{kW}] \cdot 8760[\text{h}]} \quad (2.2)$$

This means that two identical wind turbines installed at different sites will not necessarily produce equal amount of energy during a year. The wind conditions at the given site is very important.

## 2.2.1 Power curve and power coefficient

A specific wind turbine will be designed with a specific max power output. This max power output is achieved at what is called rated wind speed. Wind turbines will require a certain wind speed before it will start to generate power, this is called cut-in wind speed. Wind turbines also have a maximum wind speed for which it can generate electricity, called cut-out wind speed. For wind speeds below cut-in and above cut-out wind speed, the wind turbine will be in idling mode, and not generating electricity. Power curve for the IEA 15MW wind turbine is shown below in figure 2.1a. Note that as the wind speed increases above the rated wind speed, no extra power is generated, due to limitations in the generator. Instead, the controller pitches the blades which reduces the thrust force. Figure 2.1b shows the power and thrust coefficients for the IEA 15MW wind turbine, while the blue line is representing Betz's limit (Gaertner *et al.*, 2020).

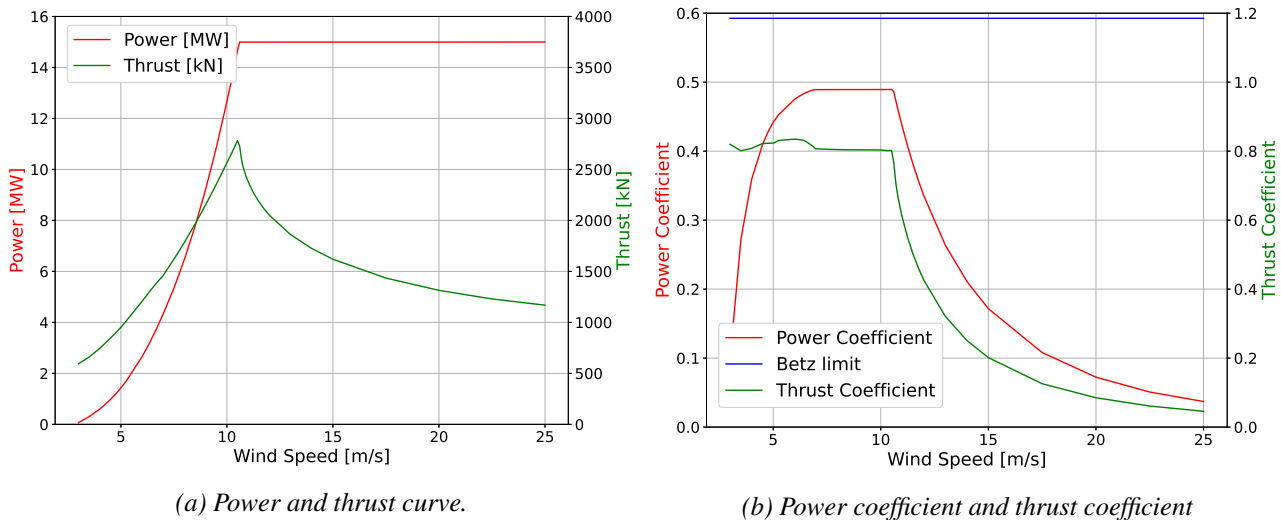


Figure 2.1: Curves for the IEA 15MW wind turbine.

When the wind speed increases to above the cut-out wind speed for the turbine, the turbine will enter a shut-down mode, pitching the blades to  $90^\circ$  before applying the brakes to stop the rotor.

## 2.3 Support structures for offshore wind turbines

An offshore wind turbine will require a support structure, which will support the tower of the turbine. Different support structures are used, depending on water depth and soil composition.

### 2.3.1 Bottom fixed wind turbines

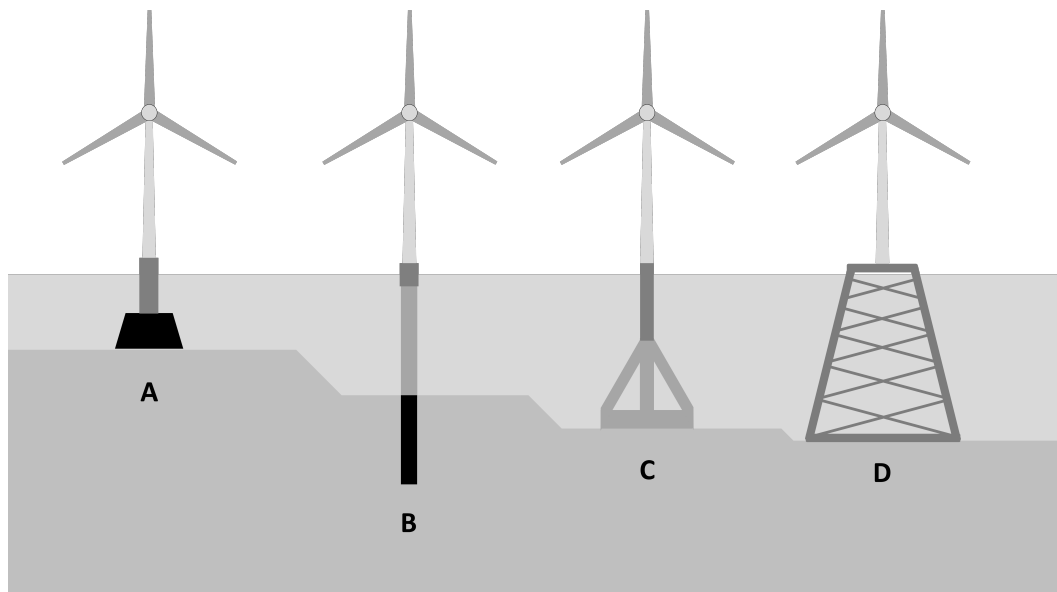


Figure 2.2: Most common substructures for bottom fixed. A: Gravity-based, B: Monopile, C: Tripod, D: Jacket

Most common support structures for bottom fixed wind turbines are monopile and jacket structures, but also gravity based and tripod structures exist, see figure 2.2. A gravity-based foundation, as shown in figure 2.2 A, is a large and heavy concrete structure which sits on the seafloor. The structural stability is provided by the high weight of the foundation. Monopile structure consists of, as the name indicates, one pile which is driven down through the top soil level of the seafloor. The wind turbine is installed on the top of the monopile. Monopile structures are mainly used in shallow water, from 0-30m depth (Bhattacharya, 2019). Typical construction shown in figure 2.2 B. Deeper water requires a structure with increased stability due to induced overturning moment from the turbine. The tripod structure, 2.2 C, has the advantage of a small exposed area at the sea level, similar to the monopile, and an increased structural stability from the three steel beam taking up the tower deflection as compression and tension. A jacket structure, as shown in figure 2.2 D, is a steel-beam structure, usually four legs with cross-beams. A jacket structure can be used for depths up to 60m (Bhattacharya, 2019).



### 2.3.2 Floating wind turbines

Typical substructures for a floating wind turbine, FWT, are spar buoy design and semi-sub design. Both require mooring, and can either be TLP (tension leg) or ordinary catenary mooring. See figure 2.3 for a simplified drawing of both mooring types.

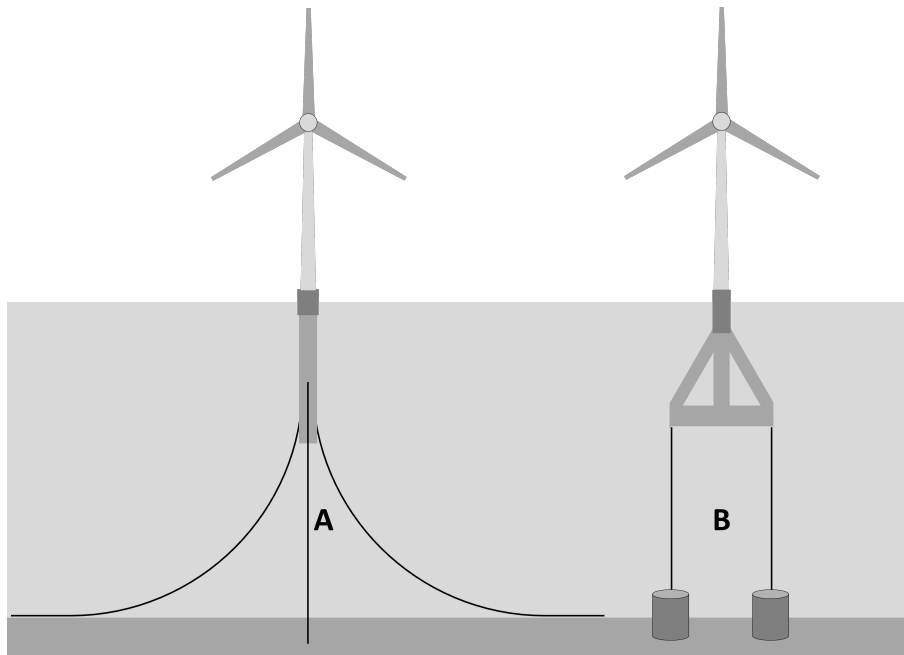


Figure 2.3: Different mooring systems for FWT. A: Ordinary catenary mooring. B: Tension leg mooring.

Floating structures have an increased number of degrees of freedom compared to bottom fixed structures. This is due to the fact that the structure is not secured to the seafloor, but rather hovering in the water. A FWT has six degrees of freedom (DOF). There are 3 DOF for translation and 3 DOF for rotation. The FWT has its centre of rotation at its mass center (*Tran and Kim, 2015*). Figure 2.4 shows the six motions that a FWT can exhibit.

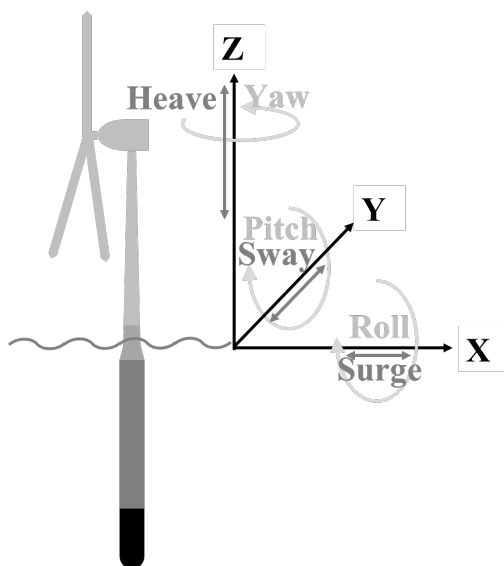


Figure 2.4: DOF for a FWT

Translation	Direction
Surge	X
Sway	Y
Heave	Z
Rotation	About axis
Roll	X
Pitch	Y
Yaw	Z

Table 2.1: Floating structures DOF

## 2.4 Forces on a floating structure

A floating structure is exposed to several forces. In this chapter I will give a brief overview of the different forces.

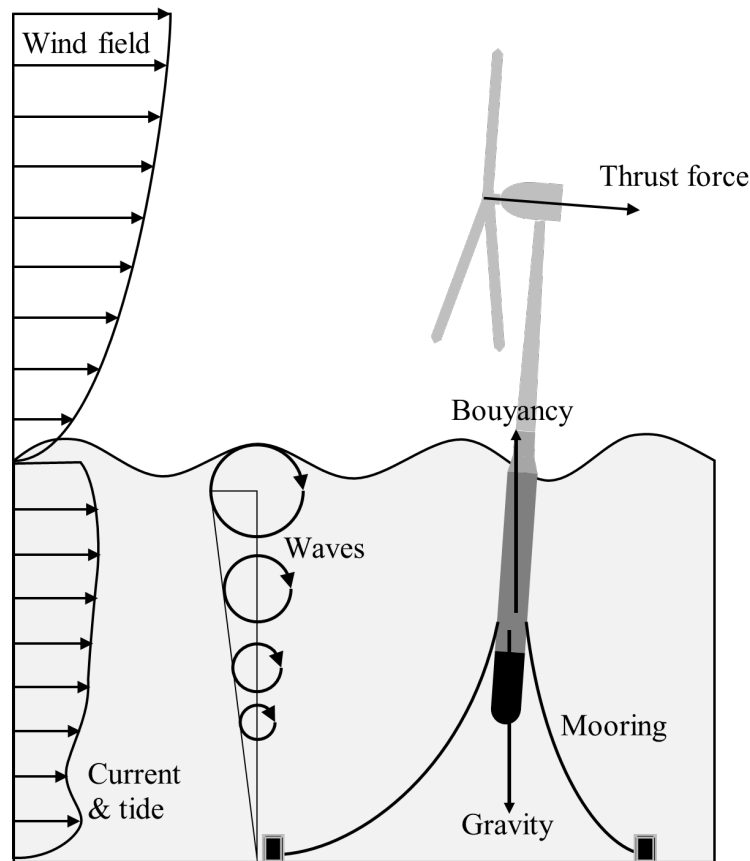


Figure 2.5: Forces on a FWT, adapted from Silva et al. (2021).

Figure 2.5 shows a simplified layout of the forces a floating structure will be exposed to. Buoyancy force,  $F_B$ , is the resultant force of the displaced water of the sub-body trying to push the structure out of the water, while the weight, or gravity force,  $F_G$ , of the complete system acts in opposite direction, towards the center of the earth.

$$F_B = \rho_w g V \quad (2.3)$$

$$F_G = mg \quad (2.4)$$

Here,  $\rho_w$  is the density of water,  $g$  is the gravity constant,  $9.81 \text{ m/s}^2$ ,  $V$  is the volume of displaced water, and  $m$  is the mass of the structure. When  $m = \rho_w V$  the structure will be in hydro-static balance. To have a stable floating structure it is important that the mass center is below the center of buoyancy. This will provide what is called hydro-static restoring force.

Mooring line forces will act in the tangential direction of the lines at the fairleads. The lines will create an added weight to the structure. Mooring lines also contribute to the damping of movement and restoring of the structure, both through geometric damping and through drag induced damping as the line moves in the fluid.

Wave forces can be split into first order and second order. First order force oscillate at the wave frequency, while second order force include both the sum-frequency force which oscillate at twice the wave frequency and the mean-drift force. For calculating wave forces, there are two

dominant theories, strip-theory (ST) and potential flow theory (PF). *Pereyra et al.* (2016) investigated the use of both theories, and concluded that both theories have their strengths and limitations. ST is preferred where the submerged structure has much smaller diameter compared to the wave length, while PF is preferred for larger structures. PF uses the MacCamy-Fuchs diffraction theory (*MacCamy and Fuchs, 1954*). ST utilizes the Morison equation. *Morison et al.* (1950) showed that the wave force can be expressed as two parts, the inertia part and the drag part. The inertia part includes both the Froude-Krylov force, which is the effect of the undisturbed flow, and the effect of the disturbed flow, through the "added mass" coefficient (*Nielsen, 2021*). The "added mass" coefficient,  $C_m$ , depends on the geometry of the sub-body. For floating objects, there is also a concept of relative motion, since the object will not be stationary. This concept is based on the relative velocity and acceleration of the structure with reference to the fluid. Morison equation in 2-D is:

$$F_x^{(2D)} = \underbrace{(1 + C_m)\rho\pi R^2\dot{U}}_{\text{Inertia part}} + \underbrace{\frac{1}{2}\rho C_d 2R(U - \dot{x})|U - \dot{x}|}_{\text{Drag part}} \quad (2.5)$$

where  $\dot{x}$  is the velocity of the structure,  $\rho$  is the density of water, normally  $1025 \text{ kg/m}^3$ ,  $R$  is the radius of the cylinder,  $U$  is the velocity of the fluid,  $\dot{U}$  is the fluid acceleration and  $C_d$  is the drag coefficient, which is dependent on the geometry of the structure. Morison equation is applied for strips of the submerged body, and includes both first- and second order wave forces. The 2-D Morison equation 2.5 is then integrated over the height of the structure to find the total force.

Ocean current and tidal current will create a drag-force on the sub-body, and also on the mooring lines. The current effect can be included in the Morrison equation for wave force by including the current velocity in the expression for  $U$ .

Wind interacting with the turbine blades will create both drag and lift forces. The resultant thrust force will act at the hub center, in the direction of the wind. A fraction of the thrust force will generate torque on the shaft of the wind turbine, defined by the lift and drag force of the blade element. There are several aerodynamic theories used for analysing wind interaction with blades. The simplest is actuator disc theory, or also called the momentum theory (*Dixon, 1998*). The momentum theory can be further evolved to include the wake rotation which is generated as the wind interacts with the rotating blades. This theory is called the blade element momentum theory, because it looks at each radial element of a blade as an aerofoil (*Dixon, 1998*). The BEM theory is the current industry standard aerodynamic formulation and is also used in OpenFAST's AeroDyn module (*Jonkman et al., 2015*).

$$F_T = \frac{1}{2}\rho_{air}A_dV_\infty^2C_T \quad (2.6)$$

Equation 2.6 refers to the thrust force,  $F_T$ , calculated from the actuator disc theory. Here,  $\rho_{air}$  is the density of air,  $A_d$  is the swept area of the rotor,  $V_\infty$  is the velocity of the wind far upstream of the wind turbine, and  $C_T$  is the thrust coefficient. In addition to the thrust force, the wind will generate a cyclic drag force on the tower, due to the turbine-blades rotating. Every time the tower is in the shadow of a blade, the force will be reduced.

In real life, the wind speed will not be constant, but include a certain level of turbulence. Due to turbulence the wind force on the blades and tower are not constant.

### 2.4.1 Equation of motion for a floating structure

For a linearized system with 6 DOF, the equation of motion can be expressed as:

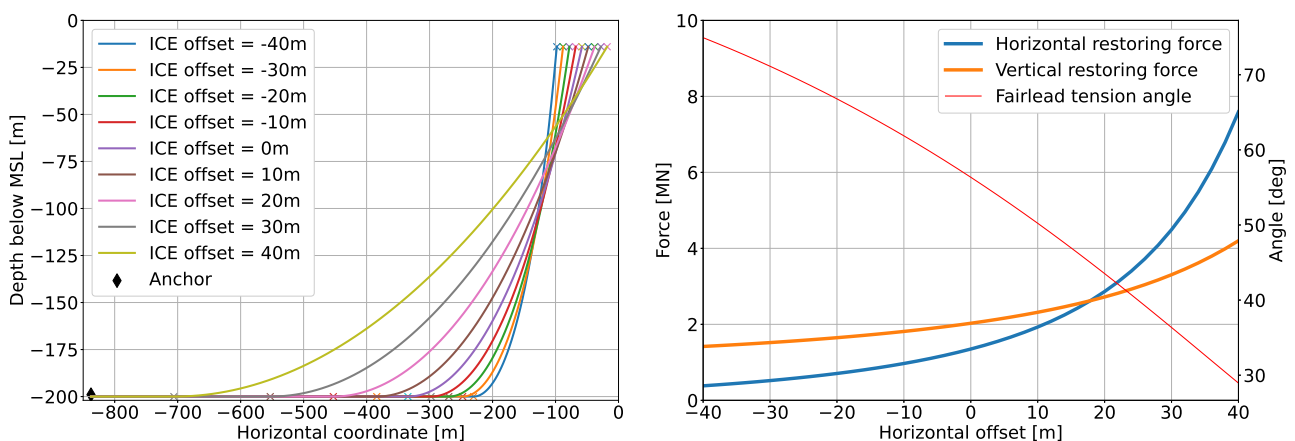
$$(\mathbf{M} + \mathbf{A})\ddot{\eta} + (\mathbf{B}_v + \mathbf{B}_r)\dot{\eta} + (\mathbf{C}_m + \mathbf{C}_h)\eta = \mathbf{F}_{wa} + \mathbf{F}_{wi} + \mathbf{F}_{cu} + \mathbf{F}_{wt} \quad (2.7)$$

where  $\mathbf{M}$  and  $\mathbf{A}$  are the dry mass and added mass matrices,  $\mathbf{B}_v$  and  $\mathbf{B}_r$  are damping matrices, and  $\mathbf{C}_m$  and  $\mathbf{C}_h$  are mooring and hydro-static restoring matrices respectively (Nielsen, 2021). For a 6 DOF system, these matrices will be of size 6x6, where the off-diagonal terms are the coupling terms.  $\eta$  is the positional offset,  $\dot{\eta}$  is the velocity while  $\ddot{\eta}$  is the acceleration. On the right hand side of the equation are the excitation forces due to waves, wind, current and the wind turbine itself.

## 2.5 Properties of mooring

The main reason for mooring of a floating structure is station keeping, to keep the floating structure within an accepted area under specific environmental conditions. (Ma *et al.*, 2019). A complete mooring system is made up of anchors, mooring lines, connectors at the structure and tension equipment. Today, there exists two main types of mooring systems, catenary mooring and TLP mooring. A typical TLP mooring system requires the use of a suction pile anchor connected to a high tensile wire connected to the installation. The system is pretensioned to reduce the movement capability of the system, and to increase stiffness.

A typical catenary mooring system includes a drag embedment anchor (DEA), to take up horizontal forces from the mooring line at seafloor, a mooring line, either chain or a combination of chain and steel / nylon wire, connected to the installation. The line will pass the fairleads, which guides the line towards the tension equipment, usually an anchor winch. For catenary mooring, it is critical that the touchdown point never approaches the anchor, even under extreme loads, as most anchors are only able to take up horizontal forcing. It is important that the mooring system is sufficiently strong such that it can withstand the average forces and the slowly varying forces at the same time (Nielsen, 2021). It is also required to withstand extreme loads due to dynamic offset. If the structure is offset in any direction by external forces, the mooring system will attempt to restore its position. The restoring force from the mooring system, also called the force versus displacement characteristic is a non-linear relationship with the offset distance. Figure 2.6a shows how the line is lifted from the seafloor as the fairlead is moved horizontally. As the fairlead is horizontally offset from 0 to 40m, the touchdown point (TD) of the line is shifted approximately 350m. Figure 2.6b shows the non-linear relationship between platform horizontal offset and both the horizontal and vertical force component from the mooring line. With 40m horizontal offset, the horizontal restoring force increases by approximately 400%. The below figures were generated using my own developed inelastic catenary solver, described in chapter 3.2.2.



(a) Line distribution with various surge offset, line 1.

(b) Horizontal force, vertical force and angle at fairlead.

Figure 2.6: ICE quasi-static simulation showing platform horizontal offset -40m to +40m in 10m steps.

## 2.5.1 Catenary shape

The name "Catenary mooring" comes from the catenary shape, which is the shape of a line as it hangs freely between two points. In the case of mooring, one end is located at the fairlead, while the other end is located at the touchdown point at seafloor. Jacob Bernoulli accidentally stumbled upon the catenary problem in 1690, and found that it had not been mathematically described. He started a contest to find the profile of a free hanging flexible cord. Leibniz, Huygens and Johann Bernoulli all found the equation for a catenary separately, and published their work in 1691 (Sepideh, 2020). The catenary formulation shapes a magical curve, which has been used in construction of bridges, buildings, ships and ocean platform mooring.

For a free hanging line, the horizontal force,  $F_H$  will be constant throughout the length of the line, while the vertical force,  $F_V$ , increases as a function of the line length. The tension,  $T$  at any point on the line will be the vector sum of the forces.

$$F_H(s) = F_H \quad (2.8)$$

$$F_V(s) = \omega_0 \cdot g \cdot s \quad (\text{For } s \in [0, S]) \quad (2.9)$$

$$T(s) = \sqrt{F_H^2 + F_V^2} \quad (2.10)$$

Here,  $\omega_0$  is the weight of the line pr. meter,  $g$  is the gravity constant, and  $s$  is the coordinate of the point on line.

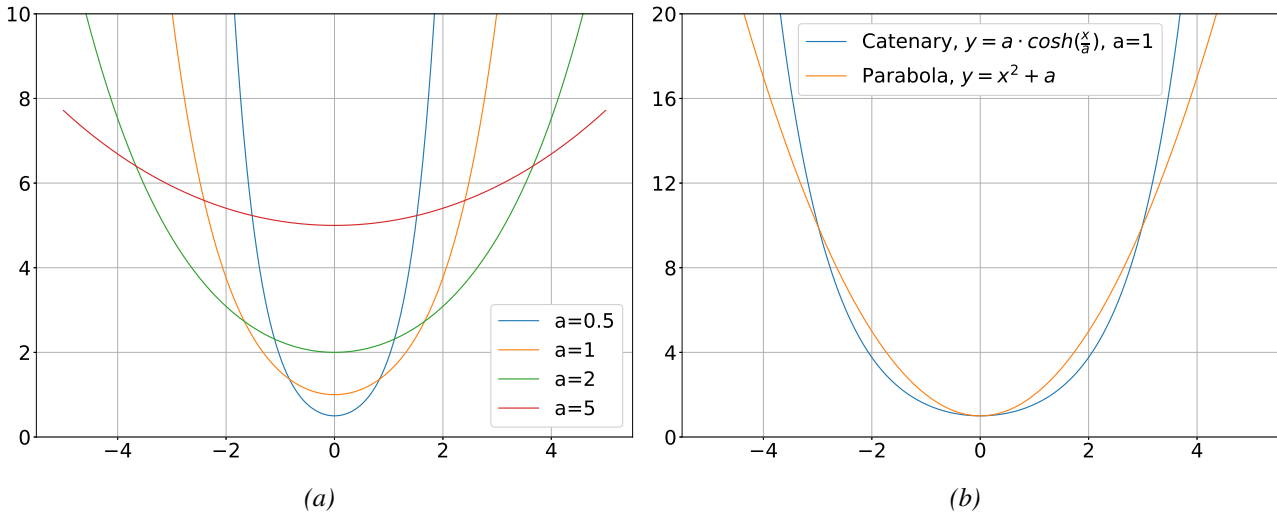


Figure 2.7: a) Catenary curve for a selection of steepness coef. b) Comparing a catenary and a parabolic curve.

The curve of the catenary has the shape of a U, and can resemble the parabolic curve, but it is not, as shown in figure 2.7b. The catenary curve has the shape of a hyperbolic cosine function. The below equation 2.11 defines the curve of the catenary, where  $a$  is the steepness coefficient,  $p$  is the unstretched line, and  $s$  is the stretched line.

$$y = a \cosh\left(\frac{x}{a}\right) = \frac{a}{2} \left( e^{\frac{x}{a}} + e^{-\frac{x}{a}} \right) = \sqrt{a^2 + s^2} = \sqrt{a^2 + p^2} + \frac{H}{2EAa} p^2 \quad (2.11)$$

Figure 2.7a compares different catenary shapes for various steepness coefficients. The stretched length,  $s$ , is stretched according to Young's modulus,

$$s = \left( 1 + \frac{T}{EA} \right) p \quad (2.12)$$

If neglecting stretch,  $EA \rightarrow \infty$ , will lead to  $s = p$ . For more information on Young's modulus, see chapter 2.8.2.

## 2.5.2 Mooring line materials

Mooring lines can be made in several different materials and design, and has different properties.

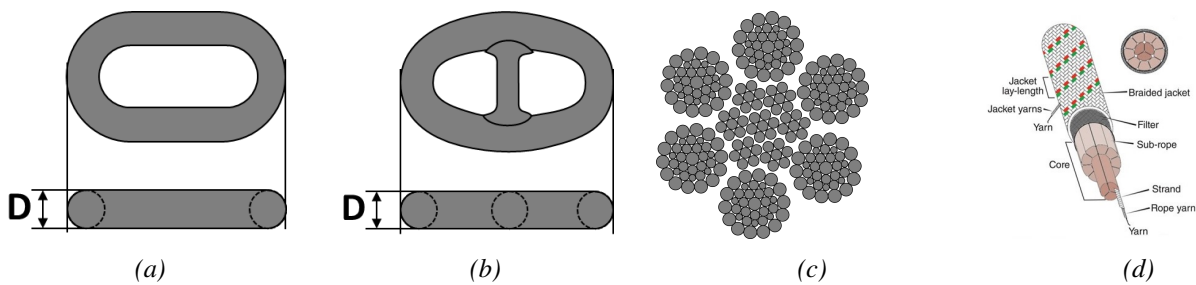


Figure 2.8: Various mooring line materials. a) Studless chain, b) Studded chain, c) Example of the cross section of steel wire rope, d) Example of synthetic fibre rope. Courtesy: Lankhorst Gama98.

The studless chain, shown in figure 2.8a, is the most commonly used mooring line material, and has high breaking strength and corrosion resistance as its advantages. The high weight and cost are two disadvantages. The studded chain, figure 2.8b, has even higher breaking strength compared to studless, but cost and weight is also higher. For both studded and studless chain, **D** is the nominal chain diameter. A mooring line from a combination of materials is also a possibility. By using chain for the top part of the mooring line connected to the fairlead, and for the bottom part connected to the anchor, and either steel wire, figure 2.8c, or synthetic rope, figure 2.8d, for the middle part, will reduce the total weight of the mooring line dramatically, and make it possible to use catenary mooring for deep water operations. It is important though, that the synthetic rope or steel wire does not come in contact with the seafloor, as the friction induced wear will damage the material and lead to a premature failure of the mooring line (*Ma et al.*, 2019).

## 2.5.3 Anchors

For catenary mooring, drag embedment anchors (DEA) are most commonly used. These have a hook-like arrangement at the back end, which will force its way down the soil to increase the anchors ability to withstand horizontal forcing. Depending on the soil characteristic, a high-efficiency DEA can potentially hold 20-90 times its own weight (*Ma et al.*, 2019).

For TLP mooring, suction anchors or gravity anchors are the most commonly used anchors. Suction anchors are cylindrical "buckets" placed on the seafloor. The water from inside the cylinder is pumped out. This creates a suction, which forces the cylinder into the soil. Gravity anchors can be used where the soil is not suitable for suction anchors, and are held in place by gravity only, as the name suggests.

## 2.6 Model description

For the simulations performed in OpenFAST I decided to use the IEA 15MW wind turbine on the VolturnUS-S sub body. The reason for choosing this model is the offshore wind industry's increased interest in semi-submersible sub-structures, like Odfjell's Oceanwind (*Odfjell*, 2023), and the current trend in ever growing wind turbine size, where 15 MW seems to be the new normal.

## 2.6.1 The 15 MW wind turbine

NREL, National Renewable Energy Laboratory, together with DTU, Technical University of Denmark and the IEA, have designed a 15 MW wind turbine (*Gaertner et al.*, 2020), which I will use for the simulations in my master thesis. IEA, International Energy Agency, is an international collaboration for renewable technology, and the IEA Wind TCP, Technology Collaboration Program, is the technology and research sharing program between the member countries. The IEA 15MW wind turbine has the following specifications:

Parameter	Value
Power rating	15 MW
Turbine class	IEC Class 1B
Number of blades	3
Rotor diameter	240 m
Hub height	150 m
Cut-in WS	3 m/s
Rated WS	10.59 m/s
Cut-out WS	25 m/s
Minimum rotor speed	5 rpm
Maximum rotor speed	7.56 rpm
Maximum tip speed	95 m/s
RNA Mass	991 t
Tower Mass	1,263 t

Table 2.2: Specification of the IEA Wind 15MW reference wind turbine

In table 2.2 it can be seen that the IEA 15MW turbine is classified as a turbine Class 1B. The basic parameters for the wind turbine classes are specified in table 2.3, where  $V_{ref}$  represents the reference wind speed averaged over ten minutes and  $I_{ref}$  is the expected value of turbulence intensity at 15 m/s, both at the hub height (*IEC*, 2005). Classes A, B and C represent high, medium and low turbulence intensities, respectively.

Wind turbine class		I	II	III
$V_{ref}$	[m/s]	50	42.5	37.5
A	$I_{ref}$		0.16	
B	$I_{ref}$		0.14	
C	$I_{ref}$		0.12	

Table 2.3: Basic parameters for wind turbines

From table 2.3 we can read that the IEA 15MW turbine is classified for wind speeds up to 50 m/s and a turbulence intensity of 0.14 at 15 m/s wind speed. This means that the turbine is designed to safely withstand these conditions without taking damage. These parameters are provided by the designer/manufacturer of the wind turbine, and is part of the design specifications. These design specifications has been taken into account when I have generated the wind fields for the load cases 9 to 11.

## 2.6.2 The VoltturnUS-S sub-body

The design of the sub-body, VoltturnUS-S, is made as a cooperation between NREL and University of Maine. It is designed as a three legged semi-submersible platform, with a center pillar.

Parameter	Value
Platform Type	Semi-submersible
Freeboard	15m
Draft	20m
Water Depth	200m
Mooring System	Three-line chain catenary
Total System Mass	20,093 t
Platform Mass	17,839 t
Ballast Mass (Fixed/Fluid)	2,540/11,300 t
Hull Displacement	20,206 $m^3$
Vertical Center of Gravity from SWL	-14.94m
Vertical Center of Buoyancy from SWL	-13.63m

Table 2.4: Specification of the VoltturnUS-S sub-body

A semi-submersible sub-structure has several advantages over a spar-structure, where one of the main advantages is that it does not require a deep water installation facility due to the shallow draft, from table 2.4 the draft of the VoltturnUS-S is only 20m. The tower of the IEA 15MW turbine is placed on the center pillar of the sub-body, see figure 2.9 (Allen *et al.*, 2020).

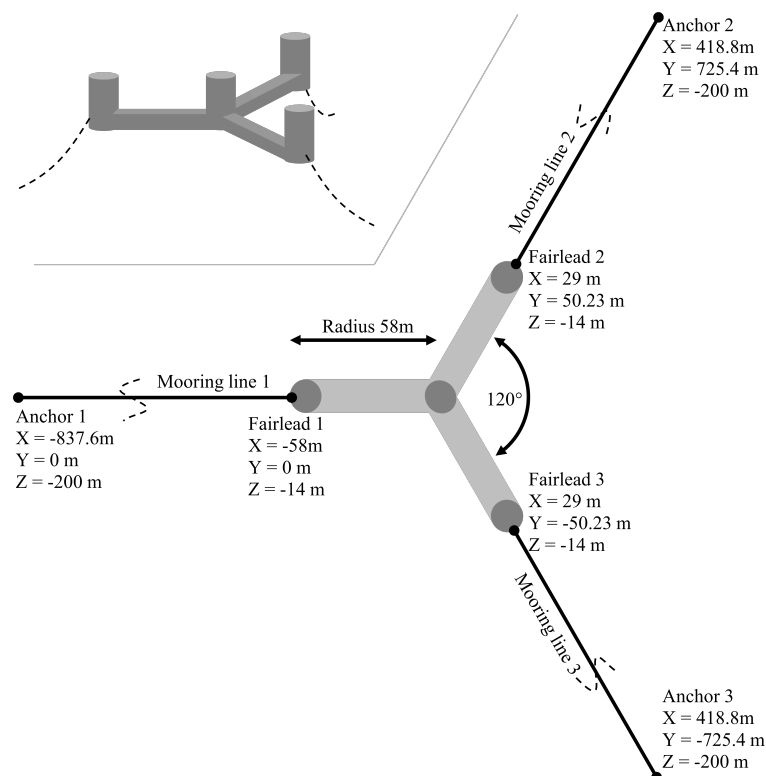


Figure 2.9: Mooring setup for the VoltturnUS-S



### 2.6.3 Mooring line specification for VoltturnUS-S

The mooring line setup is a three line setup with  $120^\circ$  radial spacing as shown in figure 2.9. Table 2.5 gives the coordinates of fairleads and anchors from the platform center.

Line number	Line length	Reference point	X-coordinate	Y-coordinate	Z-coordinate
Line 1	850.0m	Anchor 1	-837.6m	0.0m	-200.0m
		Fairlead 1	-58.0m	0.0m	-14.0m
Line 2	850.0m	Anchor 2	418.8m	725.4m	-200.0m
		Fairlead 2	29.0m	50.2m	-14.0m
Line 3	850.0m	Anchor 3	418.8m	-725.4m	-200.0m
		Fairlead 3	29.0m	-50.2m	-14.0m

Table 2.5: Mooring lines details

The VoltturnUS-S has been designed with a chain catenary mooring setup. It consists of 3 lines, each connected to the substructure at a depth of 14m below sea level. The chain type chosen is the largest commonly available at today's market, 185mm nominal diameter chain links. The fairlead pretension is 2437 kN, at a fairlead angle of  $56.4^\circ$ . This gives a total vertical forcing from the mooring system of 6084 kN, or an equivalent weight of 620 t.

Parameter	Value
Mooring System Type	Chain Catenary
Line Type	R3 Studless Chain
Line Breaking Strength	22,286 kN
Number of Lines	3
Anchor Depth	200m
Fairlead Depth	14m
Anchor Radial Spacing	837.6m
Fairlead Radial Spacing	58m
Line Unstretched Length	850m
Nominal Chain Diameter	185mm
Dry Line Linear Density	685 kg/m
Extensional Stiffness (EA)	3270 MN
Fairlead Pretension	2,437kN
Fairlead Angle from SWL	$56.4^\circ$

Table 2.6: Specification of the VoltturnUS-S mooring setup

## 2.7 Mooring analysis

It is crucial to perform a proper mooring analysis for the floating installation, both for station keeping within the drift-off limits, and to avoid failure of mooring lines. In this thesis I am focusing on catenary mooring, and catenary mooring analysis, though the new model would also be able to model a taut leg mooring system. I have chosen catenary mooring since this is the most commonly used mooring system for both oil and gas industry and FWT industry.

### 2.7.1 Static analysis - zero offset

A static mooring analysis is often performed for the initial design of the mooring system. The pretension of the lines are usually given for a specific structural design, to bring the structure to the correct draft. Pretension is the tension in the mooring lines in a zero environment, meaning no wind, no wave, and no current. The required pretension will help in determining the mooring line properties required, and the length of the mooring lines for the specific site where the structure will be moored. The pretension is normally designed to stay within 10-20% of the minimum breaking load of the line (Ma *et al.*, 2019). An increased pretension will also increase the stiffness of the structure, and reduce the vessels drift-off when exposed to wind and wave loads.

### 2.7.2 Quasi-static analysis - static offset

The quasi-static model is a simplified approach to a dynamic problem. In a quasi-static analysis the tension and the motion of the mooring lines are calculated for each fairlead position, disregarding the dynamic response of the mooring lines due to mass, damping and fluid acceleration. The mooring forces are calculated based on the lines present position, while disregarding its previous position and the motion it has undergone to get to its new position. This means that forces from inertia, damping and viscous drag are neglected (Masciola *et al.*, 2013). This design method requires the use of a higher factor of safety than dynamic analysis, due to its simplification. The quasi-static method was commonly used in the early days of mooring analysis, and is still used where a quick verification needs to be done, but most modern mooring designs are based on dynamic mooring analysis (Ma *et al.*, 2019). OpenFAST has a built-in quasi-static solver called MAP++ (Mooring Analysis Program). This is a multisegmented quasi-static (MSQS) solver. I use this solver for the static comparison between OpenFAST and the advanced rod model used here.

### 2.7.3 Dynamic analysis

Dynamic analysis is usually carried out as a coupled dynamic analysis. This means that several modules of the simulating software is coupled together such that the software is able to analyse the total systems motion and loads as it is being exposed to forces from wind, wave, current and so on. The modules interact with each other to give a more accurate result of the simulation.

Dynamic analysis can be split into two main theories, frequency domain and time domain. Frequency domain-analysis is frequently used when a rapid result is needed. Frequency domain analysis divides the floater motions into 3 parts, mean motion, wave-frequency motion and low frequency motion. The frequency domain analysis requires linearization of the non-linear terms (He and Wang, 2021). A typical frequency domain analysis decouples the mooring line and the structure, and solves the motion of the structure separately from the tension in the mooring line (Ma *et al.*, 2019).

Time domain analysis is a time-stepping analysis method. The structural response is calculated for each time step. Time domain analysis requires more computer resources compared to frequency domain analysis, but this type of analysis has the capability to include non-linearities such as the geometric non-linearity and hydrodynamic drag force. Time domain analysis is therefore considered more accurate, but also more time-consuming (Ma *et al.*, 2019).

## 2.7.4 Current coupled dynamic analysis tools for FWT

There exists a wide range of analysis tools, both for frequency domain and time domain analysis. In this section, I will give a brief overview of some of the analysis softwares available in the industry today.

### OrcaFlex

OrcaFlex by Orcina is often referred to as the industry standard dynamic analysis software. It works as a coupled dynamic simulator, meaning it has modules for aerodynamic, wave and hydrodynamic, mooring etc. which are all coupled together to perform a complete analysis of the system for a given condition. It can be used for analysis of various applications, such as riser systems, transport, installation and decommissioning, renewables and moorings and global performance. OrcaFlex can be used for both nonlinear time domain analysis and for linear frequency domain analysis. For its mooring analysis, OrcaFlex uses a proprietary lumped-mass-based mooring line model (*Orcina, 2023a*). For more info on the lumped-parameter model, see 2.7.5.

### Sima

Sima by Sintef is a workbench for simulation, interpretation and documentation of analysis results. It is a simulation software for marine operations and floating systems. It is based on software for non-linear time-domain analysis. It can output graphical results in 3D and 2D. For mooring analysis Sima uses its built-in programs RIFLEX and SIMO. SIMO is a simulation program for motions and station-keeping behaviour of complex systems of both floating vessels and suspended loads. It is a non-linear time-domain analysis software. RIFLEX can perform both dynamic time-domain analysis and frequency domain analysis.

### OpenFAST

OpenFAST by NREL is an open-source simulation code, free to use. OpenFAST was designed by NREL to provide a free to use software to the wind industry to aid in the development of wind energy parks. OpenFAST is the framework which couples the different computational modules for aerodynamics, hydrodynamics for offshore structures, control and electrical system dynamics and structural dynamics. Thus OpenFAST is able to perform coupled nonlinear aero-hydro-servo-elastic simulation in time domain. MoorDyn is the mostly used dynamic mooring simulator incorporated in OpenFAST. The results from MoorDyn needs to be analysed in a separate system, like Matlab or Python, due to its large time-series output files. The report by *Wendt et al. (2016)* performed a validation and verification of MoorDyn versus wave tank measurements and the commercial software OrcaFlex. It proved largely equivalent in results.

## 2.7.5 Lumped parameter modelling approach

Most dynamic mooring analysis softwares uses the lumped mass dampener method for computing loads and motion of a mooring line. The lumped mass method was first developed by *Walton and Polachek (1960)*. In this method, the line's evenly distributed mass is replaced by a finite number of point masses along the line. This replacement idealizes the system as a set of point masses at nodes and non-mass spring-dampeners as segments between the nodes. A schematic of the lumped mass model can be seen in figure 2.10. The number of nodes is  $N$ , while the number of segments is always one less,  $N-1$ .

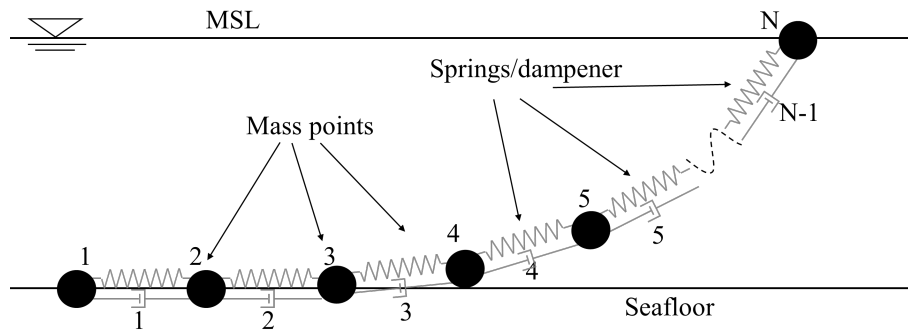


Figure 2.10: Lumped mass schematic

## 2.7.6 Seafloor contact problem

One important feature of any mooring line simulation tool is the ability to simulate a barrier at the seafloor. This is required to handle the interaction of the mooring line with the seafloor. I will give a short overview of how the various models solve for the contact between the mooring line and the seafloor.

### MAP++

MAP++ (Mooring Analysis Program) solves the interaction of the mooring line with the seafloor by splitting the catenary equations into 3 parts. Part 1 is where the line is in contact with seafloor but does not experience tension in the line, part 2 is where the line is in contact with seafloor and experience tension, while part 3 is the suspended line. This is similar to how I made the ICE solver, see section 3.2.2. If the vertical force at the free end is less than the total weight of the cable, then a portion of the mooring line will rest on the seafloor. The unstretched length of cable lying on the seafloor can be found from  $L_B = L - V/W$  (Jonkman, 2007), where  $L_B$  is the resting line,  $L$  is the total line length,  $V$  is vertical force and  $W$  is the weight force pr. meter.

MAP++ also accounts for seafloor friction, and  $x_0$ , as shown on figure 2.11, refers to the point where there is no horizontal force left in the line due to seafloor friction (Masciola *et al.*, 2013). If seafloor friction is neglected, then the horizontal force at the anchor,  $H_a$ , will be equal to the horizontal force at the fairlead,  $H$ , but in opposite directions.

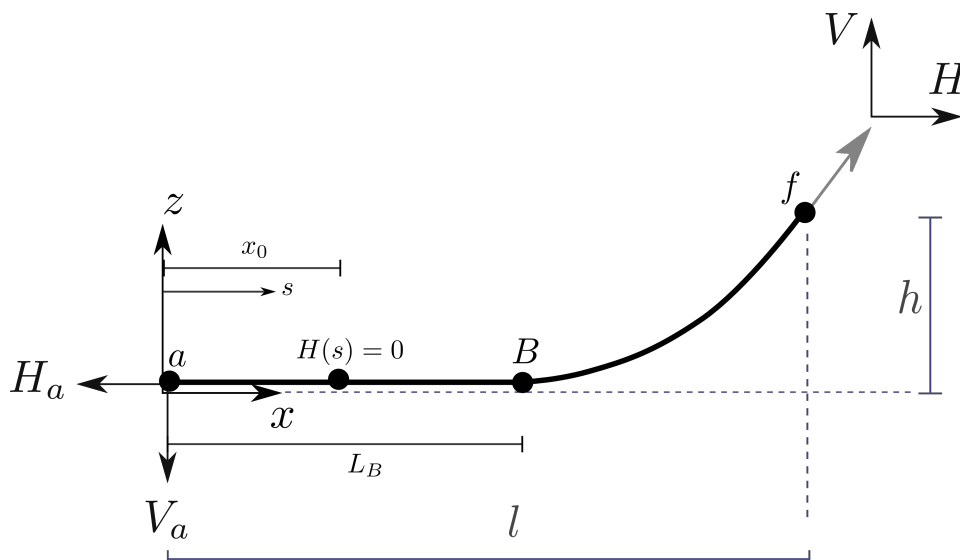


Figure 2.11: MAP++ line definitions with seafloor contact, courtesy NREL/MAP++.

## MoorDYN

MoorDyn mooring model uses a linear spring-dampener approach to handle interaction with the seafloor, as shown on figure 2.12. The spring-dampener represents the vertical reaction forces when a cable node touches the seafloor. A stiffness coefficient,  $k_b$ , represents the stiffness per unit area of the seafloor, and the damping coefficient,  $c_b$ , represents the viscous damping per unit area. The model is only active when a node contacts the seafloor (i.e. when  $z_i \leq z_{bot}$ ). When that condition is true, the force due to the interaction is modeled as:

$$B_i = dl[(z_{bot} - z_i)k_b - \dot{z}_i c_b] \mathbf{e}_z \quad (2.13)$$

where  $dl$  represents the segment length.

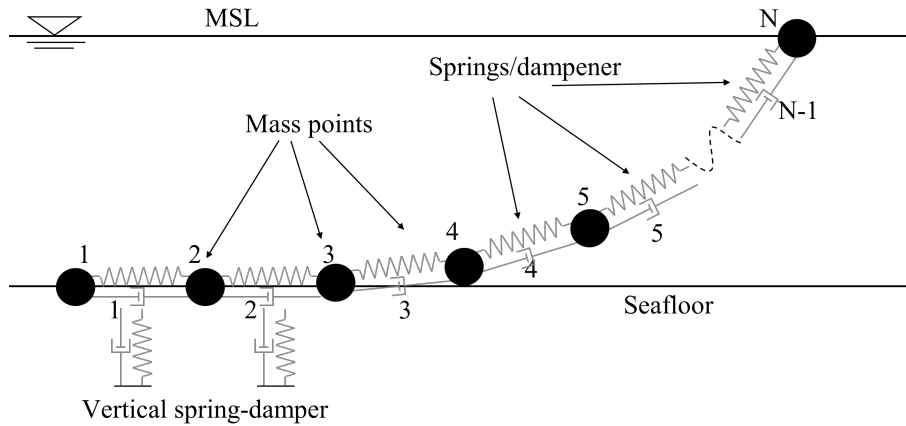


Figure 2.12: MoorDyn vertical spring-dampener approach.

The bottom contact spring stiffness and dampener introduces a pressure which is applied to the cross-sectional area (diameter · length) of each contacting line segment. This gives a resulting vertical force for each segment equal to the weight force of the segment (Hall, 2015).

## OrcaFlex

OrcaFlex has a similar approach as MoorDyn, since both these models are based on the lumped parameter modelling approach. OrcaFlex has the capability to model the springs with either linear or nonlinear stiffness, and linear damping. In addition, OrcaFlex can model the sea bottom friction (Orcina, 2023b).

## 2.8 Mathematical properties used in the new advanced model

To give better understanding of how the new advanced rod model works, I will in this section describe some of the most important mathematical and material properties used.

### 2.8.1 Kirchhoff rod theory

As mentioned, the new advanced rod model is based on a special case of Kirchhoff rod theory (Kirchhoff, 1859). Kirchhoff rod theory describes the non-linear bending and twisting of slender elastic rods in 3-D. The theory has been widely studied to predict rod deformation given its geometry and boundary conditions. The advanced rod model is a special case because it is torsion free, and shear free (Gebhardt and Romero, 2021; Romero and Gebhardt, 2020), and only looks at two deformation modes, namely elongation and curvature (stretch and bending).

## 2.8.2 Elastic modulus

A material will deform when a stress is applied. We can split the elastic modulus into three different elastic modulus based on which stress it is exposed to (*Jones and Ashby, 2019*). Young's modulus is the elastic modulus for axial strain (compression and tension). It is a material property describing the stiffness of a solid material when the force is applied lengthwise (axial). It is defined as the relationship between tensile/compressional stress ( $\sigma$ ) and axial strain ( $\epsilon$ ). Shear modulus, also called modulus of rigidity, is similar to Young's modulus, but describes a materials resistance to shear deformation when the force is applied sideways, or more precise, it is a measure of the elastic shear stiffness of a solid material. It is defined as the ratio of shear stress,  $\tau_{xy}$ , to shear strain,  $\gamma_{xy}$ . The last elastic modulus is called bulk modulus, and this describes the volume change under applied pressure.

There exists also a ratio of longitudinal to lateral strain. When a material is exposed to strain in lateral direction, it will also deform in the longitudinal direction, and vice versa. This relationship is called Poisson's ratio,  $\nu$ , after the French mathematician and physicist Siméon Poisson.

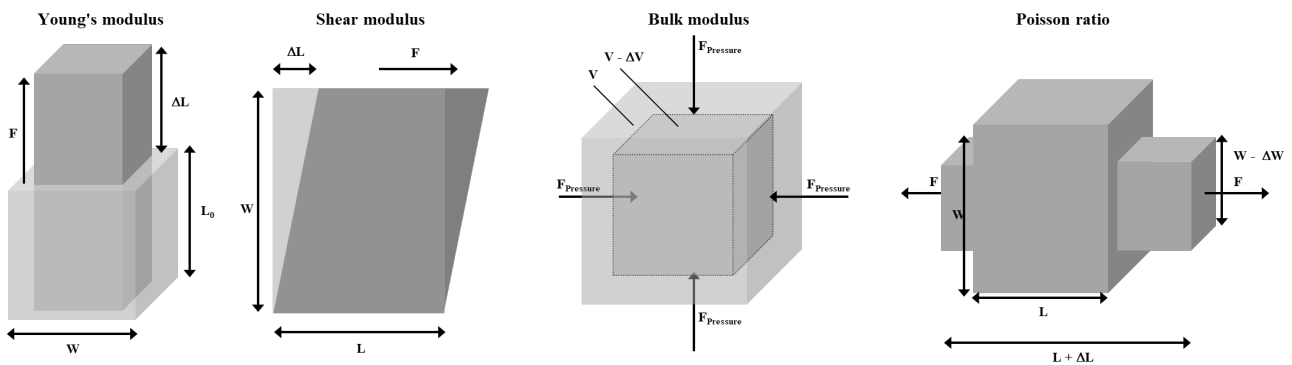


Figure 2.13: Sketch showing different elastic modulus. Adapted from *agilescientific.com*.

Young's modulus

$$E = \frac{\sigma}{\epsilon}$$

Shear modulus

$$G = \frac{\tau_{xy}}{\gamma_{xy}}$$

Bulk modulus

$$K = -V \frac{dP}{dV}$$

Poisson's ratio

$$\nu = -\frac{d\epsilon_{trans}}{d\epsilon_{axial}}$$

Young's modulus is an important material property for mooring lines, as this will dictate the elongation of the line due to tension. Young's modulus,  $E$ , for steel is typically around 205 GPa. The nominal chain diameter for the chosen model is 185mm, with an the extensional stiffness,  $EA$ , of 3270 MN, as described in table 2.5. For the chosen model, the chain length is 850m, with a pretension of 2.4 MN, from table 2.5. If we estimate an average tension in the line of 2 MN throughout the total length of the line, we can estimate how much the line stretches, based on the  $EA$ , using equation 2.12. The stretched mooring line length will be,

$$s = \left(1 + \frac{T}{EA}\right)p = \left(1 + \frac{2.0}{3270}\right)850 = 850.52\text{m.}$$

The line stretches only 52 cm, or 0.06%, which may seem insignificant, but I will show during the development of a static mooring analysis code why it is important to incorporate elasticity for the mooring lines. The development of the static mooring code can be found in section 3.2.2.

### 2.8.3 Elastic deformation and hyperelasticity

The deformation of a material is highly dependent on the material properties. Steel is a typical elastic material, and will undergo elastic deformation if a stress is applied. As the stress reaches the yield point, the deformation will change from elastic to plastic, see figure 2.14a, and as the material undergoes plastic deformation it will not return to its original state, but have a permanent deformation. If the stress is further increased, it will result in total material failure. It is vital for elastic materials undergoing deformation that the stress in the material is kept within the region of linear deformation. A safety factor, or safety margin, is often used for the maximum stress to avoid the stress to reach the yield point of the material.

Materials, like rubber, polyester or nylon, is elastic, but does not deform linearly, but rather highly non-linearly, see figure 2.14b. These materials are called hyperelastic. During the initial loading the hyperelastic material undergoes a permanent deformation (*Ridge et al., 2010*). During subsequent loading sequences the material will return to the initial state. The deformation of hyperelastic materials remains elastic up to large strain values (often well over 10%) (*Ridge et al., 2010*).

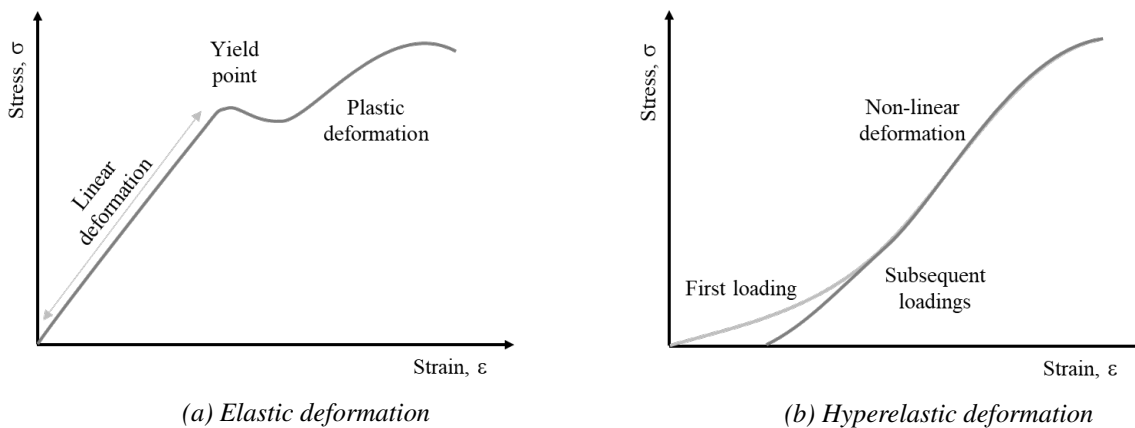


Figure 2.14: Stress-Strain relationship for elastic and hyper-elastic deformation.

The mooring industry is more and more looking into shifting from steel mooring materials towards use of synthetic fibre rope like polyester and nylon to save cost. These materials are cost effective in both material cost and handling, but they do not deform elastically, but rather hyperelastic. New mooring analysis models should incorporate this to aid in modelling of new mooring line materials.

### 2.8.4 Moment of area and inertia

#### Second moment of area

Second moment of area, also called the area moment of inertia, is a geometrical property which reflects how the objects points are distributed with regards to an arbitrary axis. The second moment of area is typically denoted with an  $I$ , and it is found by taking a double integral over the object. The more points the object has further from the axis, the larger the moment of area. The unit of the second moment of area is meters to the fourth power,  $m^4$ . Figure 2.15 shows two examples of the second moment of area.

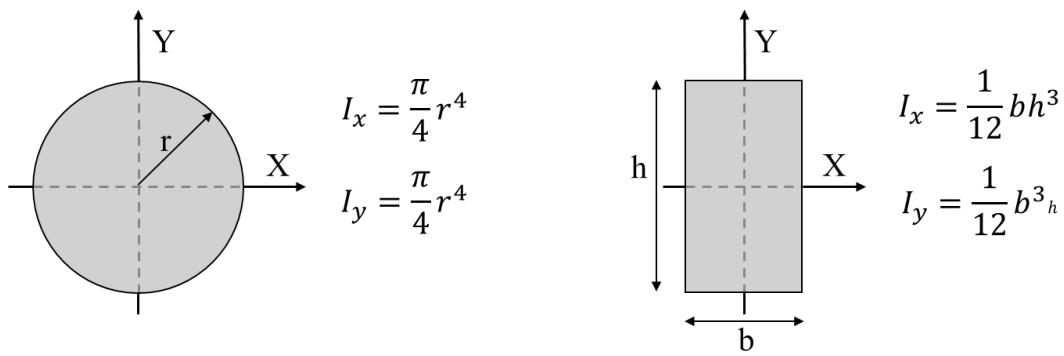


Figure 2.15: Example of 2<sup>nd</sup> moment of area.

### Moment of inertia

The moment of inertia (MOI), also called the mass moment of inertia, describes how the mass of the object is placed with regards to a rotational axis. If more of the mass is placed further from the axis, the moment of inertia increases. MOI is a quantity that determines the torque required for a desired angular acceleration about a rotational axis. This is similar to how mass will require a certain force for a desired acceleration. Figure 2.16 shows how the MOI for a cylinder with evenly distributed mass varies based on which axis the MOI is calculated for.

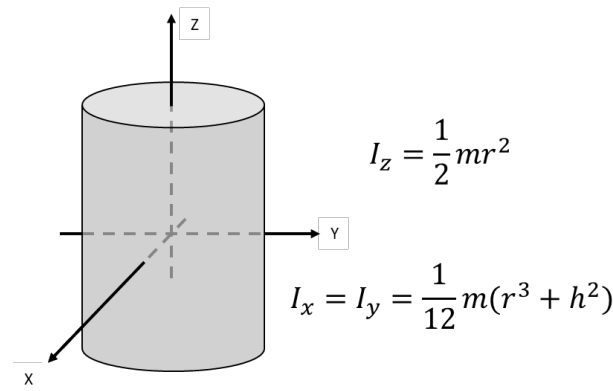


Figure 2.16: Example of moment of inertia.

## 2.8.5 Lagrangian mechanics

A rigid body mechanics problem can be solved in two ways, either by using the Newtonian approach, based on Newton's laws, or using the Lagrange's approach, based on the stationary-action principle (Lê, 2019). Lagrangian mechanics is a formulation of classical mechanics by Joseph-Louis Lagrange. In 1755 when he found that a rigid body mechanical problem could be described using the system's potential and kinetic energy (Foroghei et al., 2015). This was a new way of thinking for mechanical engineering, and was called Lagrangian mechanics. The idea of Lagrangian mechanics is that a mechanical system can be described using a configuration space and a smooth function  $\mathcal{L}$ . The configuration space is a set of generalized coordinates,  $\varphi$ , that define the configuration of a system. The Lagrangian,  $\mathcal{L}$ , is defined as the kinetic energy,  $T$ , minus potential energy,  $U$ .

$$\mathcal{L} = T - U \quad (2.14)$$

The foundation in Lagrangian mechanics is the stationary-action principle, which requires that the action functional of the system must remain stationary for the time evolution. Action is



similar to work. In simpler words, nature is lazy, and will take the path that requires the least amount of work. The action functional,  $\mathcal{S}$ , is defined as the integral of  $\mathcal{L}$  over time.

$$\mathcal{S}[\varphi(t)] = \int_{t_1}^{t_2} \mathcal{L}(\varphi, \dot{\varphi}, t) dt = \int_{t_1}^{t_2} (T - U) dt \quad (2.15)$$

To solve a rigid body mechanics problem using Lagrange's approach, we use the principle of stationary-action to find the equation of motion of this specific problem. The principle of stationary-action is a variational principle, where the problem can be solved using calculus of variations. Calculus of variations is a field of mathematics that uses variations, or small changes, in a functional.

$$\delta \mathcal{S}[\varphi(t)] = \delta \int_{t_1}^{t_2} \mathcal{L}(\varphi, \dot{\varphi}, t) dt = \int_{t_1}^{t_2} \delta \mathcal{L}(\varphi, \dot{\varphi}, t) dt = 0 \quad (2.16)$$

## 2.8.6 Equation of motion in Lagrangian configuration

In the 1750s Euler and Lagrange together developed the Euler-Lagrange equation of classical mechanics while working on solving the tautochrone problem. The tautochrone problem is to find a curve for which the time it takes an object that slides without friction to its lowest point is independent of its starting point. From equations 2.15 and 2.16 we can derive the equation of motion for a system in the Lagrangian configuration.

Since  $\delta \mathcal{L}(\varphi, \dot{\varphi}, t) = \delta T(\varphi, \dot{\varphi}, t) - \delta U(\varphi, t)$ , and

$$\delta T(\varphi, \dot{\varphi}, t) = \frac{\partial T}{\partial \dot{\varphi}} \delta \dot{\varphi} + \frac{\partial T}{\partial \varphi} \delta \varphi, \text{ and } \delta U(\varphi, \dot{\varphi}, t) = \frac{\partial U}{\partial \dot{\varphi}} \delta \dot{\varphi} + \frac{\partial U}{\partial \varphi} \delta \varphi \quad (2.17)$$

Plugging in 2.17 into 2.16 gives:

$$\delta \mathcal{S} = \int_{t_1}^{t_2} \left[ \frac{\partial T}{\partial \dot{\varphi}} \delta \dot{\varphi} - \frac{\partial U}{\partial \dot{\varphi}} \delta \dot{\varphi} + \frac{\partial T}{\partial \varphi} \delta \varphi - \frac{\partial U}{\partial \varphi} \delta \varphi \right] dt = 0 \quad (2.18)$$

From the principle of differentiation ( $((\mathbf{u}\mathbf{v})' = \mathbf{u}'\mathbf{v} + \mathbf{u}\mathbf{v}')$ ), the first two parts of the integral 2.18 can be rewritten,

$$\frac{\partial T}{\partial \dot{\varphi}} \delta \dot{\varphi} = \frac{d}{dt} \left( \frac{\partial T}{\partial \dot{\varphi}} \delta \varphi \right) - \frac{d}{dt} \frac{\partial T}{\partial \dot{\varphi}} \delta \varphi \quad (2.19)$$

$$\frac{\partial U}{\partial \dot{\varphi}} \delta \dot{\varphi} = \frac{d}{dt} \left( \frac{\partial U}{\partial \dot{\varphi}} \delta \varphi \right) - \frac{d}{dt} \frac{\partial U}{\partial \dot{\varphi}} \delta \varphi. \quad (2.20)$$

Since  $\frac{\partial T}{\partial \dot{\varphi}} \delta \varphi|_{t_1}^{t_2} = \frac{\partial U}{\partial \dot{\varphi}} \delta \varphi|_{t_1}^{t_2} = 0$  due to the boundary conditions, we can simplify equation 2.18 to,

$$\begin{aligned} \delta \mathcal{S} &= \int_{t_1}^{t_2} \left[ -\frac{d}{dt} \frac{\partial T}{\partial \dot{\varphi}} \delta \varphi + \frac{d}{dt} \frac{\partial U}{\partial \dot{\varphi}} \delta \varphi + \frac{\partial T}{\partial \varphi} \delta \varphi - \frac{\partial U}{\partial \varphi} \delta \varphi \right] dt = 0 \\ &= \int_{t_1}^{t_2} -\delta \varphi \left[ \frac{d}{dt} \frac{\partial T}{\partial \dot{\varphi}} - \frac{d}{dt} \frac{\partial U}{\partial \dot{\varphi}} - \frac{\partial T}{\partial \varphi} + \frac{\partial U}{\partial \varphi} \right] dt = 0. \end{aligned}$$

And since  $\delta \varphi$  cannot be 0, this means the integrand has to be zero, and we end up with the Euler-Lagrange equation,

$$\underbrace{\frac{d}{dt} \frac{\partial T}{\partial \dot{\varphi}_j}}_{\text{I}} - \underbrace{\frac{d}{dt} \frac{\partial U}{\partial \dot{\varphi}_j}}_{\substack{=0 \text{ for} \\ \text{mechanical} \\ \text{systems}}} - \underbrace{\frac{\partial T}{\partial \varphi_j}}_{\text{II}} + \underbrace{\frac{\partial U}{\partial \varphi_j}}_{\text{III}} = \underbrace{Q_j}_{\text{IV}}, \quad (2.21)$$

where  $\varphi_j$  is the generalized coordinates,  $\dot{\varphi}_j$  is the generalized velocity and  $Q_j$  is the generalized external force. The system being investigated needs to be complete, and the generalized coordinates needs to fully describe the motion of the system.

To solve this differential equation, the first thing to do is to determine how many DOF's is required to describe the motion. Then verify that the coordinates are complete, independent and the system is holonomic. Next step is to make expressions for kinetic energy,  $T$ , and potential energy,  $U$ , for every rigid body in the system, and use this to compute I, II and III from equation 2.21. To find  $Q_j$  for each  $\varphi_j$ , find the generalized force that acts in this coordinate, and compute the virtual work ( $\delta W^n$ ) associated with the virtual displacement ( $\delta\varphi_j$ ),

$$\delta W_j = Q_j \delta\varphi_j. \quad (2.22)$$

### Lagrange's approach to solve a swinging pendulum

A simple example is a pendulum, swinging in a 2 dimensional space. For this special case, only one degree of freedom will be required to describe the pendulum's motion. The generalized coordinate of this example is the angle  $\theta$ . As the pendulum swings,  $\theta$  will vary by time, and the position, velocity and acceleration can all be described as a function of  $\theta$ , see figure 2.17.

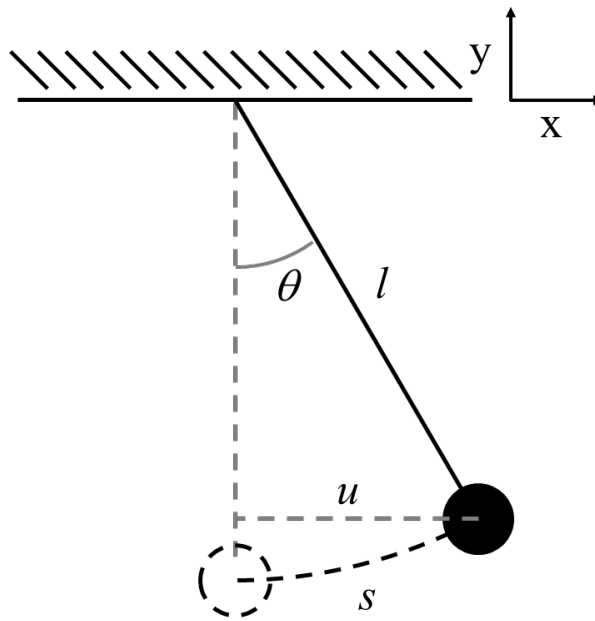


Figure 2.17: Sketch of a pendulum swinging.

$\theta$  is the angle of the line from vertical,  $l$  is the length of the line,  $s$  is the arc length of the swing and  $u$  is the projection of the arc length  $s$ .

As the pendulum moves, the kinetic and potential energy of the system will vary. If we consider the pendulum in a non-friction environment where the energy is conserved, the potential energy will be transferred to kinetic energy and vice versa as the pendulum moves.

$$\mathcal{L} = T - U \quad (2.23)$$

The kinetic and potential energy for the system can be written as,

$$T = \frac{1}{2}mv^2 \quad \text{and} \quad U = mgy, \quad (2.24)$$

where  $m$  is the mass of the pendulum,  $v$  is the velocity of the pendulum,  $g$  is the gravity constant and  $y$  is the vertical distance from the reference. Next step is to rewrite equations 2.24 to the generalized coordinate,  $\theta$ ,

$$\begin{aligned} v = \dot{s} = l\dot{\theta} &\Rightarrow T = \frac{1}{2}mv^2 = \frac{1}{2}ml^2\dot{\theta}^2 \\ y = -l \cdot \cos\theta &\Rightarrow U = mgy = -mgl \cos\theta. \end{aligned}$$

Next I will write up the Lagrangian,  $\mathcal{L}$ ,

$$\mathcal{L} = T - U = \frac{1}{2}ml^2\dot{\theta}^2 + mgl \cos\theta. \quad (2.25)$$

There exists no external forces in this example, hence  $Q = 0$ , and by using the Euler-Lagrange equation 2.21 we get,

$$\begin{aligned} \frac{d}{dt} \left( \frac{\partial T}{\partial \dot{\theta}} \right) &= \frac{\partial U}{\partial \theta} \\ ml^2\ddot{\theta} &= mgl \sin\theta \\ \ddot{\theta} &= -\frac{g}{l} \sin\theta. \end{aligned} \quad (2.26)$$

Equation 2.26 is the equation of motion for the pendulum, a nonlinear differential equation.

The equation of motion for the pendulum can be linearized using Taylor expansion and small angle approximation valid for  $\theta < 0.1$ ,

$$\begin{aligned} \sin\theta &= \frac{u}{l} \\ \ddot{\theta} &\approx \frac{\ddot{u}}{l} \\ \ddot{\theta} = -\frac{g}{l} \sin\theta &\xrightarrow{\text{by linearization}} \frac{\ddot{u}}{l} = \frac{g}{l} \cdot \frac{u}{l} \\ \ddot{u} + \frac{g}{l} \cdot u &= 0. \end{aligned} \quad (2.27)$$

Equation 2.27 is the final linearized equation of motion for the pendulum. This is an approximated solution, and valid only for small angles of  $\theta$ .

## 2.8.7 Finite Element Method

Finite Element Method (FEM) is a much used solving technique when no analytical solution can be found. It is a way of finding a numerical approximation to an IBV or a BVP (boundary value problem) (Rao, 2017). To achieve this, the problem is split into smaller, simpler parts called finite elements. A set of linear functions, one for each node, are used to substitute the BVP. FEM solving technique has several advantages over other numerical approximations, due to its numerical efficiency, it is capable of modeling of non-linearities, and the discretization can be accomplished for even complex geometry. FEM can be used for a variety of problems, like structural analysis, fluid flow and heat transfer analysis, to mention a few (Baccouch, 2021).

FEM can be divided into 4 steps according to *Baccouch* (2021)

1. Find the variational formulation of the equation
2. Discretize the object
3. Define the space where to look for the solution
4. Solve the resulting discrete system

### **Variational formulation**

From the strong form of the boundary value problem, we need to find the variational formulation. To achieve this, a test function is introduced, and multiplied with the strong form equation. By using integration by parts, one of the derivatives is moved from the strong form equation to the test function. This transforms the strong form equation to the variational formulation.

### **Discretization / Meshing**

The next step in the FEM solving technique is to describe the object in question by a selection of geometric elements. The object is discretized by using a mesh of geometric elements to describe the object. The accuracy in the numerical solution can be dependent on the size and number of elements, so it is important to select a discretization that properly describes the object, but also keep in mind that an increased number of elements yields an increased number of equations, and larger matrices to solve.

### **Define the space**

The functional spaces needs to be defined for the variational formulation, before creating the weak form of the differential equation. The next step in the FEM process is to transform the weak form to the Galerkin formulation using a set of shape functions, before proceeding with the Galerkin approximation.

### **Solving the discrete system**

The last step is to solve the linear system of equations, and thus find a numerical approximation to the boundary value problem. Most often a computer program is used for solving the linear system of equations. Depending on the number of nodes, the number of equations and size of matrices can grow quite huge for complex problems.

## **2.8.8 Isogeometric discretization in FEM solving technique**

The FEM solving technique used for the advanced rod model is what is called isogeometric analysis. This discretization scheme deals with control points instead of classical nodal finite elements (*Nguyen et al., 2023*). Isogeometric discretization closes the gap between FEM discretization and CAD modelling. Using the isogeometric discretization scheme can reduce the number of DOF's, and in turn reduce the required analysis time for a simulation, but it can also introduce errors and numerical artifacts due to shear locking. Shear locking due to the linear nature of quadrilateral elements makes the element appear stiffer than it actually is, and thus reducing bending displacements (*FEM Data streamliner; ANSYS*).

# Chapter 3

## Methodology

For this master thesis, I will use OpenFAST simulation tools for the simulation of a FWT for a selection of different load cases. The load cases have been selected based on the technical report by *Gaertner et al.* (2020), and shown in table 3.1.

### 3.1 Table of load cases

Load case	Description	Duration [s]	Wind	Wave	Turbine	Comment
1	Surge decay	1500	-	-	Idling	Model Verification
2	Sway decay	1500	-	-	Idling	Model Verification
3	Heave decay	1500	-	-	Idling	Model Verification
4	Pitch decay	1500	-	-	Idling	Model Verification
5	Yaw decay	1500	-	-	Idling	Model Verification
6	Roll decay	1500	-	-	Idling	Model Verification
7	Static equilibrium	7200	-	-	Idling	Dynamic relaxation
8	Step wind	9200	Uniform wind, 3-25 m/s	-	Operating	Controller functionality
9	Dynamic load case 1	5400	10.59 (NTM)	-	Operating	Rated wind speed
10	Dynamic load case 2	5400	10.59 (NTM)	Hs=1.6 m, Tp= 7.6s	Operating	Rated wind speed + waves
11	Dynamic load case 3	5400	47.5 m/s (EWM 50)	Hs= 10.7m, Tp= 14.2s	Idling	EWM 50 yr

Table 3.1: Simulated loadcases

Load cases 1 to 6 are simulated in OpenFAST for model verification versus the technical report (*Allen et al.*, 2020). These load cases have not been simulated in the advanced rod model (ARM). The simulation of load case 7 is a dynamic relaxation of the FWT. The resulting static fairlead force from MoorDYN is input in ARM to compare the dynamic relaxation. The resulting static fairlead force from MoorDYN is also used in load cases 8 to 11 to let the mooring line dynamically relax to a static position before proceeding with the dynamic load. Load case 8 is chosen to see the controller's response to varying wind speed, and the effect it has on the structure's behaviour and the mooring lines. Load cases 9 to 11 are simulated for comparison of MoorDYN mooring line analysis versus ARM mooring line analysis. Load case 9 is simulation with wind at rated wind speed for the turbine without waves. For load cases 10 and 11, waves are introduced, where the corresponding wave  $H_s$  and  $T_p$  are both based on the technical report (*Allen et al.*, 2020) where the environmental conditions for U.S. East coast is used as a base. The wind speed for load case 11 is at a 50-year return period for the same site. All simulations considered a wind and wave heading aligned with the wind turbine ( $0^\circ$ ).

The wind fields for load case 9 through 11 are generated using TurbSim v2.00. TurbSim is a turbulence generator, which is based on statistical models. It is able to generate velocity

fluctuations in a 2-D plane for all three velocity components. You can imagine that TurbSim generates a 3-D box, with user specified size and resolution. This box gets filled with wind with 3 velocity components. When OpenFAST runs a simulation with this wind field, the box will move across the turbine at the speed defined as the mean wind speed.

HydroDyn is the module used for wave generation in OpenFAST. HydroDyn is capable of generating waves in several ways, both regular and irregular waves. I have used Jonswap/Pierson-Moskowitz spectrum (*Spiess, 1975*), (*Pierson and Moskowitz, 1964*), for generation of irregular waves for load cases 10 and 11.

### 3.1.1 Explanation to table

The below explanations have been adapted from standards IEC 61400-3, (*IEC, 2009*), IEC 61400-1, (*IEC, 2005*) and DNV metocean characterization (*DNV, 2018*).

#### NSS - Normal sea state

Normal sea state is defined as the joint probability distribution of met ocean parameters for a specific location. This means that for a specific location, each specific wind speed and wind direction will have a normal sea state, where the sea state is defined by  $H_s$ ,  $T_p$  and direction.

#### SSS - Severe sea state

Similar to NSS, but instead of the SSS combines normal wind conditions with 50-year wave condition, such that the the wind turbine will be in operating mode, while being exposed to the 50-year waves. This is used in simulation of ultimate loading of an offshore wind turbine.

#### ESS - Extreme sea state

Similar to NSS, ESS is the defined  $H_s$ ,  $T_p$  and direction for extreme sea state for a specific mean wind for a specific site, for a specific return period. The return period can for example be 1-year, 50-year, 100-year and so on.

#### NTM - Normal turbulence model

The IEC standard 61400-1 defines NTM as the standard deviation at the 90<sup>th</sup> quantile for a given wind speed at hub height,  $V_{hub}$ , using equation 3.1. The constant  $b$  is derived from measurement data, and given at 5.6 m/s.

$$\sigma_1 = I_{ref}(0.75 \cdot V_{hub} + b) \quad (3.1)$$

#### ETM - Extreme turbulence model

For ETM the turbulence longitudinal component standard deviation is given by,

$$\sigma_1 = cI_{ref} \left[ 0.072 \left( \frac{V_{ave}}{c} + 3 \right) \left( \frac{V_{hub}}{c} - 4 \right) + 10 \right], \quad (3.2)$$

where  $c$  is a constant of 2 m/s.  $I_{ref}$  is the reference turbulence intensity at 15 m/s from table 2.3,  $V_{ave}$  is the annual average wind speed at hub height, and  $V_{hub}$  is the 10-minute mean wind speed at hub height.

## EWM - Extreme wind speed model

EWM can be either a steady or turbulent wind model. Both models are based on the reference wind speed,  $V_{ref}$  from table 2.3, and a fixed turbulence standard deviation,  $\sigma_1$ . For the steady extreme wind model, the wind speeds are calculated with recurrence periode of 1-year and 50-year, as a function of height using the power law equation with a coefficient of 0.11, multiplied by 1.4 for 50-year return period, see equation 3.3, and for 1-year return period the wind speed is 80% of the wind speed at 50-year return period, see equation 3.4 (IEC, 2005).

$$V_{e50}(z) = 1.4V_{ref} \left( \frac{z}{z_{hub}} \right)^{0.11} \quad (3.3)$$

$$V_{e1}(z) = 1.12V_{ref} \left( \frac{z}{z_{hub}} \right)^{0.11} = 0.8V_{e50}(z) \quad (3.4)$$

For the turbulent EWM, the 50-year wind speed are calculated in the same way, but without the multiplication of 1.4, and the 1-year wind speed is 80% of this. The longitudinal turbulence standard deviation is given by,

$$\sigma_1 = 0.11V_{hub}. \quad (3.5)$$

## 3.2 Static Solver

I wanted to make a simplified static mooring solver based on the elastic catenary formulation, where the required inputs would be the mooring line properties, like weight and young's modulus, coordinates of the anchor and fairlead. I have used mooring line 1 from the model VoltornUS-S, with the coordinates from table 2.5, and the line properties from table 2.6. I started with the inelastic formulation, and made a script that solves the differential equation using the Newton Raphson, N-R, method. The next section will give a description this work.

### 3.2.1 Inelastic catenary equations

The catenary equations are based on the hyperbolic sine and cosine functions.

$$Y = a \cosh \left( \frac{X}{a} \right) \text{ and } X = a \sinh^{-1} \left( \frac{S}{a} \right) \quad (3.6)$$

$$Y^2 = a^2 + S^2 \quad (3.7)$$

In addition to the equations, I have some input data based on the static mooring coordinates used in OpenFAST for line 1. Subscript A refers to anchor and subscript F refers to fairlead.

$$\hat{X}_A = -837.6 \quad \hat{Y}_A = -200.0 \quad \hat{X}_F = -58.0 \quad \hat{Y}_F = -14.0$$

Next, I will move the origin from the platform center to the anchor position. This will change the coordinates to,

$$X_A = 0 \quad Y_A = 0 \quad X_F = 779.6 \quad Y_F = 186.$$

The mooring line length is given, at  $L = 850$ , and I can update the catenary formulas, using  $S$  as the length of the suspended line,

$$Y = Y_F + a = a \cosh\left(\frac{X_F - L + S}{a}\right) \quad (3.8)$$

$$X = X_F - L + S = a \sinh^{-1}\left(\frac{S}{a}\right) \quad (3.9)$$

$$S = \sqrt{Y^2 - a^2} = \sqrt{(Y_F + a)^2 - a^2} = \sqrt{Y_F^2 + 2Y_F a}. \quad (3.10)$$

By inserting 3.10 in equation 3.8 and 3.9 and rearranging the expression,

$$Y_F = a \left[ \cosh\left(\frac{X_F - L + \sqrt{Y_F^2 + 2Y_F a}}{a}\right) - 1 \right] \quad (3.11)$$

$$X_F = a \sinh^{-1}\left(\frac{\sqrt{Y_F^2 + 2Y_F a}}{a}\right) + L - \sqrt{Y_F^2 + 2Y_F a}. \quad (3.12)$$

I have now obtained two equations, both of which are in term of one unknown, the shape parameter  $a$ . To perform the N-R method for numerical approximation, only one equation is needed. I decided to use 3.11. I set this equation equal to zero, and I need the derived function with regards to the unknown,  $\frac{df}{da}$ . To simplify the expression I first create a helper function  $g$  and collect some of the constants.

$$B = X_F - L, \quad C = Y_F^2, \quad D = 2Y_F, \quad g = \frac{B + \sqrt{C + Da}}{a} \quad (3.13)$$

$$\frac{df}{da} = - \left[ \cosh(g) + \sinh(g) \left( \frac{D}{2\sqrt{C + Da}} - g \right) \right] + 1 \quad (3.14)$$

Using the N-R method on equation 3.11 and 3.14, I was able to find a numerical approximation for the parameter  $a$ . When I insert the parameter  $a$  in equations 3.8 and 3.10, I can find the touchdown point, length of the resting line,  $RL$ , and the coordinates of the suspended line,  $S$ , as shown in table 3.2.

Results from the inelastic solver			
$a = 234.3$	$S = 348.94 \text{ m}$	$RL = 501.06 \text{ m}$	$TD = -336.54 \text{ m}$

Table 3.2: Results from inelastic N-R.



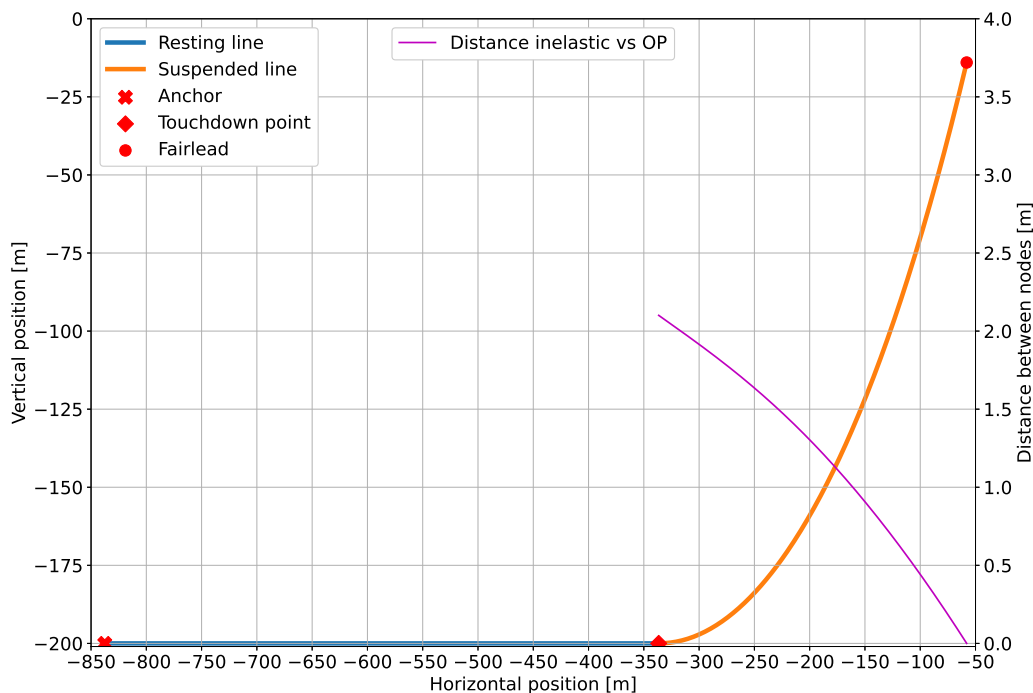


Figure 3.1: Figure showing the static inelastic solution for line 1.

Figure 3.1 shows the plotted mooring line using equation 3.8 with the shape parameter  $a$  found from the N-R method. Origin has now been set back to platform center, so I can compare the results with OpenFAST (OP). As can be seen from the figure the inelastic solution diverges from the OpenFAST static solution at the touchdown point, the distance between the solvers is the purple curve. Since there is no stretching of the mooring line, inelastic formulation, the line is shorter compared to OpenFAST, such that touchdown point is closer to the anchor, and more of the line is suspended. Since one of the boundary conditions are coordinates at the fairlead, the solution converges back to the OpenFAST static solution at this point. The calculated forces at the fairlead is higher for the inelastic solution, since more of the line is suspended.

### 3.2.2 Elastic catenary solver

It proved much more difficult to make an elastic catenary solver. When trying to apply the same principles as for the inelastic, the result was two equations with two unknowns. This would normally be solvable, but when trying to solve for this using the Newton-Raphson method, it did not compute. I believe the reason for this is that the equations were not independent, meaning, in reality I only had one equation, but two unknowns. As a workaround, I proceeded to use what I call an Inelastic Combined Elastic, ICE, formulation. For this process, I start by solving the inelastic equation as above, before both the suspended line and the resting line is stretched based on the forces in the line found from the inelastic formulation. I then update the line length based on this, to re-calculate the inelastic solution. I let this run in a loop until the change in the suspended line-length is below a set limit. From this, I take the forces at the fairlead, and solve the elastic catenary equations using the forces.

Results from the ICE solver			
$a = 231.01$	$S = 347.33 \text{ m}$	$RL = 503.13 \text{ m}$	$TD = -334.47 \text{ m}$

Table 3.3: Results from ICE N-R.

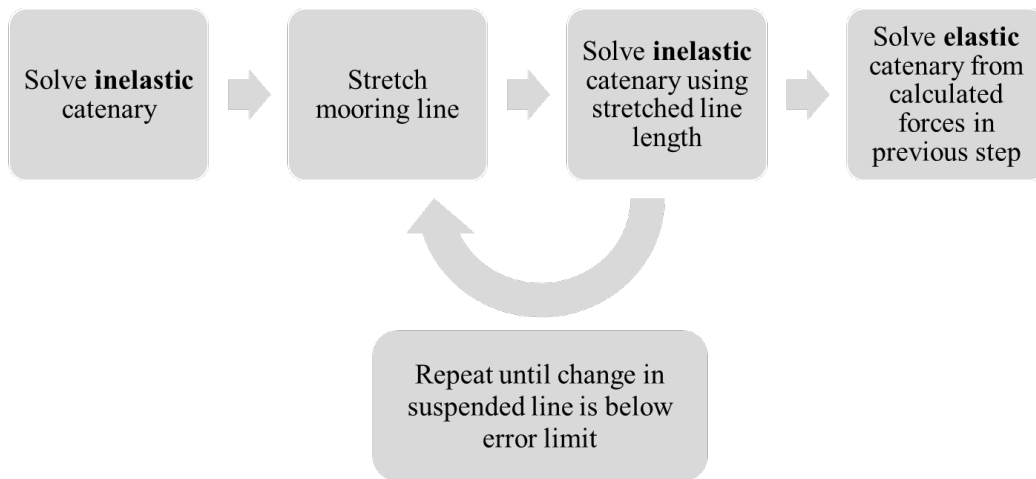


Figure 3.2: Flowdiagram showing the ICE procedure.

Using this solver, I can replicate the results from the OpenFAST's MAP++ solver. It is worth noticing that due to elasticity, the mooring line has stretched 46 cm, or equivalent to 0.05% elongation. It does not sound much, but it makes a much larger impact on the fairlead forces, which are reduced by 1.5% ( $F_x$ ) and 0.5% ( $F_y$ ).

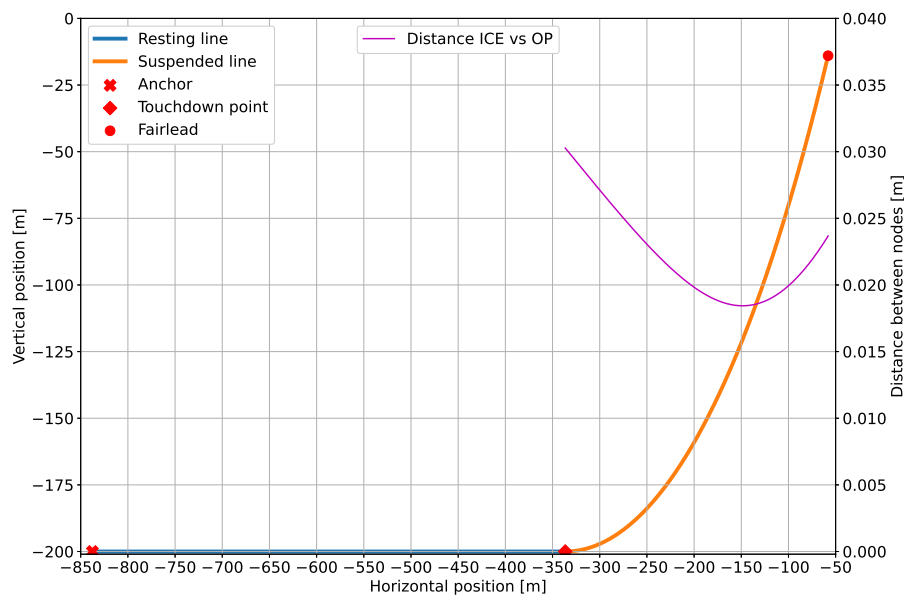


Figure 3.3: Figure showing the comparison between ICE and OpenFAST for mooring line 1.

Figure 3.3 shows that the offset between ICE and OpenFAST is less than 3 cm for the entire length of mooring line 1.

Simulation model	Resting line [m]	Resting line Error [m]	Fairlead X,Z [m]	Fairlead Force $F_x, F_z$ [kN]	Fairlead force Error [%]
MAP++	503.16	N/A	-58.00, -14.00	1350.01, 2028.16	N/a
Inelastic	501.06	2.10	-58.00, -14.00	1369.30, 2039.23	14.29 , 5.46
ICE	503.13	0.03	-58.01, -13.98	1350.06, 2028.34	0.04 , 0.09

Table 3.4: Comparison of the static results.

As seen in table 3.4, with the use of ICE, the positional data and fairlead forces from OpenFAST can be replicated to high level of accuracy. Also interesting to observe that the 46 cm of stretch shifts the touchdown point over 2m.

### 3.3 OpenFAST v.3.5.0

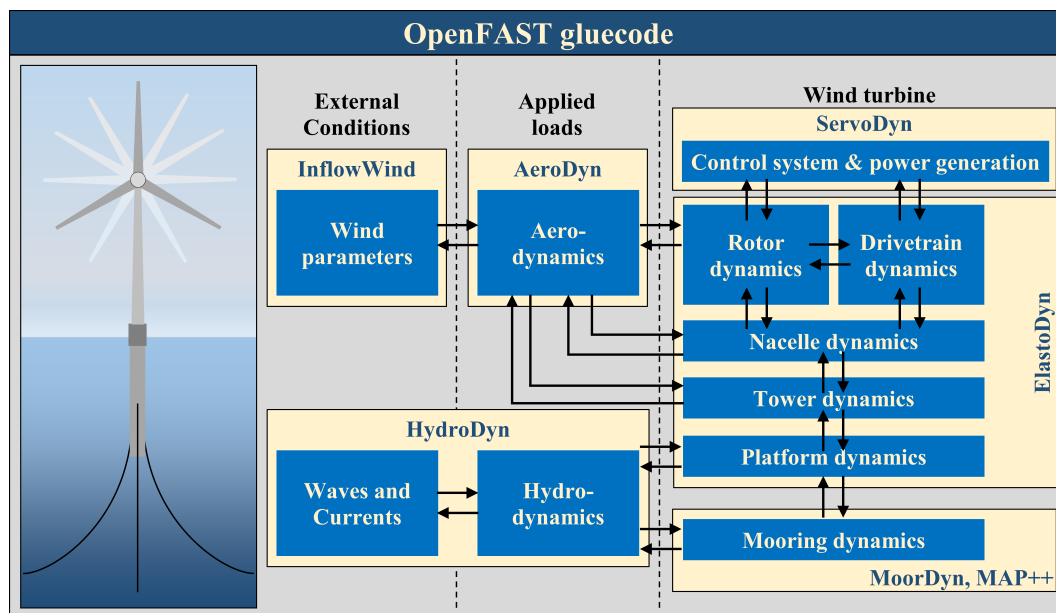


Figure 3.4: OpenFAST Modules, adapted from NREL / OpenFAST.

OpenFAST (Fatigue, Aerodynamics, Structures, and Turbulence) software is an open source code, supported by NREL (National Renewable Energy Laboratory). It is a comprehensive aeroelastic simulator, which has been continuously upgraded and maintained by NREL, and now also includes hydrodynamics for both offshore bottom fixed and floating structures. The main module, OpenFAST glue-code, allows for a combination of required sub-modules selected by the user depending on which simulations to be run. Figure 3.4 shows how the modules are connected. Below is a short description of the modules I have used for the simulations, and its possibilities.

#### InFlowWind

InFlowWind is the module that controls the wind. This can be steady wind, uniform wind with a shear profile, a binary wind field based on a turbsim input file, or another type of a binary input file. For my simulations, I have used binary turbsim input files. The turbsim input files have been generated for different loadcases using the stand-alone program TurbSim v2.00.

#### AeroDyn

InFlowWind is coupled to AeroDyn which is the aerodynamics module. This module will calculate the aerodynamic loads on both the blades and the tower of the wind turbine. The structure model is based on the actuator line model. Both the tower and the blades are modelled using lines and nodes. The local loads for each node is calculated using the Blade-Element Momentum Theory (BEMT) (Jonkman *et al.*, 2015).

#### ServoDyn

The controller system of the wind turbine is handled by ServoDyn in OpenFAST. This module includes blade pitch, nacelle yaw control and generator control with start-up and shut-down procedure (Jonkman and Buhl Jr, 2005).

### HydroDyn

HydroDyn is the hydrodynamics (wave and current) module in OpenFAST. It is used to generate waves and calculate the hydrodynamic loads on the structure. Waves can be generated as periodic, stochastic or long- or short-crested. Loads can be calculated in 3 different ways, either using potential flow theory, strip-theory (Morison) or a combination of the two. The module uses the JONSWAP/Pierson-Moskowitz spectrum for simulating irregular waves (*Jonkman, 2009*).

### MoorDyn

MoorDyn is one of three included mooring modules available in OpenFAST. The other two modules are MAP++ and FEAMooring. In addition OpenFAST can be coupled with OrcaFlex. MoorDyn is the most used dynamic mooring module, and is based on the lumped-mass dampener methodology as described in section 2.7.5.

### MAP++

MAP++ is OpenFAST's quasi-static mooring solver (*Masciola et al., 2013*). This module can be used for static analysis, but also as a quasi-static time marching analysis.

### ElastoDyn

ElastoDyn is the fatigue and loading simulation module. It looks at the structural dynamics of the rotor, drivetrain, nacelle, tower and platform. The loads from AeroDyn, HydroDyn, controller commands and substructure reactions are all loaded into ElastoDyn for the complete structural dynamics of the system. The module uses an ordinary differential equation (ODE) solver of the 4<sup>th</sup> order, which is selected by the user, to solve the EoM using Kane's method (*Jonkman and Jonkman, 2016*). The outputs from ElastoDyn are, among others, displacements, velocities, accelerations and reaction loads.

## 3.4 Advanced rod model

The advanced rod model computes the motion and stresses experienced by an initial straight, transversely isotropic rod. It may be considered as a special case of the static and dynamic variational principles of nonlinear Kirchhoff rods. The configuration space of the new advanced rod model is selected such that it disables shear, (*Gebhardt and Romero, 2021*), which is negligible for mooring lines. It also disregards any energetic contribution due to torsion, and as a Kirchhoff rod, its cross-section remains plane and normal to the tangent vector. The resulting formulation is of such format that it can be described completely by primal variables, and does not rely on dual variables such as Lagrange multipliers.

### 3.4.1 From advanced rod model to a mooring line analysis tool

The advanced rod model (ARM) has required several modifications to be able to be used as a mooring line simulator. Mooring lines, made of fibre rope, chain or steel wire, have very little bending stiffness. The regular catenary equations are totally neglecting bending stiffness. The static formulation for the new advanced rod model cannot have a zero bending stiffness, as this will lead to singular matrices in the computation. To avoid this issue, I have used a very low value of bending stiffness, to try to achieve a comparable result as OpenFAST. This is not an

issue for the dynamic formulation, due to inertia terms the bending stiffness can be set to 0 without having the issue with singular matrices.

Further more, one important attribution with mooring lines, is the resting line length, and the touchdown point for the mooring line at the seafloor. This characteristic is not captured in the static advanced rod model, as one of the inputs here is the suspended line length. To overcome this obstacle, a modification is done to the dynamic model. A barrier function is introduced, based on the work by *Roccia and Gebhardt (2023)*, which works by applying a vertical force which increases in strength the closer the line gets to the vertical position of the barrier. In section 4.1, I show the work carried out to attempt the use of alternative barrier functions to find in my opinion the best solution for simulating the mooring lines interaction with the seafloor.

In addition, the advanced rod model requires the rod, or in this case the mooring line, to be initially straight. To account for this in the static model, the line is initially laying horizontally on the seafloor, with one end clamped at the touchdown point, before a force at the free-end is applied. The force is increased in steps to avoid numerical instability. For the dynamic model, the rod is initially straight, at an angle between the anchor and the fairlead, before it is dynamically relaxed using a static force at the free end for 600 seconds of simulation time. After the initial 600 seconds of simulation time, the dynamic force is applied to the free end based on the simulation being run.

### 3.4.2 Mathematical formulation

In this section, I will give an introduction to parts of the mathematical formulation used for the ARM. The derivation of some of the vital operators and the EoM can be found in appendix A.

The new model is based on the research by *Romero and Gebhardt (2020)*, *Gebhardt and Romero (2021)* and *Roccia and Gebhardt (2023)*. It is a complex set of equations, based on a special case of Kirchhoff rod theory, where no torsion or shear is considered. Some of the mathematical and material properties used in the model have already been introduced in chapter 2.8.

#### Definitions

Configuration manifold:

$$\mathcal{L} := \{\varphi \in [C^2(0, S)]^3\}, BC : |\varphi'(s)| > 0, \varphi(0) = 0, \varphi'(0) = \mathbf{D} \quad (3.15)$$

$S$  is the total length of the rod, while  $s$  is the coordinate of the arc length, and is in the region of 0 to  $S$ ,  $s \in [0, S]$ . In the use of ARM as mooring line, the rod is clamped at  $s = 0$ .  $\varphi$  describes the current configuration, and is dependent on  $s$  and  $t$ , where  $t$  is time, defined as  $t \in [0, T]$ .

$$|\varphi'(s)| > 0 \quad (\text{this is a regular function}) \quad (3.16)$$

$$\varphi(0) = 0 \quad (\text{the function starts at zero}) \quad (3.17)$$

$$\varphi'(0) = \mathbf{D} \quad (\text{at zero the first derivative of } \varphi \text{ is along } E_3) \quad (3.18)$$

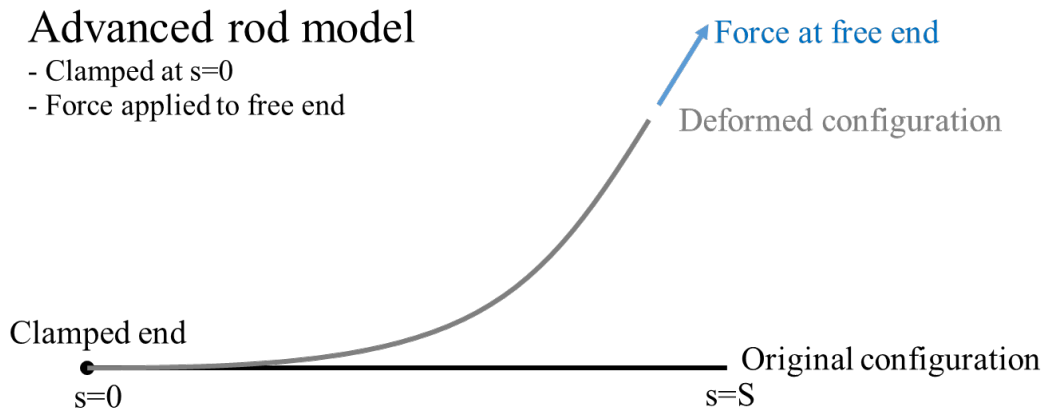


Figure 3.5: Simple drawing showing the original configuration and the deformed configuration.

$$\boldsymbol{\varphi} = \varphi^1 \mathbf{E}_1 + \varphi^2 \mathbf{E}_2 + \varphi^3 \mathbf{E}_3 \quad (3.19)$$

$$\boldsymbol{\varphi}_t(s) = \boldsymbol{\varphi}(s, t) \quad (3.20)$$

$$\boldsymbol{\varphi}_0(s) = s\mathbf{D} \quad (3.21)$$

The equation 3.21 reduces the class of allowable motion of the rod. Constant vector  $\mathbf{D}$  belongs on the unit sphere  $S^2 := \{\mathbf{d} \in \mathbb{R}^3 | \mathbf{d} \cdot \mathbf{d} = 1\}$ , and is known as the director. It describes the direction of the first derivative of  $\boldsymbol{\varphi}$ .

$$\mathbf{d} := \frac{\boldsymbol{\varphi}'}{|\boldsymbol{\varphi}'|}, \quad \mathbf{n} := \frac{\boldsymbol{\varphi}''}{|\boldsymbol{\varphi}''|}, \quad \mathbf{b} := \frac{\boldsymbol{\varphi}' \times \boldsymbol{\varphi}''}{|\boldsymbol{\varphi}' \times \boldsymbol{\varphi}''|} \quad (3.22)$$

Equation 3.22 is called the Frenet-Serret triad, and it satisfies  $\mathbf{b} = \mathbf{d} \times \mathbf{n}$ . Since  $\mathbf{d} := \frac{\boldsymbol{\varphi}'}{|\boldsymbol{\varphi}'|}$ , and  $|\mathbf{d}| = 1$ , which means  $\mathbf{d}$  is a unit vector. Thus as a requirement for this system of equations is that  $|\boldsymbol{\varphi}''| \neq 0$ .  $\mathbf{d}$  is the tangential vector,  $\mathbf{n}$  is the normal vector and  $\mathbf{b}$  is the binormal vector.

### Spatial strain measures:

Deformation modes that the system can handle is elongation and curvature. As previously mentioned, torsion is disregarded.

$$\boldsymbol{\varepsilon} := (|\boldsymbol{\varphi}'| - 1)\mathbf{d}, \quad \boldsymbol{\kappa} := \mathbf{d} \times \mathbf{d}' \quad (3.23)$$

Equation 3.23 defines the two *spatial* strain measures. Epsilon,  $\boldsymbol{\varepsilon}$ , is the axial strain, while kappa,  $\boldsymbol{\kappa}$ , is the bending strain.

### Stress measures:

The stress measures are calculated based on the spatial strain measures using the Young's modulus of the material,

$$\mathbf{n} = EA\boldsymbol{\varepsilon}, \quad \mathbf{m} = EI\boldsymbol{\kappa} \quad (3.24)$$

$\mathbf{n}$  describes the tangential stress measure, e.g. tension, while  $\mathbf{m}$  describes the bending stress measure.  $E$  is the Young's modulus,  $A$  is the cross-section of the rod, and  $I$  is the 2<sup>nd</sup> moment of area with regards to an axis contained in the cross-section.

**Energy:**

Stored energy of the rod can be described in two parts, the axial stored energy ( $U_a$ ) and the bending stored energy ( $U_b$ ),

$$U_a(\varepsilon) = \frac{1}{2}EA\varepsilon^2, \quad U_b(\kappa) = \frac{1}{2}EI\kappa^2 \quad (3.25)$$

Using the equations 3.25, I can now express the equations for kinetic and total potential energy:

$$T = \underbrace{\frac{1}{2} \int_0^L \dot{\boldsymbol{\phi}} \cdot \dot{\boldsymbol{\phi}} A_\rho ds}_{\text{translation energy}} + \underbrace{\frac{1}{2} \int_0^L \dot{\mathbf{d}} \cdot \dot{\mathbf{d}} I_\rho ds}_{\text{rotational energy}} \quad (3.26)$$

$$U = \underbrace{\frac{1}{2} \int_0^L \varepsilon \cdot \varepsilon E A ds}_{\text{axial tension energy}} + \underbrace{\frac{1}{2} \int_0^L \kappa \cdot \kappa E I ds}_{\text{bending energy}} \quad (3.27)$$

Equations 3.26 and 3.27 describes kinetic energy and the potential energy in the rod respectively. A simplistic view would be to consider the energy expressions as:  $T = \frac{1}{2}m\dot{x}^2 + \frac{1}{2}I\dot{\theta}^2$ , and  $U = \frac{1}{2}x^2 K_x + \frac{1}{2}\theta^2 K_\theta$ .

**Variational principle**

Since this model is based on the Lagrangian approach, which is a variational principle, it is required to find the variation in Kinetic and Potential energies. To express the variational energies I will use two operators, the Mass operator,  $\mathcal{M}$ , and the Strain operator,  $\mathcal{B}$ . The derivation of these are described in appendix A.

**Mass operator and the variation of kinetic energy:**

$$\begin{aligned} \mathcal{M}(\varphi') &= \left( (A_\rho \mathbf{I}) + I_\rho \partial s^T \left( \frac{\mathbf{I} - \mathbf{d} \otimes \mathbf{d}}{|\varphi'|^2} \right) \partial s \right) \\ T &= \frac{1}{2} \int_0^L \dot{\boldsymbol{\phi}} \cdot \mathcal{M}(\varphi') \dot{\boldsymbol{\phi}} ds \\ \delta \mathbf{T}(\varphi) &= - \int_0^S \delta \varphi \cdot \mathcal{M}(\varphi') \hat{\nabla}_\phi \dot{\boldsymbol{\phi}} ds \end{aligned} \quad (3.28)$$

**Linear strain operator and the variation of potential energy:**

$$\begin{aligned} \mathcal{B}(\varphi', \varphi'') \delta \varphi &= \begin{bmatrix} \delta \varepsilon \\ \delta \kappa \end{bmatrix} \\ \mathcal{B}(\varphi', \varphi'') &= \begin{bmatrix} \mathbf{I} - \frac{\mathbf{I} - \mathbf{d} \otimes \mathbf{d}}{|\varphi'|^2} & 0 \\ -\frac{1}{|\varphi'|^2} \left[ [\varphi'']_x [(\mathbf{I} - \mathbf{d} \otimes \mathbf{d}) + [\mathbf{d}]_x (2(\nabla_{\mathbf{d}'}(\varphi') \odot \mathbf{d})) \right] & [\mathbf{d}]_x \frac{\mathbf{I} - \mathbf{d} \otimes \mathbf{d}}{|\varphi'|^2} \end{bmatrix} \begin{Bmatrix} \mathcal{D}_1 \\ \mathcal{D}_2 \end{Bmatrix} \\ \delta \tilde{U}(\varepsilon, \kappa) &= \int_0^S \delta \varphi \cdot (\mathcal{B}(\varphi', \varphi'')^T \boldsymbol{\sigma}) ds \end{aligned} \quad (3.29)$$

The equations 3.28 and 3.29 can then be used in the derivation of the EoM for rod using the stationary action principle,

$$\mathcal{I} = \int_0^T \mathcal{L}(\varphi', \boldsymbol{\phi}, \varphi'', \dot{\boldsymbol{\phi}} : t) dt = \int_0^T [T(\varphi', \boldsymbol{\phi}, \dot{\boldsymbol{\phi}} : t) - U(\varphi', \varphi'' : t)] dt. \quad (3.30)$$

The weak Euler-Lagrange equation corresponding to the functional is,

$$\int_0^S \delta \varphi \cdot \left( \mathcal{M}(\varphi') \hat{\nabla}_{\dot{\varphi}} \dot{\varphi} + \mathcal{B}(\varphi', \varphi'')^T \sigma \right) ds = 0. \quad (3.31)$$

The strong form of equation of motion for the Kirchhoff rod can be recovered from the variational equation 3.31 as follows,

$$\mathbf{n}' + \left( \frac{1}{|\varphi'|} \mathbf{d} \times \nabla_{\mathbf{d}'} \mathbf{m} \right)' = \dot{\mathbf{p}} + \left( \frac{1}{|\varphi'|} \mathbf{d} \times \nabla_{\mathbf{d}} \pi \right)', \quad (3.32)$$

where  $\mathbf{n}$  and  $\mathbf{m}$  are stress measures as introduced in 3.24, while  $\mathbf{p}$  and  $\pi$  are the momenta. The definition for the momenta are,

$$\mathbf{p} = A_\rho \dot{\varphi} \text{ and } \pi = I_\rho \dot{\mathbf{d}}, \quad (3.33)$$

where  $A_\rho$  is the density pr. unit length and  $I_\rho$  is the inertia density pr. unit length.

These equations are based on no external forces. For a mooring line, several external forces are present, gravity, buoyancy, drag etc. These need to be derived and introduced by using the virtual work principle into the variational equation of motion 3.31.

### 3.4.3 Forces in ARM

The current version of ARM includes four forces on the line:

- Fluid force, including added mass force and drag force, both tangential and normal
- Gravitational force
- Buoyancy
- The input force at the free-end

The fluid force is the only damping force currently implemented in ARM, and as thus plays a vital role. As mentioned, the fluid force can be split into three components (*Nguyen et al., 2023*),

$$F_f = \underbrace{C_1 a_N}_{\text{Added mass}} + \underbrace{C_2 |V_N| V_N}_{\text{Normal drag}} + \underbrace{C_3 |V_T| V_T}_{\text{Tangential drag}}, \text{ where} \quad (3.34)$$

$$C_1 = \frac{1}{4} \pi C_M \rho_f \varnothing^2$$

$$C_2 = \frac{1}{2} C_N \rho_f \varnothing$$

$$C_3 = \frac{1}{2} C_T \rho_f \varnothing,$$

where  $C_M$  is defined as the added mass coefficient, which is determined by the cross-section and length of the system, and can be found from tables such as *DNV RP-C205 (2014)*.  $C_N$  and  $C_T$  are the normal and tangential drag coefficients, both determined experimentally, and dependent on Reynolds number.  $\rho_f$  is the density of the flowing fluid around the rod, while  $\varnothing$  is



the diameter of the cylindrical cross-section of the rod. In addition,  $a$  and  $V$  are the acceleration and velocity respectively, and can be expressed as follows:

$$\begin{aligned}\mathbf{a}_N &= \mathcal{P}_d \mathbf{a} \\ \mathbf{V}_N &= \mathcal{P}_d \mathbf{V} \\ \mathbf{V}_T &= (\mathbf{d} \otimes \mathbf{d}) \mathbf{V}\end{aligned}$$

Where  $\mathcal{P}_d$  is the orthogonal projector and  $\mathbf{d} \otimes \mathbf{d}$  is the tangential projector. The velocity vector consist of two elements, the free stream velocity, which for a mooring line would be the ocean current or tidal current velocity, and the velocity of the rod  $\dot{\phi}$ , similarly the acceleration vector consist of the time derivative of the free stream velocity and the rod acceleration  $\ddot{\phi}$ . The buoyancy force is given by,

$$F_b = \int_0^S \rho_w \mathbf{g} A ds, \quad (3.35)$$

where  $\mathbf{g}$  is the gravity constant,  $A$  is the cross section of the rod and  $\rho_w$  is the density of the fluid. Similarly the gravity force is given by,

$$F_g = - \int_0^S \rho_{rod} \mathbf{g} A ds, \quad (3.36)$$

where  $\rho_{rod}$  is the density of the rod.

In addition to the fluid force, gravity force and the buoyancy force, the force at the free end is required. The free end force is extracted from the OpenFAST simulation and converted to the correct time-step. It is input into ARM as a txt file containing 3 columns,  $F_x$ ,  $F_y$  and  $F_z$ .

The external forces are summed, and input in the EoM (3.32) for the rod, such that for the strong form the EoM becomes

$$\mathbf{n}' + \left( \frac{1}{|\phi'|} \mathbf{d} \times \nabla_{\mathbf{d}'} \mathbf{m} \right)' = \dot{\mathbf{p}} + \left( \frac{1}{|\phi'|} \mathbf{d} \times \nabla_{\mathbf{d}} \pi \right)' - \mathbf{f}^{\text{ext}} \quad (3.37)$$

Due to the nature of the velocity and acceleration components, current forcing can easily be introduced in future version of the model.

### 3.4.4 Derivation of the barrier function

In addition to introducing the external forces, a mooring line simulator requires modelling of the seafloor contact. The seafloor contact model is required to handle the interaction between the mooring line and the seafloor, and to allow for the mooring line to rest at this depth. To introduce the barrier in the advanced rod model, a functional is introduced. The below derivation is based on the work of *Roccia and Gebhardt (2023)*,

$$\begin{aligned}\mathcal{H} &= \int_0^S \mathcal{g}(C) ds, \text{ where} \\ C &= \boldsymbol{\varphi} \cdot \mathbf{E}_3 - Z_0 > 0,\end{aligned} \quad (3.38)$$

Equation 3.38 is the integration of the barrier function,  $\mathcal{g}$ , over the length of the rod.  $C$  is the constraint to be imposed on the mooring line, while  $Z_0$  is the vertical coordinate of the seafloor, with respect to the global reference frame. To be able to use the functional in the EoM, we need to derive the variation of  $\mathcal{H}$ ,

$$\delta \mathcal{H} = \delta \int_0^S \mathcal{g}(\boldsymbol{\varphi} \cdot \mathbf{E}_3 - Z_0) ds \quad (3.39)$$

$$= \int_0^S \delta \mathcal{g}(\boldsymbol{\varphi} \cdot \mathbf{E}_3 - Z_0) ds, \quad (3.40)$$

where,

$$\begin{aligned}
 \delta \mathcal{G}(\boldsymbol{\varphi} \cdot \mathbf{E}_3 - Z_0) &= \partial_{\boldsymbol{\varphi}}(\boldsymbol{\varphi} \cdot \mathbf{E}_3 - Z_0) \cdot \delta \boldsymbol{\varphi} \\
 &= \partial_z [\mathcal{G}(z)]|_{z=C} \partial_{\boldsymbol{\varphi}}(\boldsymbol{\varphi} \cdot \mathbf{E}_3 - Z_0) \delta \boldsymbol{\varphi} \\
 &= \partial_z [\mathcal{G}(z)]|_{z=C} \partial_{\boldsymbol{\varphi}^a}(\boldsymbol{\varphi} \cdot \mathbf{E}_3 - Z_0) \mathbf{E}_a \delta \boldsymbol{\varphi} \\
 &= \partial_z [\mathcal{G}(z)]|_{z=C} \mathbf{E}_3 \cdot \delta \boldsymbol{\varphi},
 \end{aligned} \tag{3.41}$$

thus 3.40 becomes

$$\delta \mathcal{H} = \int_0^S \delta \boldsymbol{\varphi} \cdot \partial_z [\mathcal{G}(z)]|_{z=C} \mathbf{E}_3 ds. \tag{3.42}$$

The barrier function needs to be calibrated, or tuned, to achieve a sufficient barrier at the specified depth,  $z_0$ , and to avoid introducing instabilities in the formulation. The barrier parameter,  $\mu$ , is a user defined, positive penalty parameter. For the simulation of the mooring line, I have used  $\mu$  as a fraction of the density of the mooring line. This way it would be possible to only change the density of the mooring line, and the barrier parameter will change accordingly. The specified depth,  $z_0$ , cannot be placed at the exact place where the barrier should be, due to the nature of the logarithmic function. Instead it has to be placed a certain distance below where the barrier should be. For my simulation I have used an offset distance of -0.2m to -0.5m.

In the ARM matlab code, the barrier function is split into 3 parts.  $G(z)$ , which is the actual barrier function. This may be thought of as the work of the barrier force. The first derivative of  $G(z)$  with respect to  $z$ ,  $\frac{dG(z)}{dz}$ , which is the force from the barrier function, and the second derivative of  $G(z)$  with respect to  $z$ ,  $\frac{d^2G(z)}{dz^2}$  which is the potential associated to the barrier force.

### 3.4.5 Tuning of the barrier function

I have run a set of dynamic relaxation tests on the dynamic code to test and calibrate the barrier function. Two different scenarios were tested. The first scenario has the line hinged at the anchor, and a force at the free end from the OpenFAST static fairlead tension result. The second scenario has the line hinged at the fairlead, and a horizontal force at the free end, equal to the force at anchor from the OpenFAST static tension result. By calibrating the barrier function I can get results from both scenarios similar to the static solution from OpenFAST, see figure 3.6a.

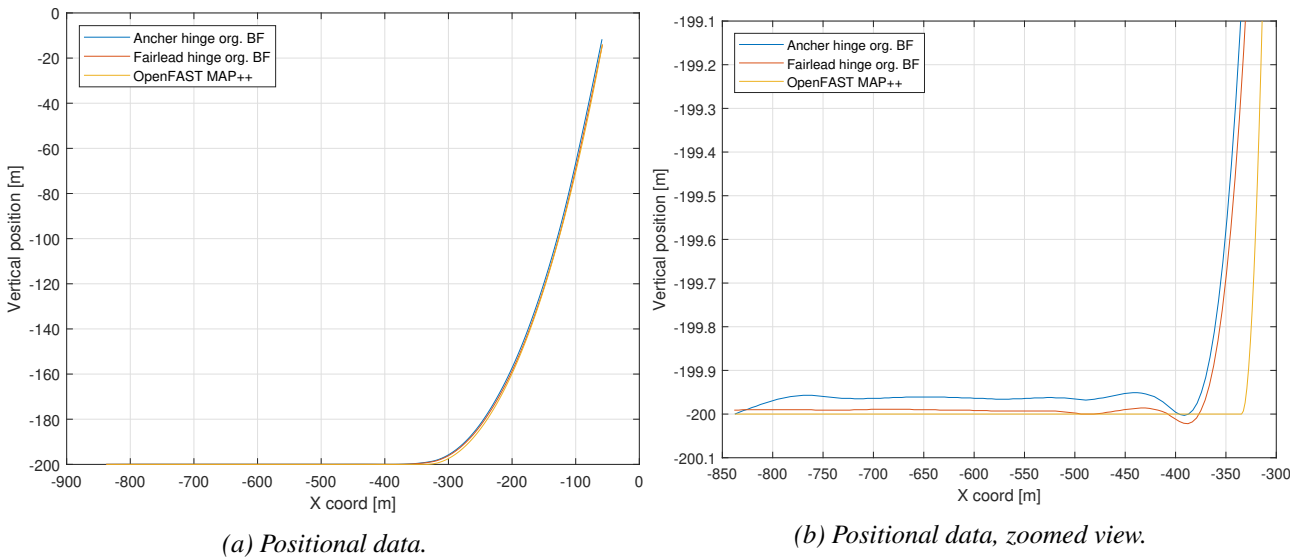


Figure 3.6: Comparison of OpenFAST static results and ARM hinged at fairlead and at anchor.

What is important to notice here, is that due to the barrier function, it seems that the touchdown point of the mooring line for both static ARM simulations does not match the static solution from OpenFAST MAP++, even after calibrating the barrier parameter and barrier depth. There seems to be a horizontal offset of approximately 40m. I believe the reason for this is the nature of the barrier function, lifting the line above the seafloor. This will lift the mooring line, and shift the touchdown point. This can be seen in figure 3.6b where I compare ARM dynamic relaxation with static results from OpenFAST MAP++.

Another point of interest is that setting the anchor as hinge point and applying the tension force at the free end does not give the correct coordinate for the fairlead, see table 3.5. While on the other hand, setting the fairlead as hinge point and the horizontal force at anchor at the free end will place the anchor at the correct coordinate within a few cm of difference.

Simulation model	Anchor X,Z [m]	Resting line [m]	Resting line Error [m]	Fairlead X,Z [m]
MAP++	-837.60, -200.00	503.16	N/A	-58.00, -14.00
ARM Anchor hinge	-837.60, -200.00	467.6	35.56	-58.56, -12.04
ARM Fairlead hinge	-837.75, -199.85	471.6	31.56	-58.00, -14.00

Table 3.5: Anchor and fairlead coordinates for dynamic relaxation.

### Testing of alternative barrier functions

I have worked on the formulation of the barrier function, to see if I could improve the positional result of the new model. The idea here is to try to let the barrier force decline much faster as a function of the line distance from the barrier depth.

Original formulation for  $G$ ,

$$G(z) = -\mu \log(z) \quad (3.43)$$

$$\frac{dG(z)}{dz} = -\frac{\mu}{z}$$

$$\frac{d^2G(z)}{d^2z} = \frac{\mu}{z^2}$$

Alternative 1 -  $G_1$ ,

$$G(z) = \frac{\mu}{z} \quad (3.44)$$

$$\frac{dG(z)}{dz} = -\frac{\mu}{z^2}$$

$$\frac{d^2G(z)}{d^2z} = 2\frac{\mu}{z^3}$$

Alternative 2 -  $G_2$ ,

$$G(z) = \frac{\mu}{3z^3} \quad (3.45)$$

$$\frac{dG(z)}{dz} = -\frac{\mu}{z^4}$$

$$\frac{d^2G(z)}{d^2z} = 4\frac{\mu}{z^5}$$

I tried two different alternative barrier functions, alternative 1 shown in equation 3.44 and alternative 2 shown in equation 3.45, which I compared to the original barrier function shown in equation 3.43.

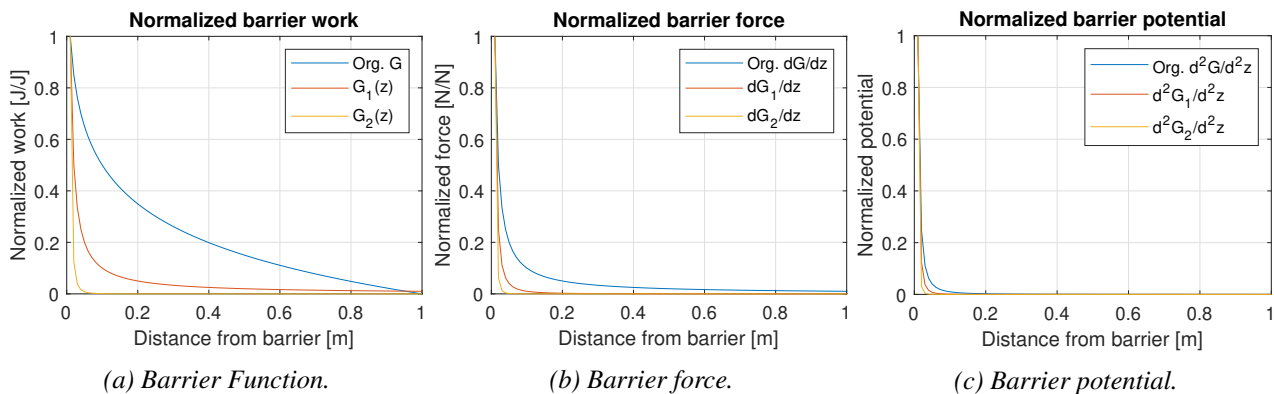


Figure 3.7: Comparison of barrier functions, original and alternative 1 and 2.

Figure 3.7 shows the comparison of the 3 different barrier functions, the barrier force, and the barrier potential. It is worth noting that the alternative barrier functions, 3.44 and 3.45, are valid only for as long as the line z-position does not pass the barrier depth. As seen in figure 3.7a, the force has a much steeper drop off for alternative 1 and 2 compared to the original. I found that alternative 1, 3.44, worked good, and comparing the ARM dynamic relaxing versus MAP++ static results yielded a close to identical result.

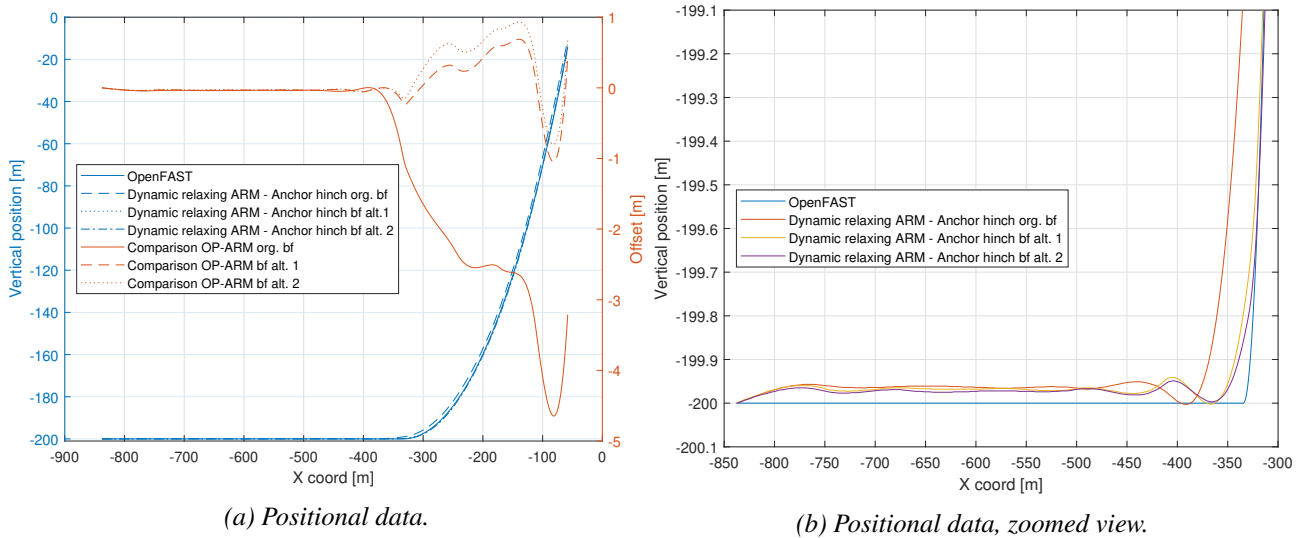


Figure 3.8: Comparison of barrier functions effect on line distribution.

Simulation model	Resting line [m]	Resting line Error [m]	Fairlead X,Z [m]	Fairlead pos. Error [m]
MAP++	503.16	N/A	-58.00, -14.00	N/A
ARM Anchor hinge org. BF	467.6	35.56	-58.56, -12.04	2.04
ARM Anchor hinge alt. 1 BF	494.6	8.56	-58.08, -14.54	0.55
ARM Anchor hinge alt. 2 BF	494.6	8.56	-58.08, -14.78	0.78

Table 3.6: Anchor and fairlead coordinates for dynamic relaxation

From table 3.6, it can be observed that both alternatives provide better results than the original barrier function, but alternative 1, 3.44, performs slightly better. Fairlead positional error for alternative 1 reduced compared to the original and alternative 2. For the dynamic simulations in chapter 4 I have chosen to use alternative 1 for the barrier function, as this alternative showed the best results for comparison with OpenFAST, and also that this had the most simplistic equation design. Due to the nature of a mooring line, the rod will be clamped at the anchor for the dynamic simulations.

# Chapter 4

## Results

This chapter presents the results from the OpenFAST simulations and the ARM simulations. For the static simulations and the dynamic relaxation, load case 7, I have only studied the position and tension of mooring line 1. Mooring lines 2 and 3 would show a similar response due to the nature of the mooring layout symmetry, 2.9. For the dynamic simulations, load case 8 through 11, I will investigate the response on all 3 mooring lines. For load cases with wind and wave loads, it is important to remember that the wind and wave inflow angle is  $0^\circ$ .

### 4.1 Static simulation

For the static simulation, I have been focusing on mooring line 1, which has anchor and fairlead coordinates as stated in table 2.5. For the OpenFAST static results, I have used the quasi-static mooring simulator MAP++, Mooring Analysis Program. The output from MAP++ was then used in the elastic catenary formulation to get the line distribution. The outputs used from MAP++ are the resting line length and fairlead force. In addition, the mooring line properties from table 2.6 are required in the elastic catenary equations.

To run the ARM static model, the inputs required are similar to the inputs for the elastic catenary equation, and are obtained from MAP++. The static ARM is only able to output the line distribution, tension is not analysed for this case. The line distribution was compared to OpenFAST and to my own static code, ICE. As previously mentioned, the static ARM simulator requires a bending stiffness  $> 0$  to avoid singular matrices. Since MAP++ and ICE does not account for bending stiffness, I reduced the area moment of inertia to 0.1% of the actual area moment of inertia. By doing so, I reduced the bending stiffness to a minimum without experiencing numerical instability in the simulation.

The required inputs for the self-designed ICE mooring simulator, from section 3.2.2, are mooring line properties and coordinates of anchor and fairlead. The three different static simulators were compared in figure 4.1, and showed very similar positional results.

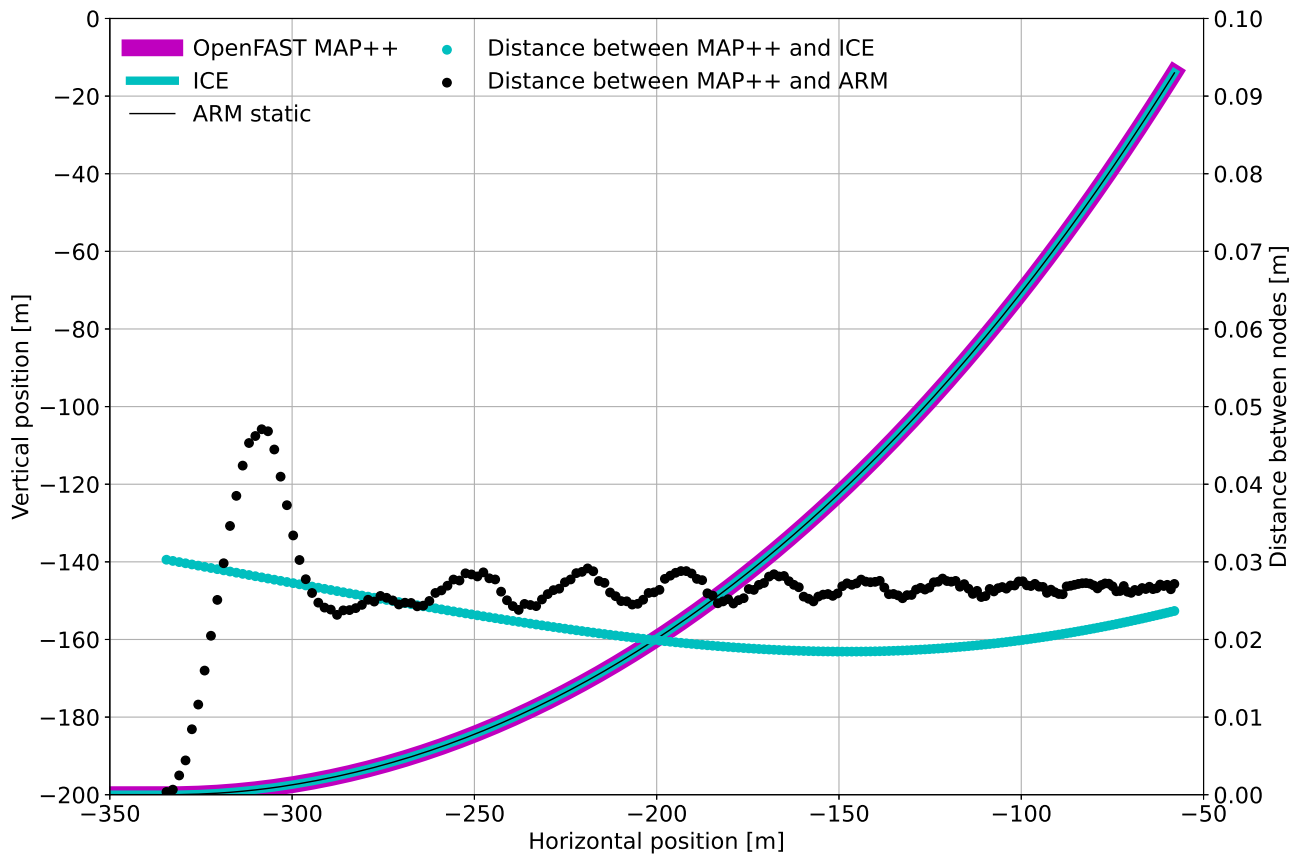


Figure 4.1: Static solvers, with distance between nodes on right axis.

The positional data from all three models are showing overlapping results, and a maximum positional error in the area of 3-5 cm. The ARM static results starts to differ from the OpenFAST results directly from the touchdown point, but then converges back and levels out with an offset of less than 3 cm, which is similar to the ICE simulator.

Simulation model	TD coordinate X,Z [m]	Fairlead coordinate X,Z [m]	Fairlead Force $F_x, F_z$ kN
OpenFAST MAP++	-334.44, -200.00	-58.00, -14.00	1350.01, 2028.16
ICE	-334.47, -200.00	-58.01, -13.98	1350.06, 2028.34
ARM static	uses MAP++	-58.00, -14.03	uses MAP++

Table 4.1: Static solvers results

### New static simulation with new FEM discretization

After the discovery of improved results by ARM with increased polynomial degree and continuity order for the FEM discretization in section 4.3.1, I decided to perform the static simulation again, with the new discretization. During the dynamic relaxation, load case 7, I observed instability in the tension results from the ARM model, especially around node 181, which can be observed on figure 4.5. This lead me to attempt several different tweaks on the model to achieve a more stable tension result. During this work, I found that the FEM discretization played a big role in the models stability, and by changing the polynomial degree from 3<sup>rd</sup> to 5<sup>th</sup> and the continuity order from 1<sup>st</sup> to 2<sup>nd</sup> improved the stability of the model significantly for the tension results. But, this change also improved the positional data slightly. For this reason, I wanted to revisit the static simulation. I have re-run the ARM static simulation with the new FEM discretization, and the result is shown in figure 4.2.

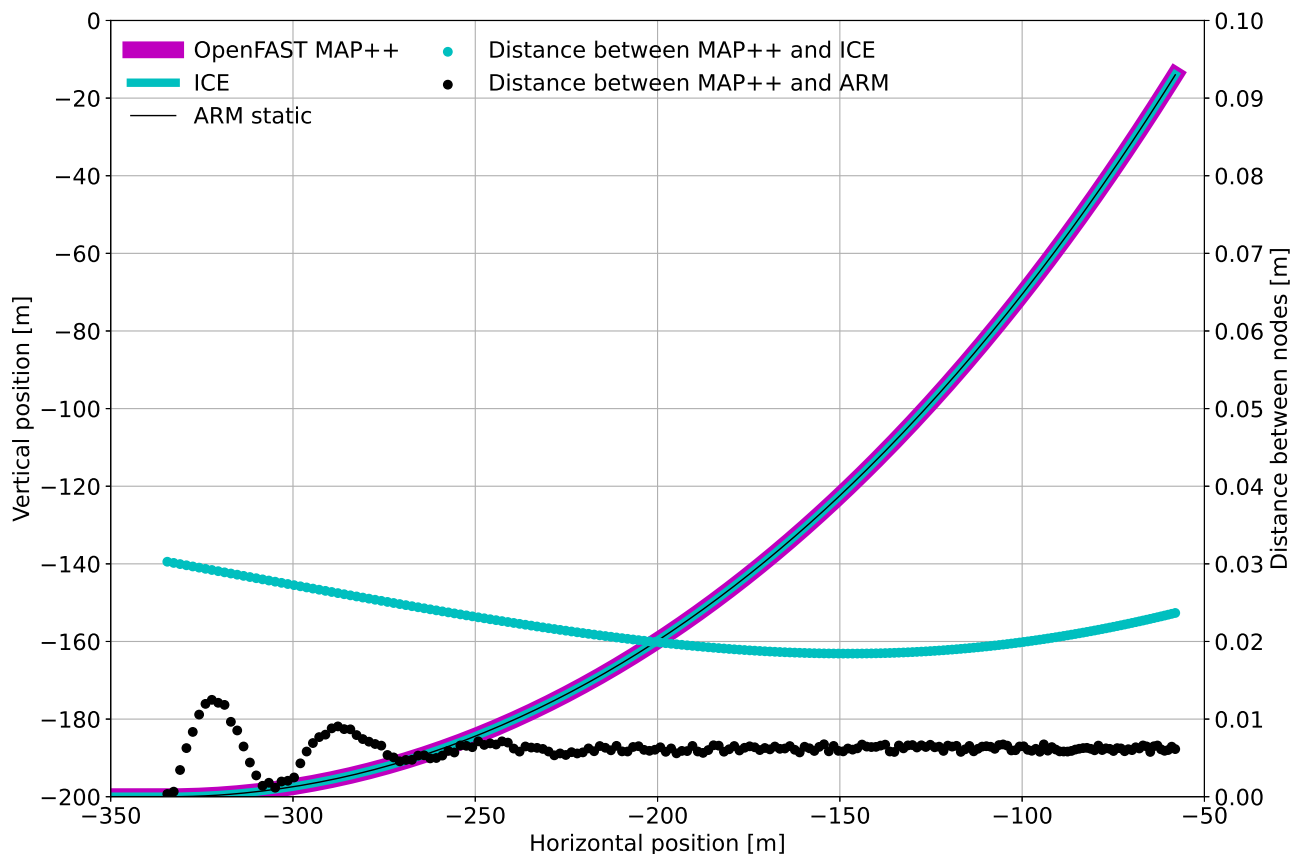


Figure 4.2: Static solvers, with distance between nodes on right axis. Increased polynomial degree.

The new results from the static solver confirms what was observed in the dynamic simulations. There is a slight instability at the touchdown point, but in general, increasing the polynomial degree and continuity order improves the result, reducing the offset between OpenFAST and ARM to below 1 cm, and the hump in the offset distance with original discretization at  $X \approx -320\text{m}$  has almost vanished. This agrees with the dynamic results, and shows that the FEM discretization is important for the accuracy of ARM model.

## 4.2 Model verification in OpenFAST

The current version when this thesis was started was OpenFAST v.3.5.0, which is not the same as was used by University of Maine when the design of the VoltturnUS-S was analysed in the definition (Allen *et al.*, 2020). The results from the definition was generated in 2020, using a previous version of OpenFAST. The definition does not state which version of OpenFAST was used. To verify that the version of OpenFAST I am using together with the VoltturnUS-S model will perform as expected, I have run 6 verification simulations to replicate the results from the definition by UMaine / NREL. The results of the verification can be found in the first part of the results chapter 4.

### 4.2.1 Load case 1 to 6 - Natural frequencies and damping ratio's

Load cases 1 to 6 are run in a no-wind and no-wave environment. These simulations are performed to replicate the decay frequencies and damping ratios that was reported in the definition (Allen *et al.*, 2020). These load cases are the free-decay simulations, where I analyse the natural frequency and dampening ratio for all the 6 DOF of the FWT, one simulation for each DOF. The structure is offset in the DOF being investigated, before it is released, and free to move. Initial offsets are as follows

DOF	Surge	Sway	Heave	Pitch	Roll	Yaw
Offset	30m	30m	5m	10 °	10 °	5 °

Table 4.2: Initial offset for free-decay tests.

Each simulation is run for 1500 seconds. The model will oscillate in the DOF at its natural frequency. From the results of these simulations, I have plotted the motion, damping ratios and natural frequencies for each of the 6 DOF. Based on the oscillations from the motion, I have found the natural frequency for each DOF by using the normalized fast fourier transform (FFT) method. The plots are shown in figure 4.3. The first column in figure 4.3 displays the the motion being analysed, and the middle column the damping ratio, while the third column shows the FFT of the motion to find the natural frequency. Surge and sway are the slowest motions, where one oscillation takes over 2 minutes. Heave is the quickest, where one oscillation takes just over 20 seconds.

Rigid-Body Model	Technical report	Personal results
Surge	0.007 Hz	0.007 Hz
Sway	0.007 Hz	0.007 Hz
Heave	0.049 Hz	0.049 Hz
Roll	0.036 Hz	0.035 Hz
Pitch	0.036 Hz	0.035 Hz
Yaw	0.011 Hz	0.012 Hz

Table 4.3: Comparison of natural frequencies

The results are shown in table 4.3, which also compares my results with the results from UMaine / NREL (Allen *et al.*, 2020). The results from the free-decay simulations have a good comparison with the technical report (Allen *et al.*, 2020), I only observe a fractional difference in the three rotational DOF. I believe this difference either is due to my simulations run on a newer version of OpenFAST, or can potentially be a rounding error from the calculations of the frequencies.



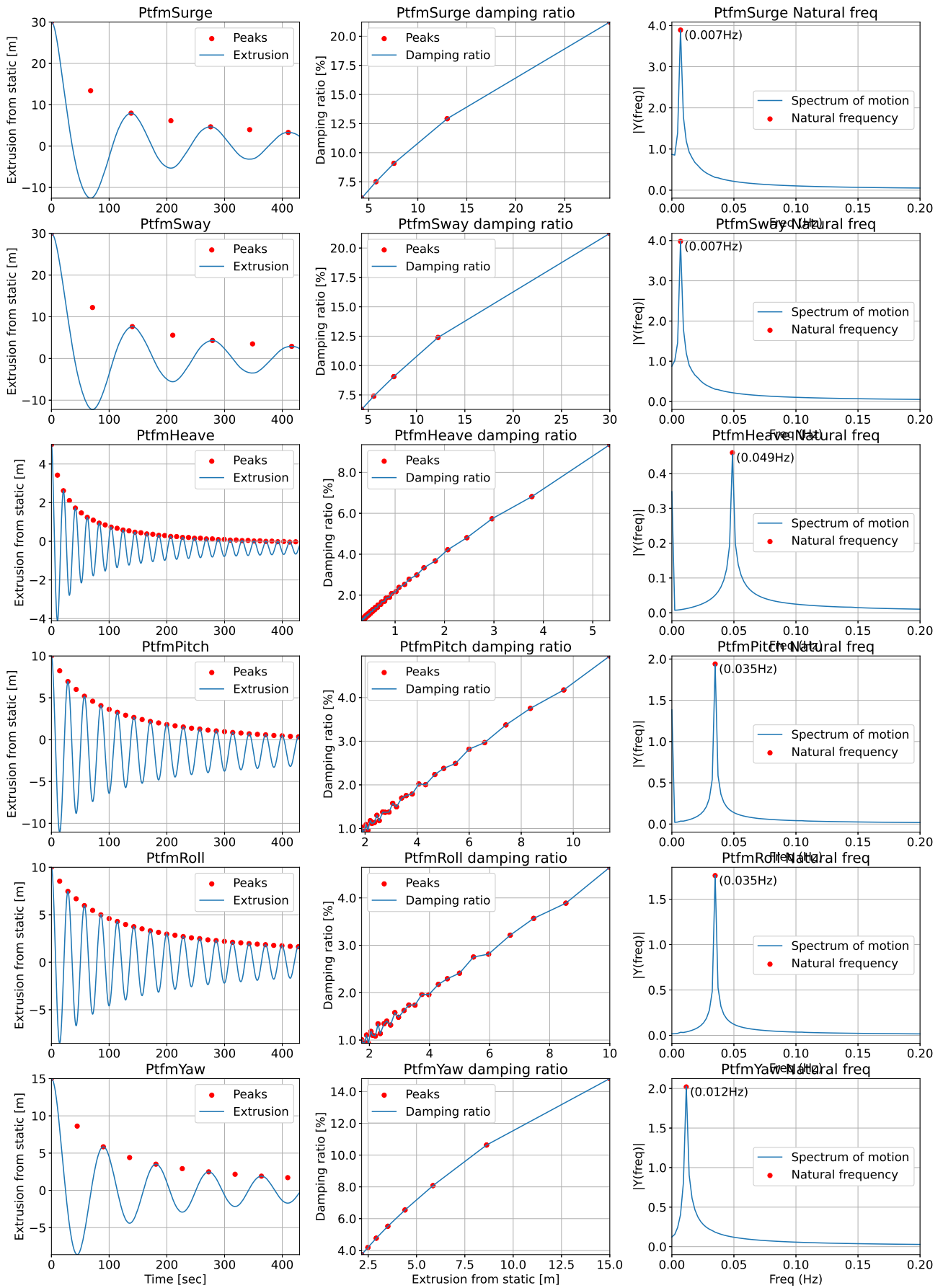


Figure 4.3: Natural frequencies and damping ratio for 6 DOF

## 4.3 Simulations for comparison of OpenFAST and ARM

For these simulations MoorDyn was chosen as the dynamic mooring simulator in OpenFAST. For the load cases 8 through 11, all three mooring lines were examined, for both dynamic loads and position using both OpenFAST MoorDyn and ARM. The fairlead force is taken from the OpenFAST simulations, and reworked to match the time-step in the ARM simulation. For most simulations, this means taking the OpenFAST data at 0.01 s time-step, and converting to ARM's 0.1 s time-step. In addition, ARM requires the force at the middle of time-steps, not at the time-step, such that the force is at time-step  $n + \frac{1}{2}$ .

To simplify the comparison between mooring lines 1,2 and 3, I decided to reduce the positional data from 3-D to 2-D. To do this I vector sum the X and Y coordinate of each line to get the horizontal position. The origin of the horizontal coordinate is the static platform center, meaning that the static horizontal position of each fairlead is 58m, 2.9, while the anchor is at horizontal coordinate 837.6m.

### 4.3.1 Load case 7 - dynamic relaxation

Load case 7 is simulated to find the static equilibrium, letting the FWT dynamically relax to a static position, and is simulated in a no-wind and no-wave environment. The OpenFAST simulation was run over 7200 sec, where the FWT are subjected to still wind and still sea. The first 6600 seconds of the OpenFAST result is skipped to avoid start-up errors and to let the motion of the platform be damped as much as possible, before taking the mean of the positional data of the remaining 600 seconds of data.

#### Results from the OpenFAST dynamic relaxation simulation

Translational position		Rotational position	
Surge	0.406m	Pitch	-1.403°
Sway	0.000m	Yaw	-0.000°
Heave	-0.355m	Roll	-0.000°

Table 4.4: Static position after dynamic relaxation

The platform's relaxed position is shifted slightly from its initial position. It is worth noting the negative pitch observed. I believe this is due to the large overhang of the rotor at the hub, causing the platform to pitch forward. When the turbine experiences a thrust force due to wind, I believe the pitch will level out. A negative platform pitch for a no-wind scenario is positive for the energy production since it will avoid the platform pitching backwards when the turbine is operating.

Fairlead 1 [kN]		Fairlead 2 [kN]		Fairlead 3 [kN]	
CON1FX	1340.65	CON3FX	-670.33	CON5FX	-670.33
CON1FY	-0.00	CON3FY	-1163.27	CON5FY	1163.27
CON1FZ	2010.35	CON3FZ	2026.96	CON5FZ	2026.96
Fairlead 1 tension	2416.37	Fairlead 2 tension	2431.28	Fairlead 3 tension	2431.28

Table 4.5: Forces at fairlead averaged over the last 600 seconds of dynamic relaxation.

As can be seen in table 4.5 the fairlead forces change slightly compared to the static results in table 4.1. This is due to the change of platform position, mostly platform pitch, which moves

the fairlead positions. As mentioned in section 2.7.1, pretension is normally kept at 10-20% of the minimum breaking load. For this model, the pretension is around 11%, which seems like a reasonable value based on the recommendation.

Fairlead 1 [m]		Fairlead 2 [m]		Fairlead 3 [m]	
Node200px	-57.23	Node200px	29.75	Node200px	29.75
Node200py	0.00	Node200py	50.23	Node200py	-50.23
Node200pz	-15.83	Node200pz	-13.61	Node200pz	-13.61
Offset from static	1.98	Offset from static	0.84	Offset from static	0.84

Table 4.6: Dynamic relaxed fairlead coordinates.

The fairlead's new relaxed position is shown in table 4.6. The overhang of the rotor which pitches the platform forward, moves the fairlead position for line 1 about 2m and about 1m for line 2 and 3.

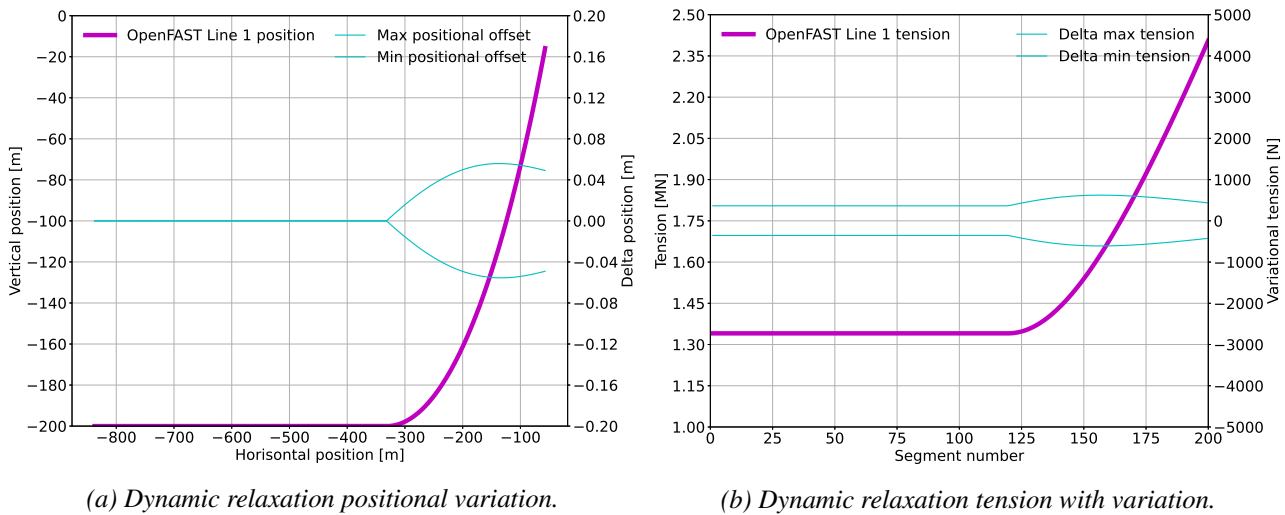


Figure 4.4: OpenFAST results.

Even after 6600 seconds, the platform has not come to complete rest. The figures 4.4a and 4.4b shows the mean position and tension over the last 600 seconds of simulation time, and the variation in position and tension. The mean position and tension is used as a static reference in load case 9 to 11.

## ARM results

The ARM simulation is run with a constant force at the free end, corresponding to the force for Fairlead 1 in table 4.5. The mooring line is clamped at the anchor, and the static force applied to the free end. The simulation is run for 1800 seconds. The first simulation showed a good comparison with the line positional distribution, but the distributed line tension,  $n_{stress}$  (3.23), showed an unstable response. The  $n_{stress}$  showed a large peak at node 181, or around 769m from the anchor. I have investigated this issue to see if I could explain the behaviour. The first I tried was to increase the number of nodes, to see if the peak shifted. By changing from 200 nodes to 850 nodes, the peak was not shifted significantly, leading me to believe that the nodal resolution was not the reason for the instability. Next step was to check if by increasing the coefficient of fluid dampening would reduce the instability, but unfortunately it did not. Finally, I tried to change the FEM discretization of the rod, by increasing the polynomial degree, and the continuity order. I increased the polynomial degree from cubic to quintic (3<sup>rd</sup> to 5<sup>th</sup> degree),

and the continuity order from 1<sup>st</sup> degree to 2<sup>nd</sup> degree. This gave a much more stable  $n_{stress}$ , but introduced some instability at the touchdown point. It may seem as the instability shifted position on the line.

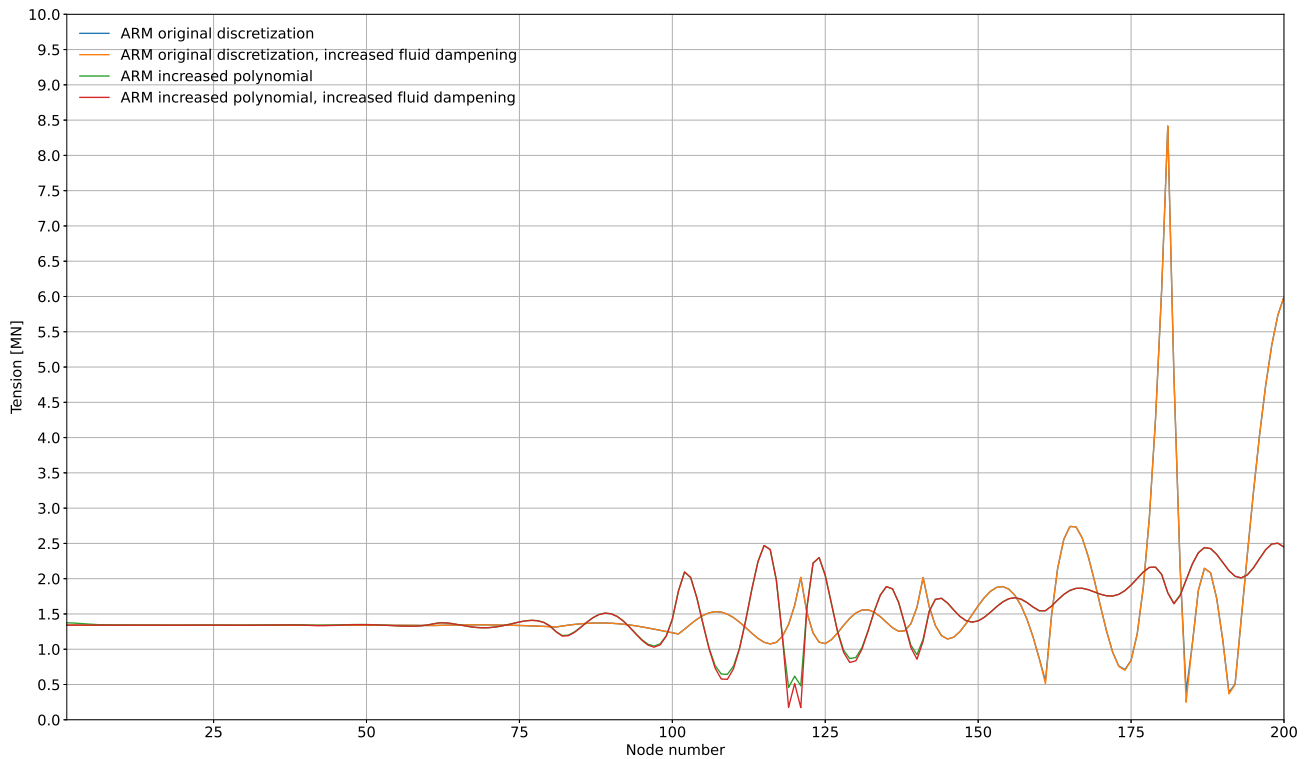


Figure 4.5: Comparison of 4 different ARM simulations with same force input.

Figure 4.5 shows 4 simulations, all run for 1800 seconds simulation time,  $n_{stress}$  averaged for each segment over the last 600 seconds. As can be seen, there is very little difference with the change of coefficient of fluid dampening with regards to  $n_{stress}$ . The curves with increased fluid dampening are overlapping with the normal fluid dampening coefficients for the same polynomial degree and continuity order. The result from the quintic polynomial shows a  $n_{stress}$  at the free end of 2.4 MN, which matches with the applied tension of 2.42 MN in the F\_input.

### Comparison of ARM and OpenFAST for load case 7

For this load case I have compared the mooring line 1 nodal position and line tension. Since the fluid dampening does not affect the result, I have proceeded with only the simulations with normal coefficient of fluid dampening. The line distribution for both ARM simulations are close to the OpenFAST results, but for the original discretization I observed that the line distribution starts to differ at around node 181, which is also where I observed instability with  $n_{stress}$  with this polynomial degree, see figure 4.6a. For the simulation with increased polynomial degree and continuity order the instability of  $n_{stress}$  is shifted towards the touchdown point, and the instability is decreased compared to the original polynomial degree.

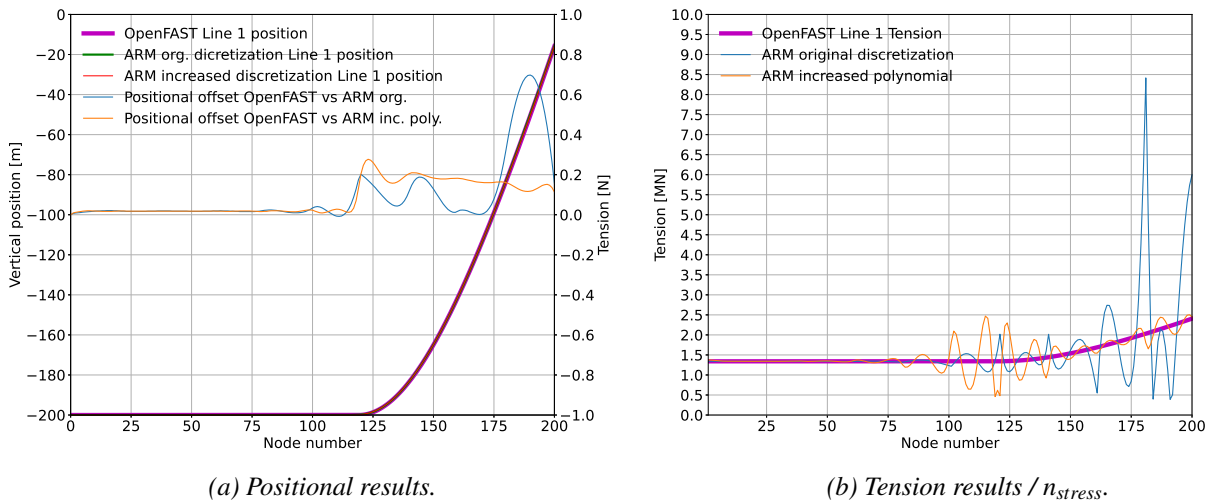


Figure 4.6: Comparison of OpenFAST results versus ARM with org. discretization and increased polynomial degree.

From figure 4.6a it can be observed that the offset distance from OpenFAST is reduced with the new FEM discretization.

Fairlead 1 OpenFAST [m]		Fairlead 1 ARM org. [m]		Fairlead 1 ARM inc. pol. [m]	
Node200px	-57.225	Node200px	-57.566	Node200px	-57.510
Node200py	0.000	Node200py	-0.000	Node200py	-0.000
Node200pz	-15.827	Node200pz	-15.670	Node200pz	-15.713
Offset from OpenFAST			0.375		0.307

Table 4.7: Dynamic relaxed fairlead coordinates, comparison OpenFAST and ARM.

The  $n_{stress}$  from the ARM simulation with increased polynomial degree shows a better comparison with OpenFAST simulated tension, see figure 4.6b, but there is still some instability, which has shifted to around the touchdown point. I believe that the instability could be caused by a numerical artifact, or from shear locking in the FEM analysis, this is discussed further in the conclusion, see chapter 5.

I do see the unstable  $n_{stress}$  as a challenge for the new model, which needs to be addressed if this model is to be used for mooring line tension analysis.

### 4.3.2 Load case 8 - Step-wind

The step-wind case is run as a simulation without waves, while the wind speed is stepped up in 200s intervals from 3 m/s until 25 m/s and back down to 3 m/s. In this case the wind is uniform.

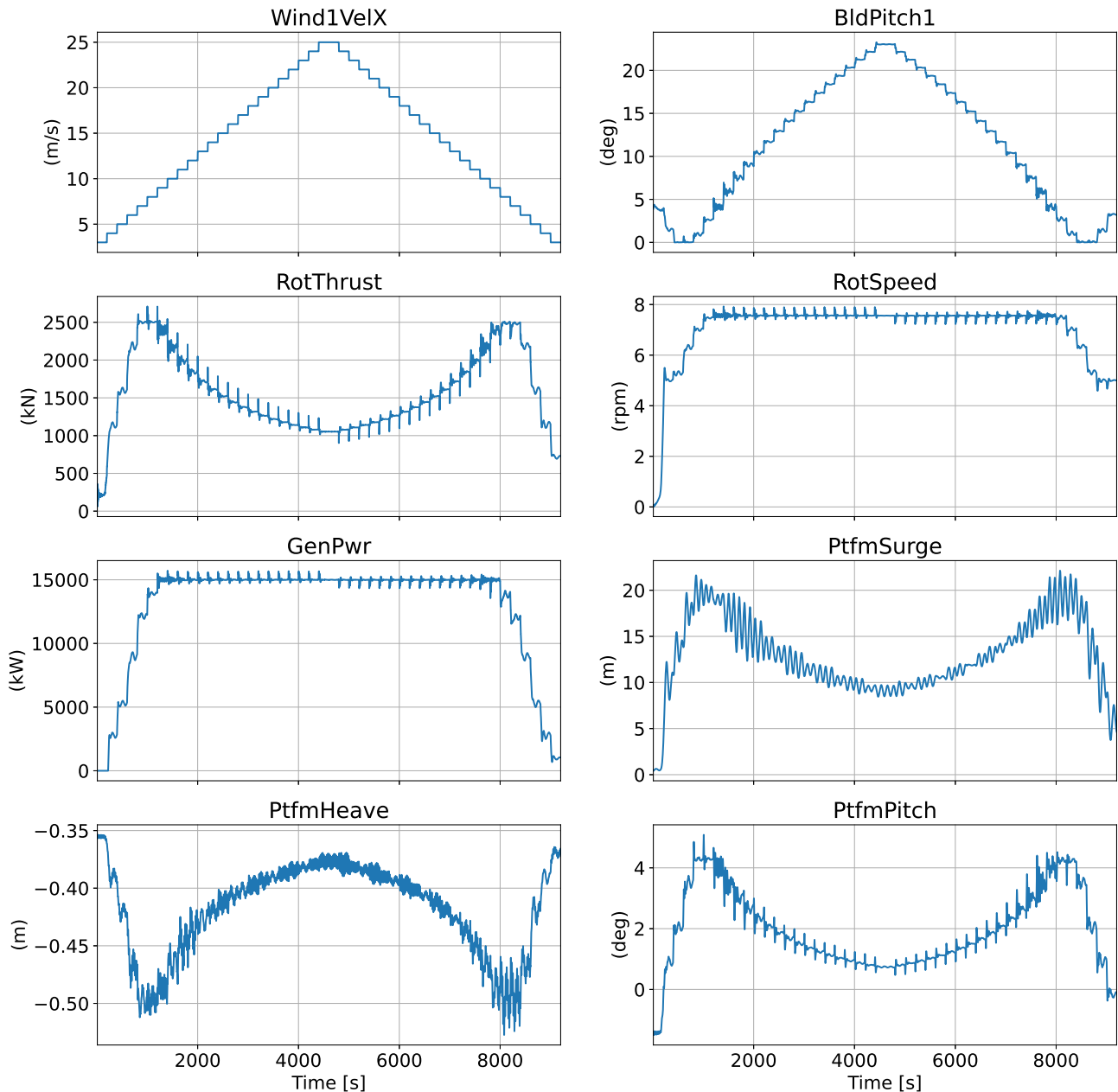


Figure 4.7: Step-wind platform motion and turbine response from OpenFAST simulation of load case 8.

As can be seen from figure 4.7, maximum thrust force is achieved just before rated wind speed, which causes the platform to surge and pitch at its maximum. This also causes a negative heave motion. The controller seems to work good, from rated wind speed to max wind speed the generated power is kept at 15 MW, and the blade pitch keeps the rotational speed at its maximum rotor speed from table 2.2. There is no indications of the controller introducing negative damping, and there is no platform pitch instability.

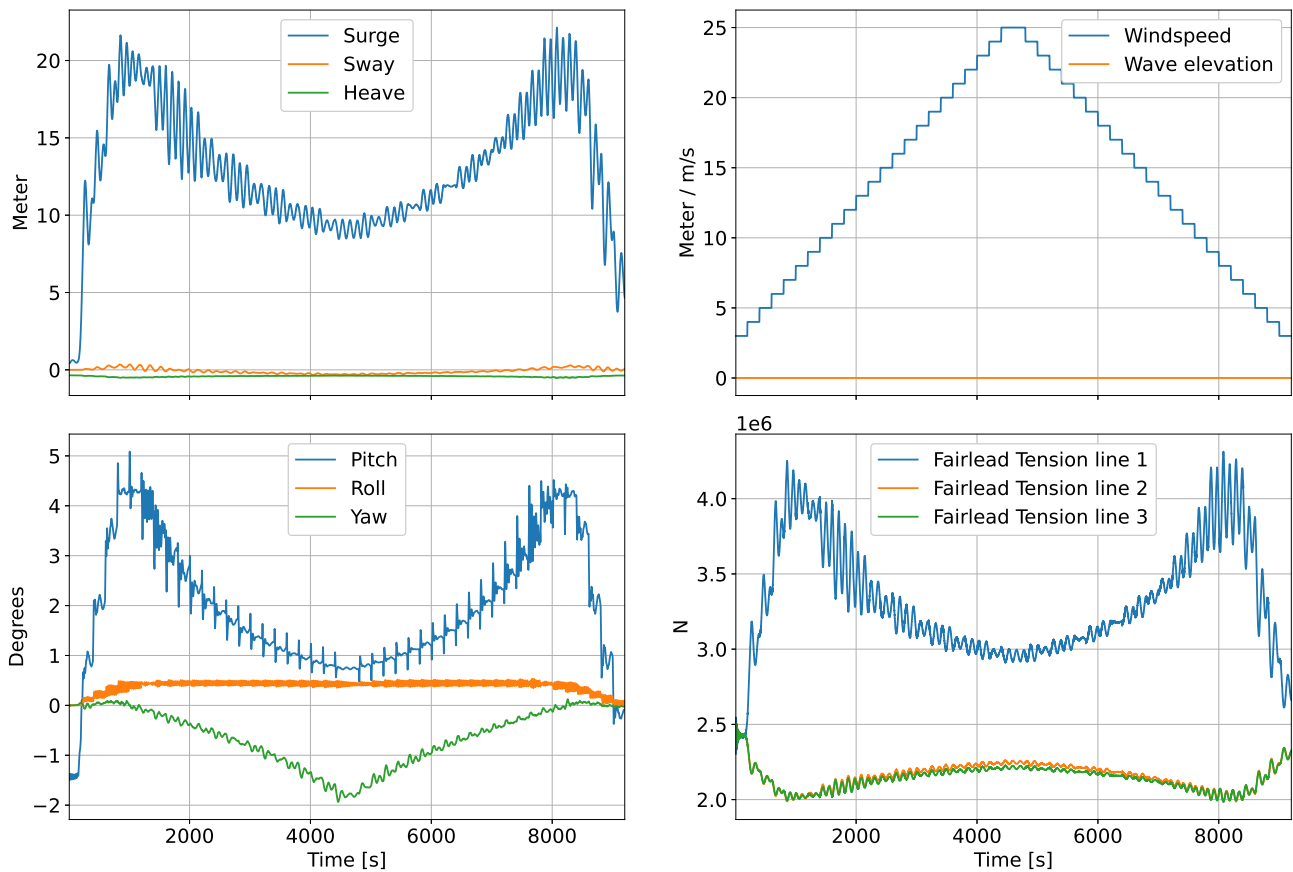


Figure 4.8: Platform motion with step-wind only.

As seen in figure 4.8, the tension in line 2 is slightly higher than for line 3. This is due to the yaw motion the platform experiences as the wind speed is stepped up. Maximum yaw experienced at maximum wind speed. This is also obvious when looking at the nodal motion, and comparing line 2 and 3, the vertical position of nodes 140 and 200 are both deeper for line 3 than line 2.

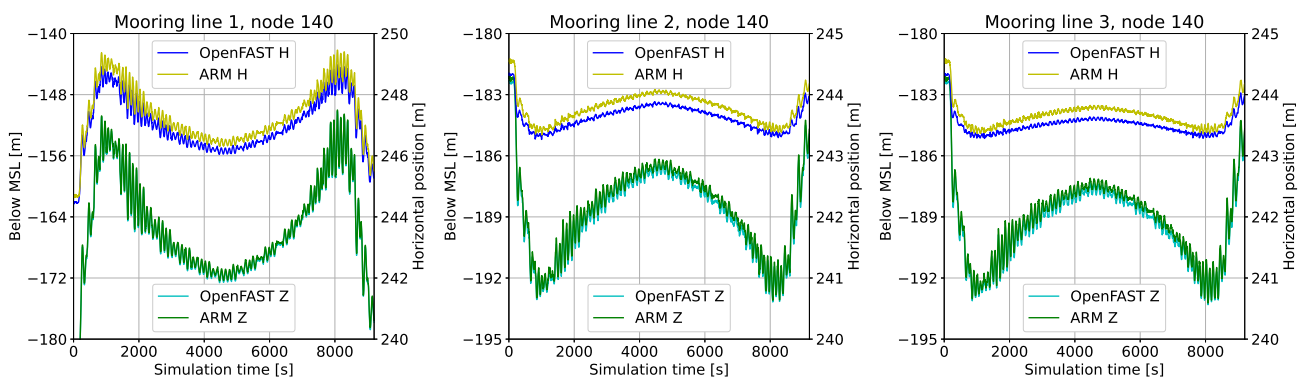


Figure 4.9: Nodal comparison for load case 8, node 140 position over time.

Figure 4.9 shows the motion of node 140 for all three mooring lines. Both the OpenFAST and ARM simulation shows similar response of the horizontal and vertical position. All three lines show a slight offset in the horizontal position of the selected node, which I believe is due to the stiffness of the model, where the MoorDyn model is slightly stiffer than ARM. The difference in model stiffness comes from the nature of a lumped parameter model vs. a continuous model, this is discussed further in the conclusion, see chapter 5. If the number of

nodes in the lumped parameter model had been increased towards infinite I would expect the two models to converge.

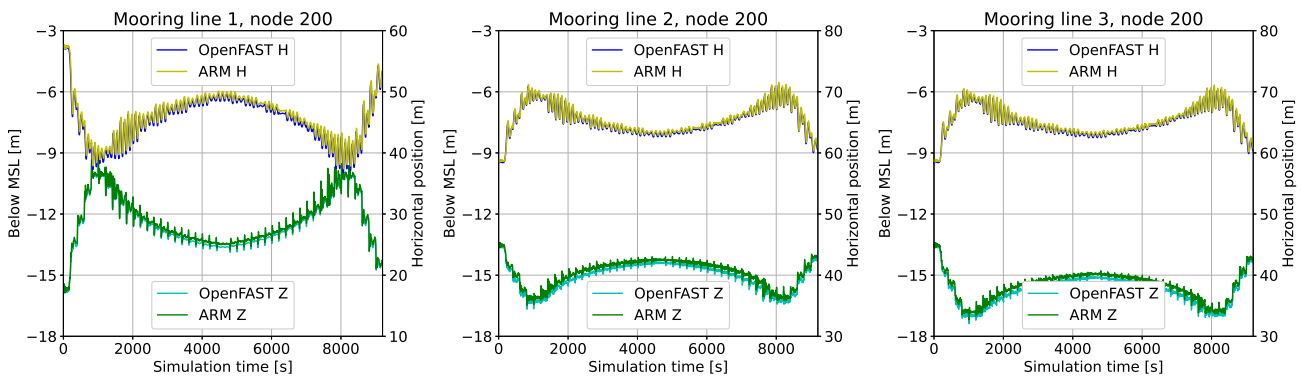


Figure 4.10: Nodal comparison for load case 8, fairlead position over time.

Figure 4.10 shows the motion of node 200, the fairlead, for all three mooring lines. The fairlead position for both models and all three mooring lines are showing a high degree of comparability. The horizontal offset seen for node 140 is not visible for the fairlead. I believe both simulations show a similar pattern of motion for both node 140 and the fairlead. Both the vertical and the horizontal position is within an acceptable offset. Node 140 shows a slightly larger offset on the horizontal position.

### 4.3.3 Load case 9 - rated wind speed without waves

This load case is simulated in OpenFAST using a turbulent wind field as described previously. The OpenFAST simulation time is 5400 seconds, For analysing the OpenFAST results, I discard the first 3000 seconds. The ARM simulation is run for 3600 seconds where the first 600 seconds are with the constant dynamically relaxed fairlead force to let the mooring line relax to near static position, before the next 3000 seconds are with the load case dynamic fairlead force. I remove the first 1200 seconds of the result, and end up with 2400 seconds of comparable data.

At rated wind speed, the thrust force is at its maximum. I expect to see a shift in the surge position, similar to load case 8, step-wind. Due to the surge offset, I expect mooring line 1 to be lifted off seafloor, which in return will create a strong restoring force. As already mentioned, the wind field was generated using TurbSim2.00. To verify that the wind field had the expected conditions, I have performed a quick analysis on this. This showed a mean wind speed at 11.0 m/s, with a standard deviation of 1.9 m/s. This gives a turbulence intensity of 17.2. The skewness and kurtosis is 0.16 and 3.03 respectively, meaning that the distributed wind speed follows the normal, Gaussian, distribution. All wind measurements are at hub height, and is calculated over the analysed time interval.



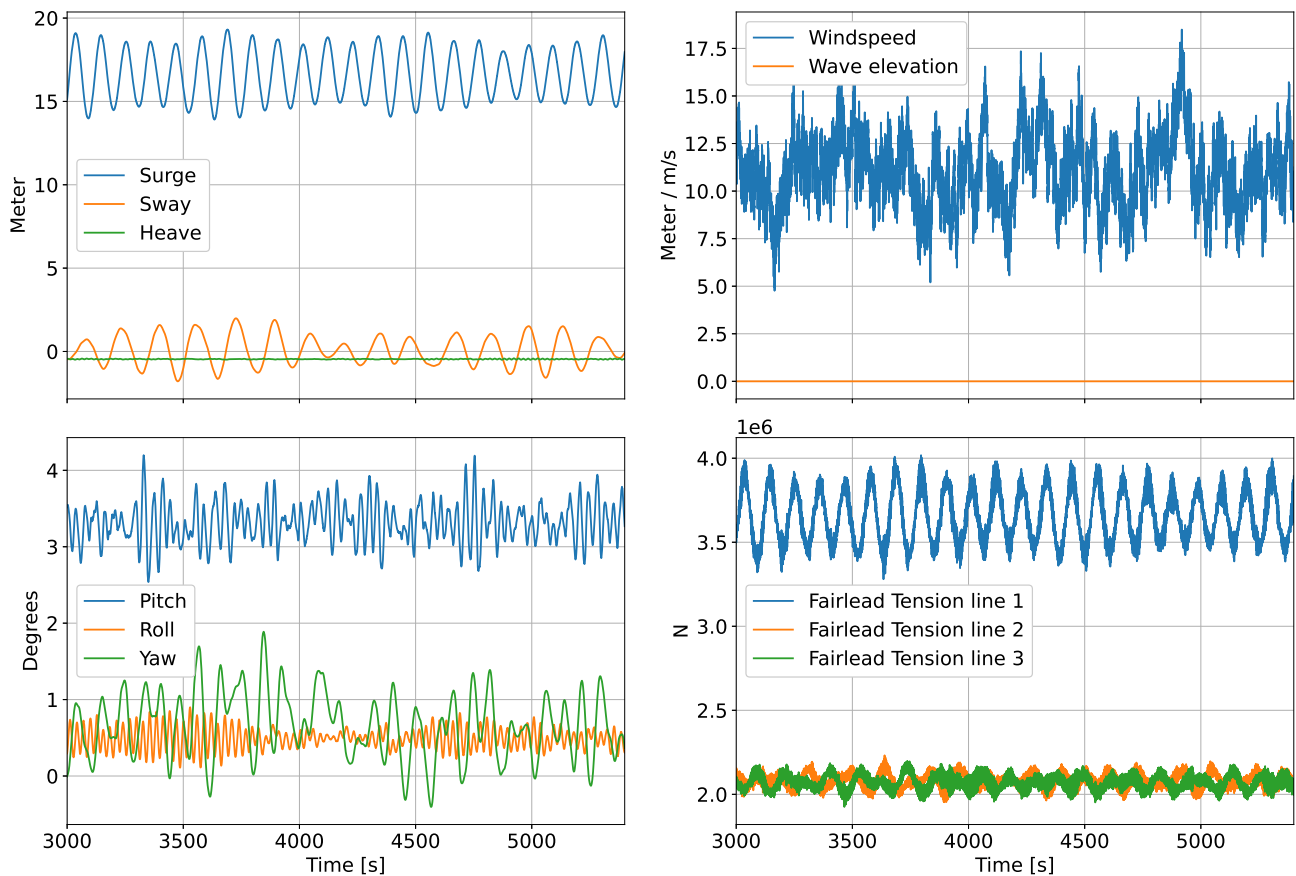


Figure 4.11: Platform motion with wind only.

As can be observed from figure 4.11, the platform surges at an average of 17m from origin, and the pitch shifts from the static  $-1.4^\circ$  to an average of  $3.4^\circ$ . The tension at fairlead 1 is almost double compared to fairlead 2 and 3. Also, the variation of fairlead 1 tension is much greater, and seems to follow the cyclic surge motion.

### Mooring line analysis

When looking at the line displacement for the mooring analysis, one important factor is to find at what point the line is lifted from the seafloor. It is important that there is sufficient resting line to avoid vertical forcing at the anchor. As mentioned in section 2.5, most anchors cannot take up vertical forces.

	OpenFAST		ARM	
	1 <sup>st</sup> node lifted	Distance to anchor [m]	1 <sup>st</sup> node lifted	Distance to anchor [m]
Line 1	91	386.9	90	382.5
Line 2	126	535.6	125	531.2
Line 3	126	535.6	125	531.2

Table 4.8: Nodal lift off from seafloor.

As can be seen from table 4.8, the ARM results have more movement in the line, such that the 1<sup>st</sup> node that is lifted from seafloor is closer to the anchor than for the OpenFAST results. But it is also worth noting that both simulations show a resting line length of more than 380m. This would be more than normally required, and could potentially be shortened to reduce material cost of mooring lines. This would need to be investigated further with more load cases before a final decision can be made.

For positional comparison between the two models, I decided to plot the mean line position for the scenario, and show the variation from mean line position. All three mooring lines are shown in the figures.

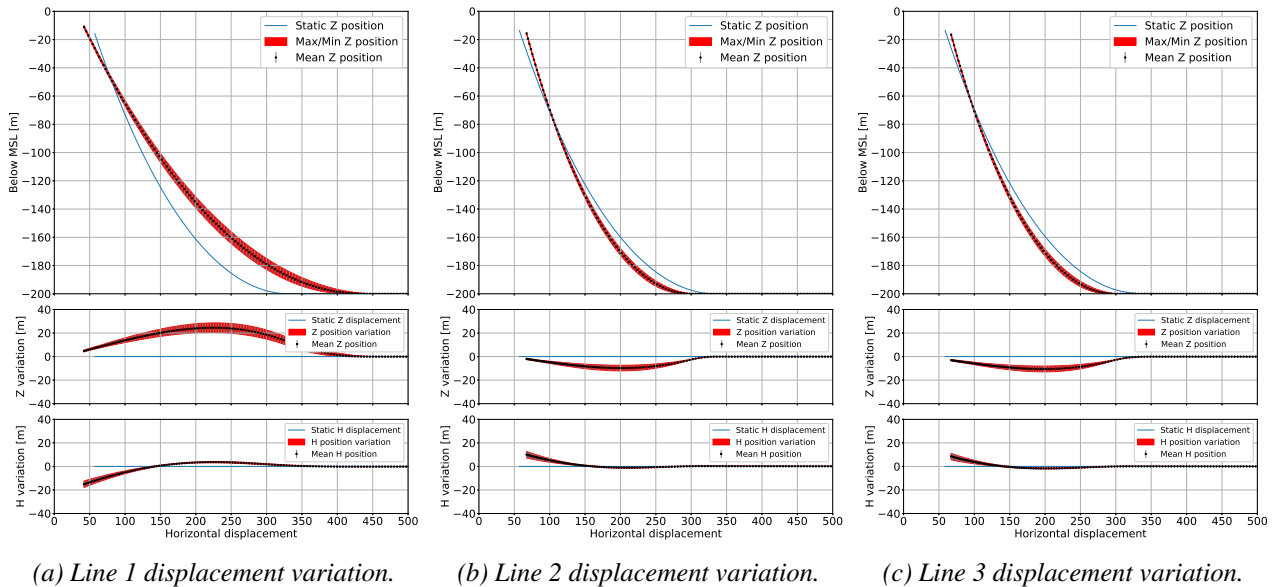


Figure 4.12: MoorDyn mooring line distribution from load case 9.

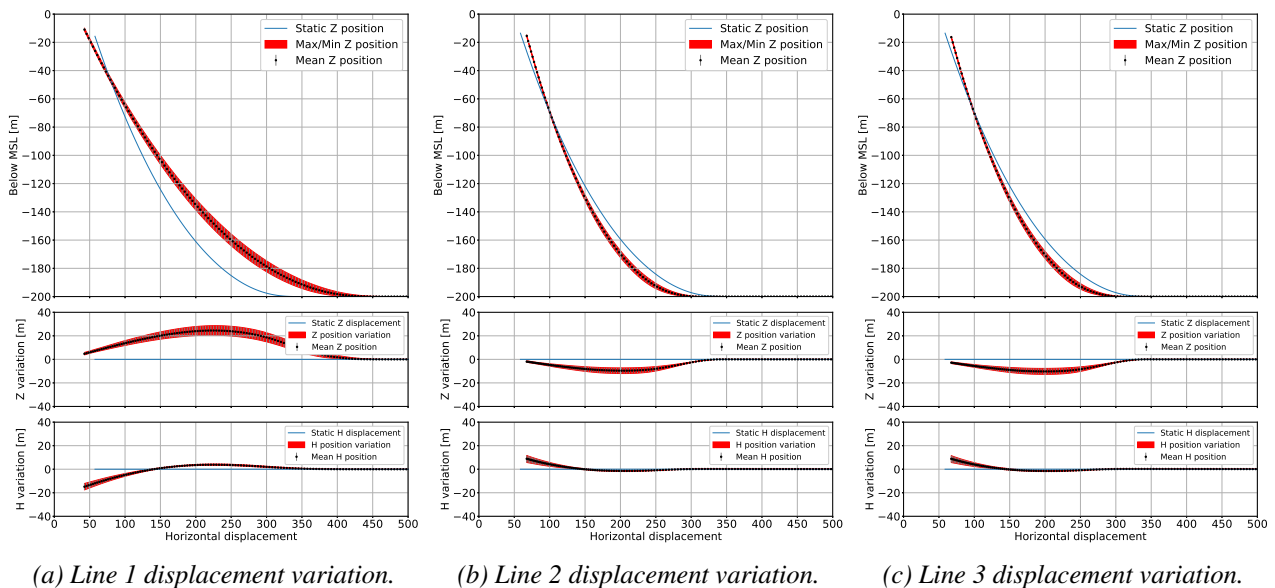


Figure 4.13: ARM mooring line distribution from load case 9.

The comparison between OpenFAST and ARM line distribution for this load case is very good, and minimal offset can be observed from the figures 4.12 and 4.13. Both simulations show that line 1 is stretched out and lifted from the sea bottom, while line 2 and 3 see a reduction in tension and hence more of the line is resting on the sea bottom. As expected when the wind is coming from  $0^\circ$ irc, line 1 has the highest tension and line 2 and 3 shows almost identical results. The positional data for line 2 and 3 are close to identical, which is what would be expected since the wind inflow angle is from  $0^\circ$ .

For the nodal comparison of the positional data I chose node number 150. This is one of the nodes that experiences the largest positional variance for all lines and load cases, and thus is well suited for comparison. I also compared the fairlead position for all 3 lines.

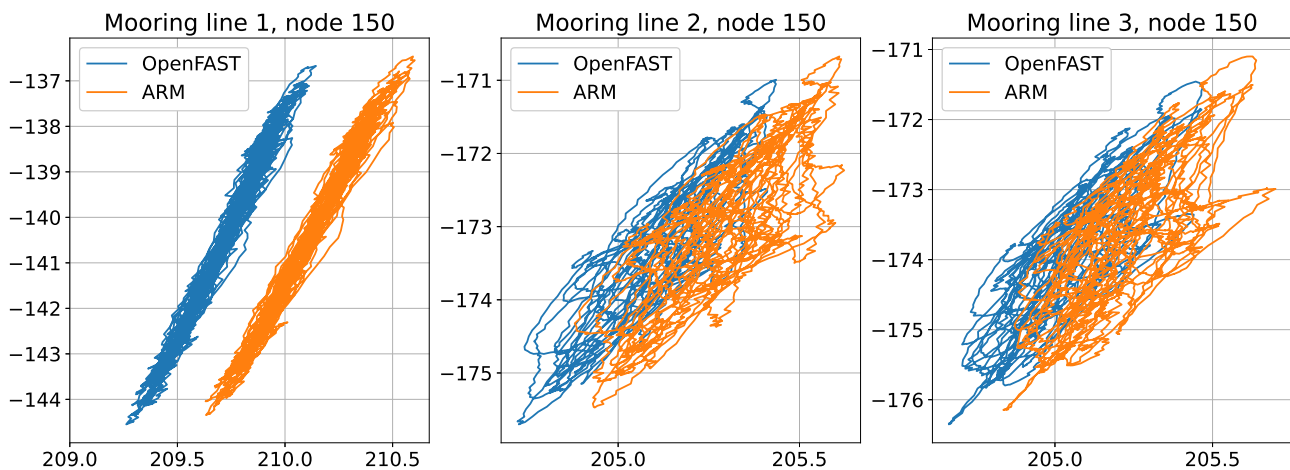


Figure 4.14: Nodal comparison for load case 9, node number 150.

The nodal motion of node 150 for mooring line 1 shows a near linear motion, but a slight horizontal offset between ARM and OpenFAST. For line 2 and 3 the nodal movement of both simulations show a similar layout, and minimal offset, see figure 4.14. I believe the offset is due to the model stiffness, which is discussed more in the conclusion.

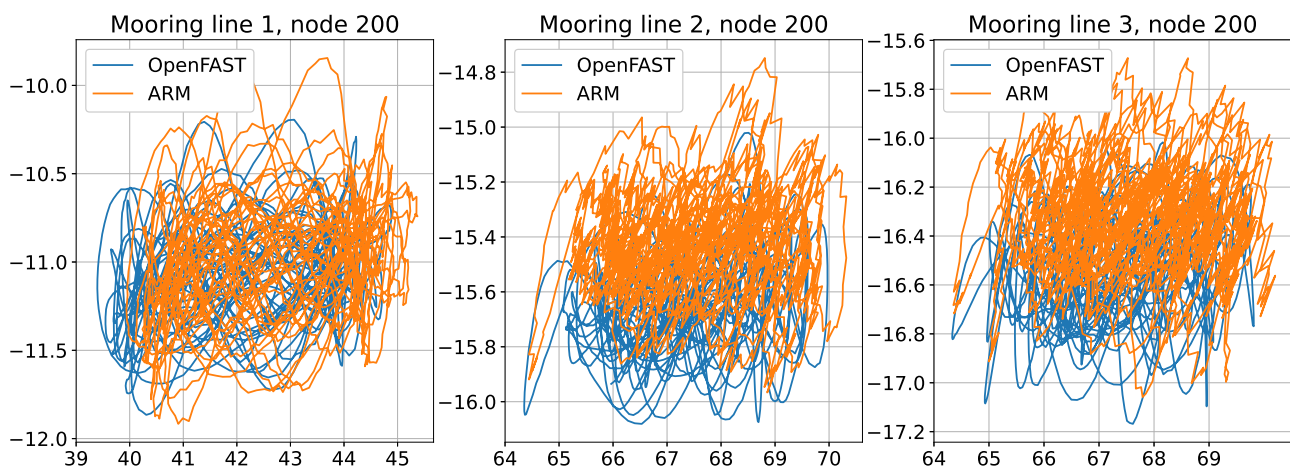


Figure 4.15: Nodal comparison for load case 9, fairlead.

Also for the fairlead motion shown in figure 4.15, both simulations show a similar nodal motion pattern, and the motion is within the same area. I believe the motion results from the nodes displayed in figure 4.14 and 4.15 shows that the ARM simulator agrees with MoorDyn for the nodal positional data.

### Line tension comparison

To analyse the line tension for a dynamic scenario, I decided to display the mean tension and the variation in tension for each segment.

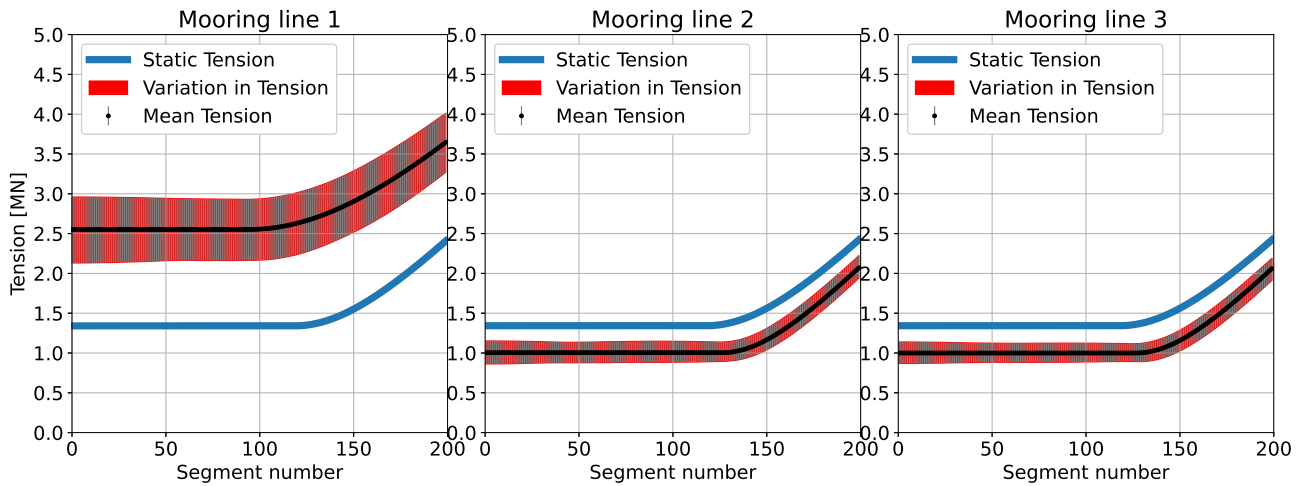


Figure 4.16: OpenFAST line tension variation, lines 1 through 3.

In figure 4.16 I have compared how the tension in the lines are shifted from the dynamically relaxed static tension to the mean tension for this load case. Line 1 is experiencing an increase in tension at the fairlead of 1.2 MN from the static, while line 2 and 3 are experiencing a reduction in tension of 0.3 MN. The variation in tension for line 1 is in the order of 0.8 MN for line 1 and 0.3 MN for line 2 and 3.

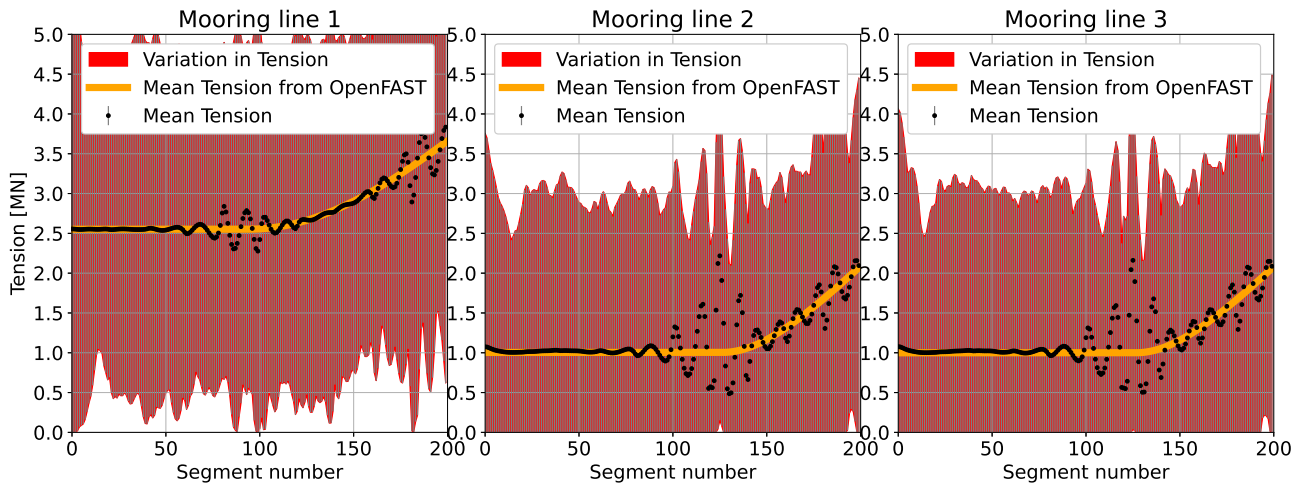


Figure 4.17: ARM line tension variation, lines 1 through 3.

For the tension results, this is where the ARM has the biggest challenge. The mean  $n_{stress}$  is similar to the mean tension from OpenFAST results, but max/min variation is much greater for ARM results than OpenFAST, for line 1 the variation is in the order of 5 MN, while for line 2 and 3 it is around 3 MN.

I had a hypothesis that the reason for the highly erratic tension could be due to the time-steps being too long, and that the force at the fairlead would change too rapidly for the ARM simulator, which could introduce instability in the tension calculation. In the ARM simulation the time-stepping is 0.1 second, or 10 Hz simulation frequency. I decided to reduce the time-step for the ARM simulation from 0.1 second to 0.01 second, or 100 Hz simulation frequency. The figure 4.18 shows the results from the ARM simulation run at 100 Hz frequency.

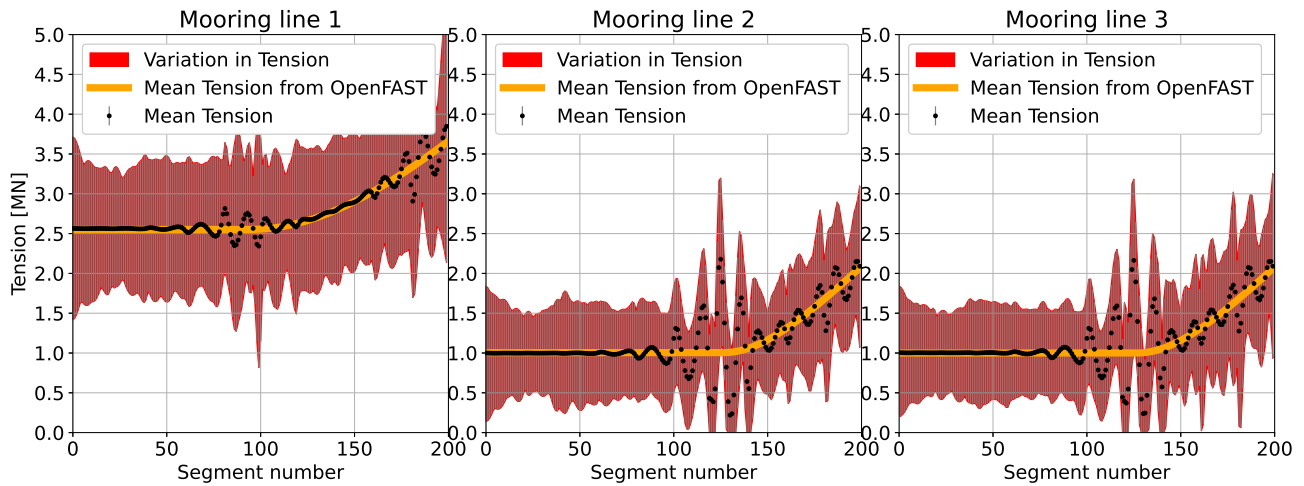
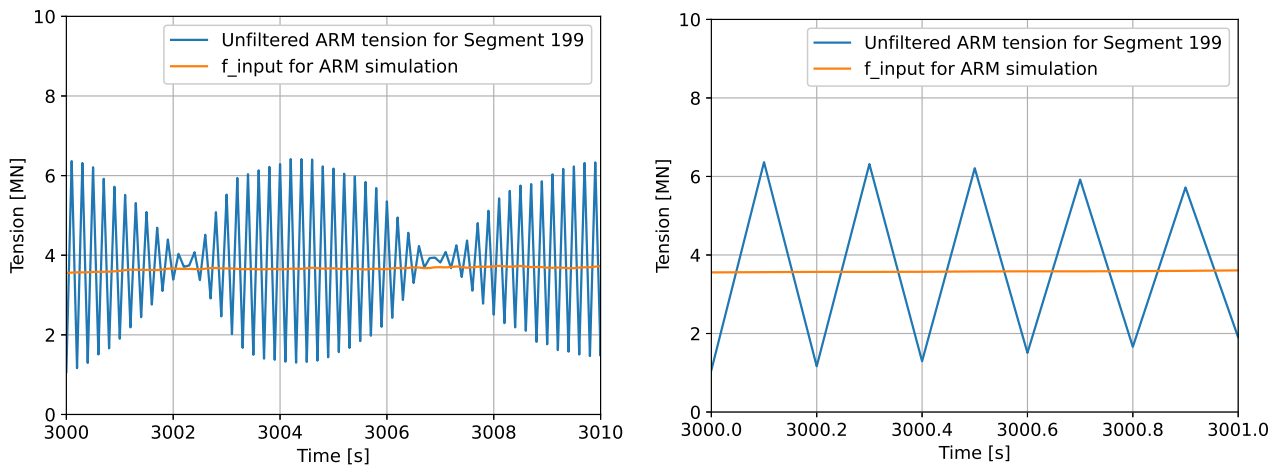


Figure 4.18: ARM line tension variation, increased frequency, lines 1 through 3.

The results from the simulation at 100 Hz shows much better comparison with OpenFAST, but still a slightly larger variation, in the order of 1.5 MN for line 1 and around 1 MN for line 2 and 3. I believe the smaller changes in input force due to the shorter time between force input at the free end is reducing the erratic behaviour of the tension results. Due to the high computational time for the 100 Hz simulations, I wanted to investigate if the 10 Hz results could be refined. When going back to the 10 Hz simulation results, and zooming in on the time interval, I noticed that the data shows a noise band of 10 Hz on top of the tension data, see figure 4.19. This 10 Hz noise, which is the same as the time-step used for the simulation, can easily be filtered out.



(a) Zoomed raw data for segment 199.

(b) Zoomed raw data for segment 199.

Figure 4.19: Figure showing noise on tension data from ARM.

I applied a low pass filtering of the 10 Hz results, using a Butterworth low-pass filtering technique. I set the cut-off to 1 Hz. The below graphs show the filtering of segment 160 for line 1.

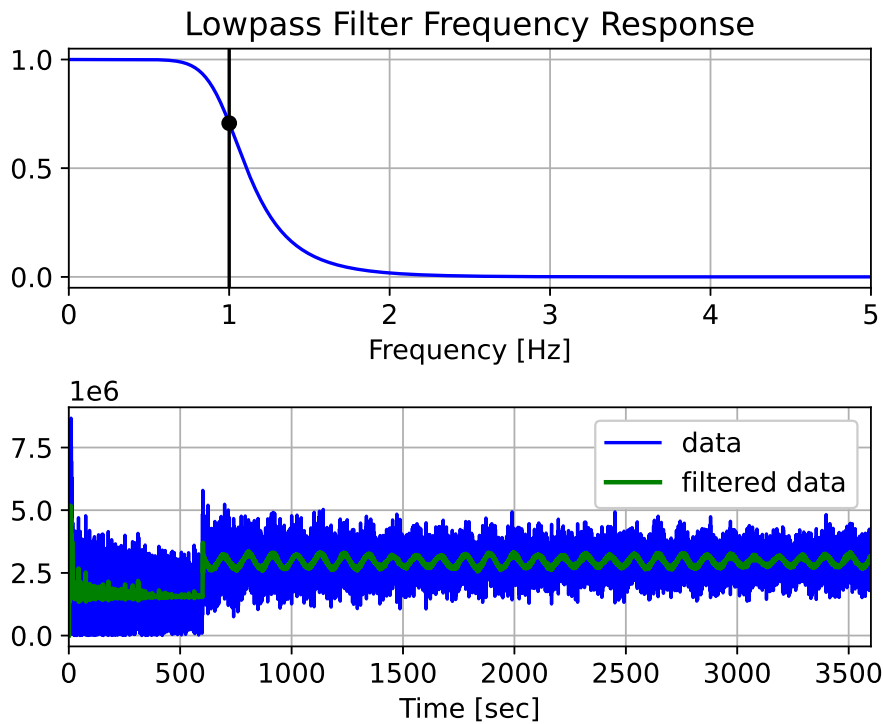
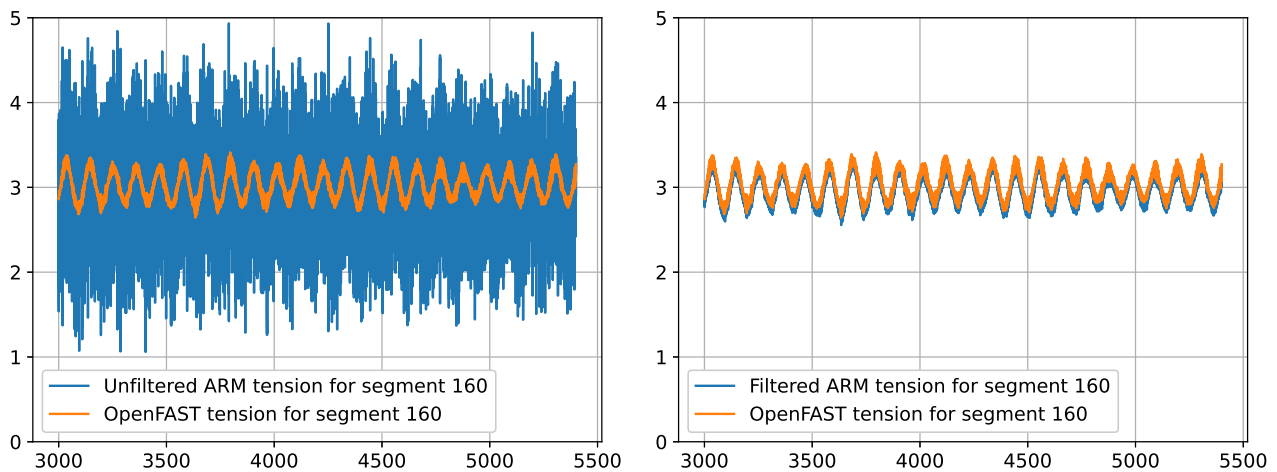


Figure 4.20: Low pass filtering, cutoff at 1 Hz.

From figure 4.20, it can be observed that the first 600 seconds is the dynamic relaxation of the line, where the input force is static. For analysis, I remove the first 1200 seconds of the time-series to allow for dynamic relaxation, and remove any biasing error once the varying free end force is applied. Figure 4.21 shows the before and after filtering of tension at node 160 compared with OpenFAST. For this node, the filtering has a very good effect, and the results are matching well with OpenFAST.



(a) ARM unfiltered tension at segment 160, mooring line 1. (b) ARM filtered tension at segment 160, mooring line 1.

Figure 4.21: The results from the Butterworth filtering.

The tension results were much improved, and the post-filtered mean, max and min tension results can be observed in figure 4.22. The variation in tension for line 1 is now in the same range as the OpenFAST tension results, but still slightly enlarger for line 2 and 3. It is unknown at this time if this higher variation in tension is due to numerical artifacts or actual tension results from using an advanced rod model.

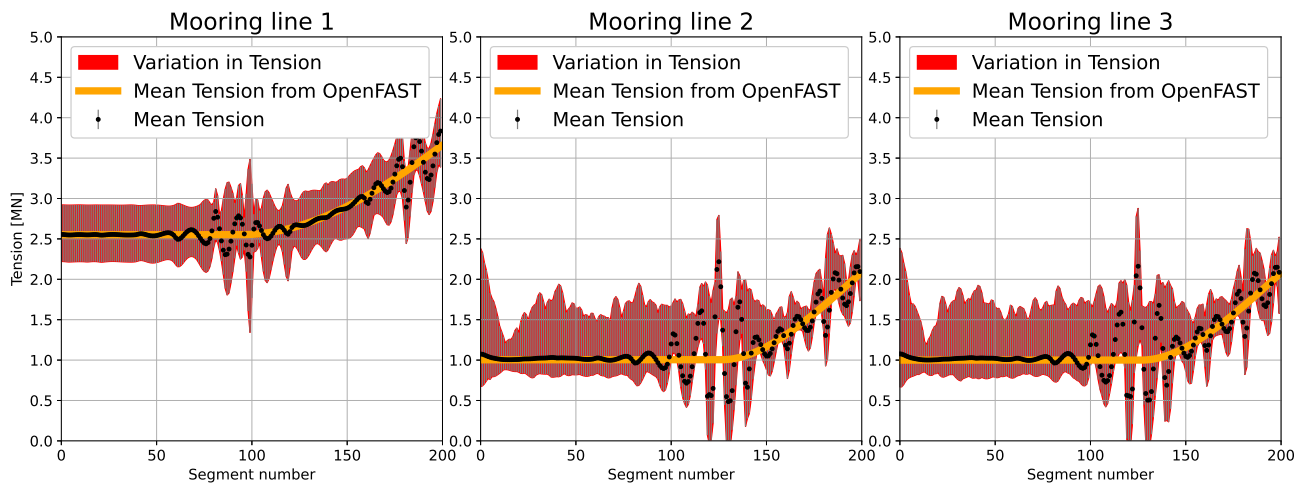


Figure 4.22: ARM line tension variation, lines 1 through 3.

For the remaining dynamic simulations, a 10 Hz simulation frequency is used, and the  $n_{stress}$  is filtered using a Butterworth low pass filter with cutoff at 1 Hz.

### 4.3.4 Load case 10 - rated wind speed with waves

This load case uses the same wind field as load case 9, but introduces waves with  $H_s$  of 1.6m and a periode of 7.6 seconds. This is the NSS, normal sea state, for rated wind speed at this site.

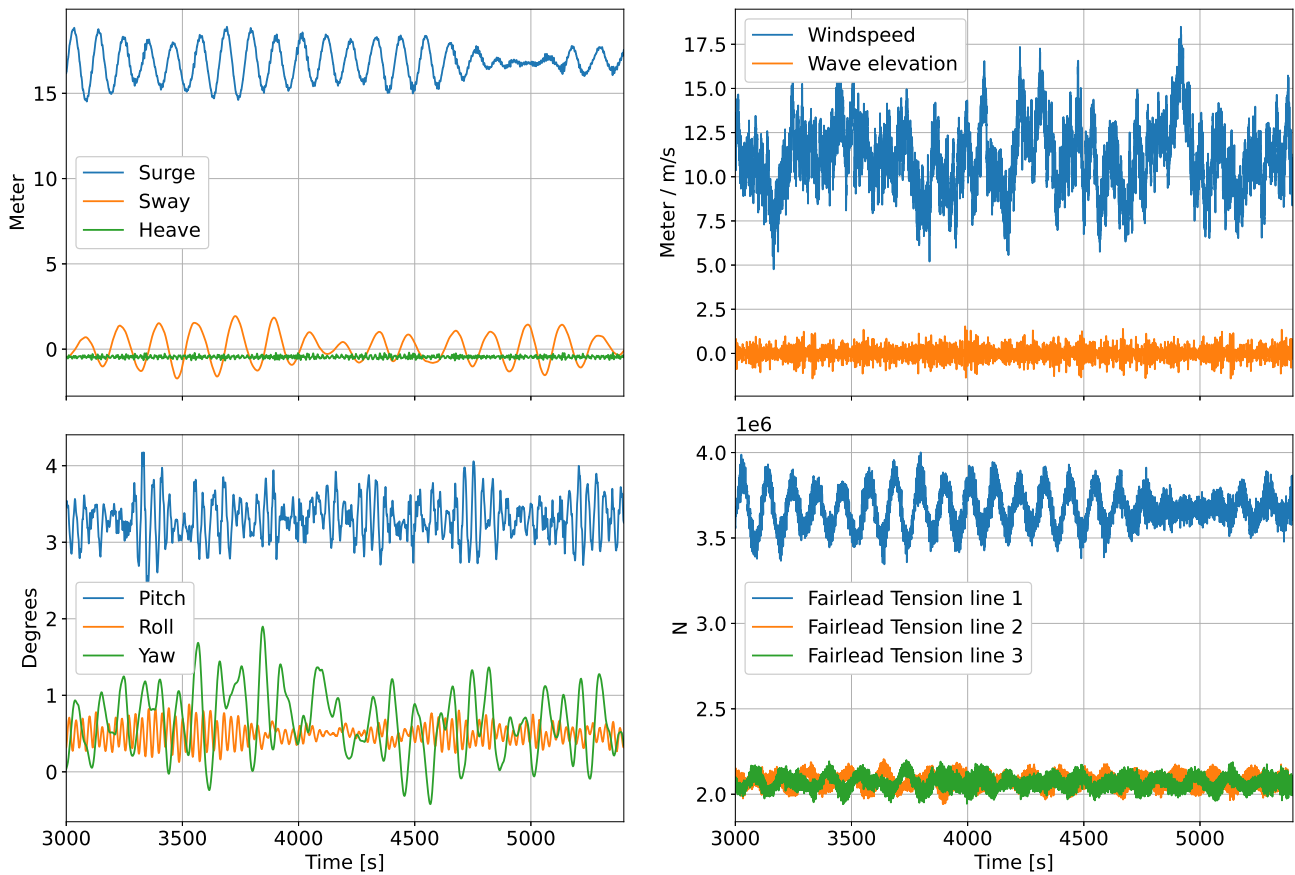


Figure 4.23: Platform motion with wind and waves.

I expected similar platform motion as load case 9, but a slight increase in surge and heave motion due to the introduction of the waves. This will in turn give a slight increase in fairlead 1 tension, and a slight reduction in fairlead 2 and 3 tension. Instead the fairlead 1 tension reduced compared to load case 9.

#### Mooring line analysis

As before, I proceed with finding the mooring lines touchdown point.

	OpenFAST		ARM	
	1 <sup>st</sup> node lifted	Distance to anchor [m]	1 <sup>st</sup> node lifted	Distance to anchor [m]
Line 1	92	391.2	91	386.78
Line 2	126	535.6	125	531.2
Line 3	126	535.6	125	531.2

Table 4.9: Nodal lift off from seafloor.

As can be seen from table 4.9, the ARM results have more movement in the line, such that the 1<sup>st</sup> node that is lifted from seafloor is closer to the anchor than for the OpenFAST results. This is similar to the results from load case 9. It is worth noting that for this load



case, the touchdown point for line 1 is actually further from the anchor compared to load case 9. I find this surprising, since this load case is using the same wind field as load case 9, but also considering wave forcing, with wave direction at  $0^\circ$ , same as wind direction. For this load case I had expected more movement of the mooring line 1 due to the mean drift force from the waves.

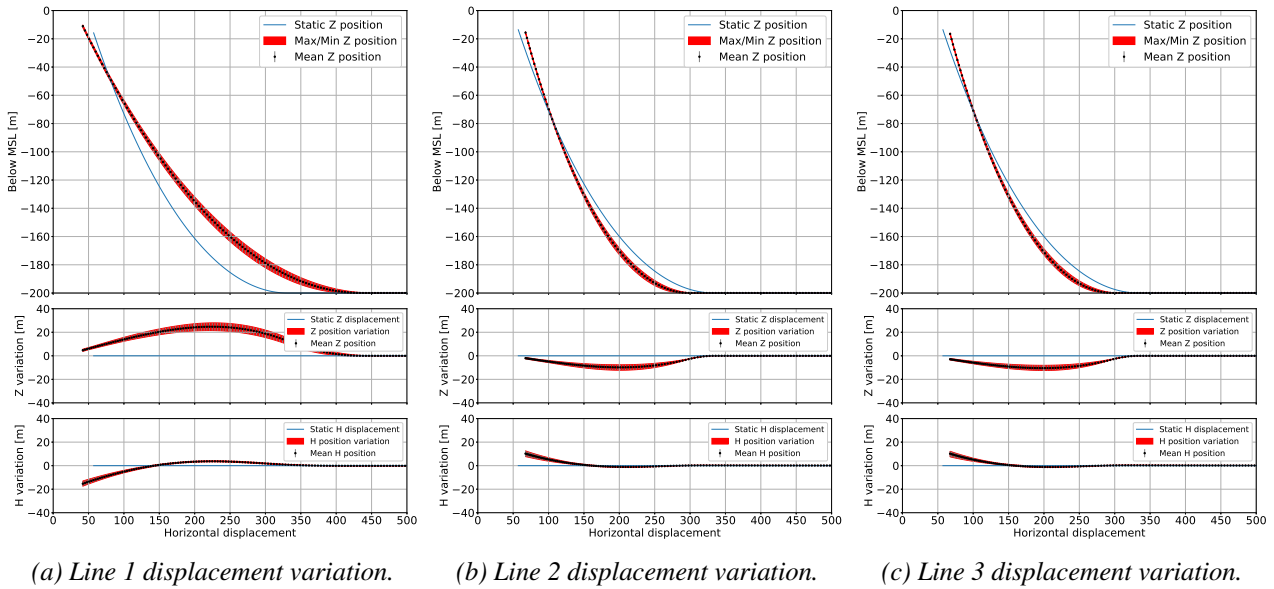


Figure 4.24: MoorDyn mooring line distribution from load case 10.

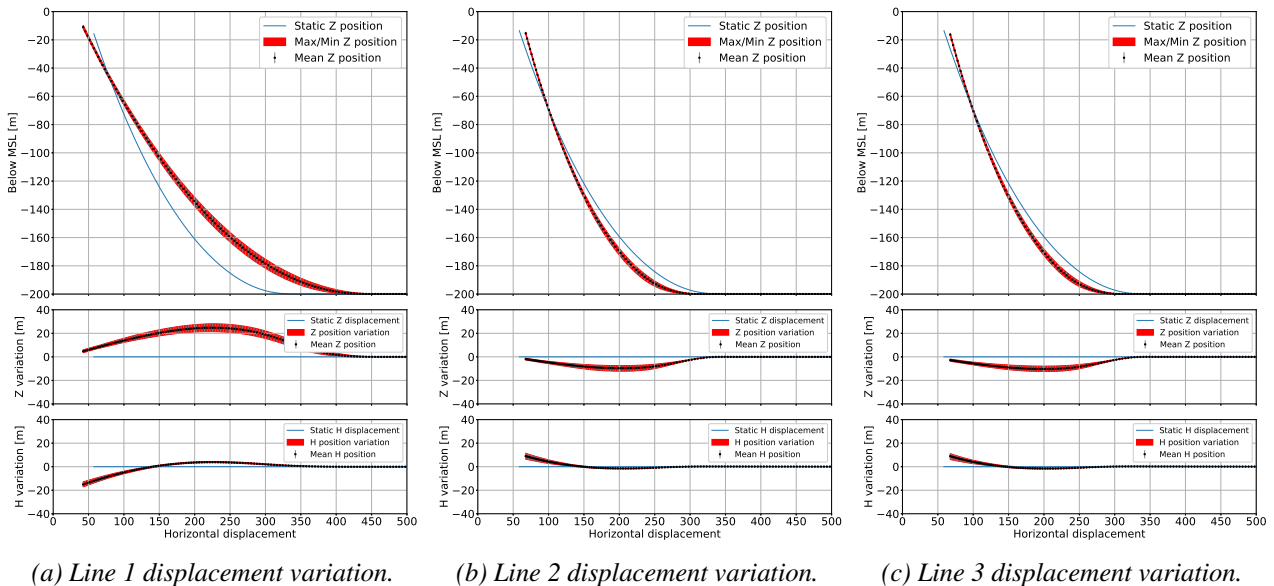


Figure 4.25: ARM mooring line distribution from load case 10.

The mooring line positional data shown in figure 4.24 and 4.25 displays a similar results as for load case 9. The line distribution from both OpenFAST and ARM simulations show a high degree of comparability.

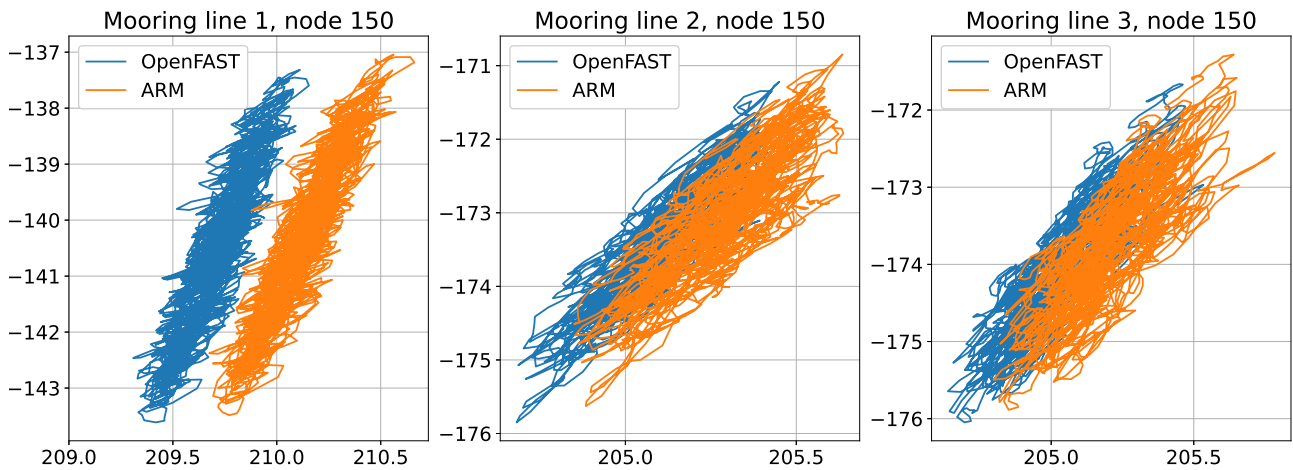


Figure 4.26: Nodal comparison for load case 10, node number 150.

The nodal position for line 1 at node 150 for this load case shows an offset between ARM and OpenFAST, mostly in the horizontal plane, as can be seen in in figure 4.26. For line 2 and 3 there is minimal offset, and the motion of the node seems to follow a similar pattern for both simulations. This is similar as for load case 9.

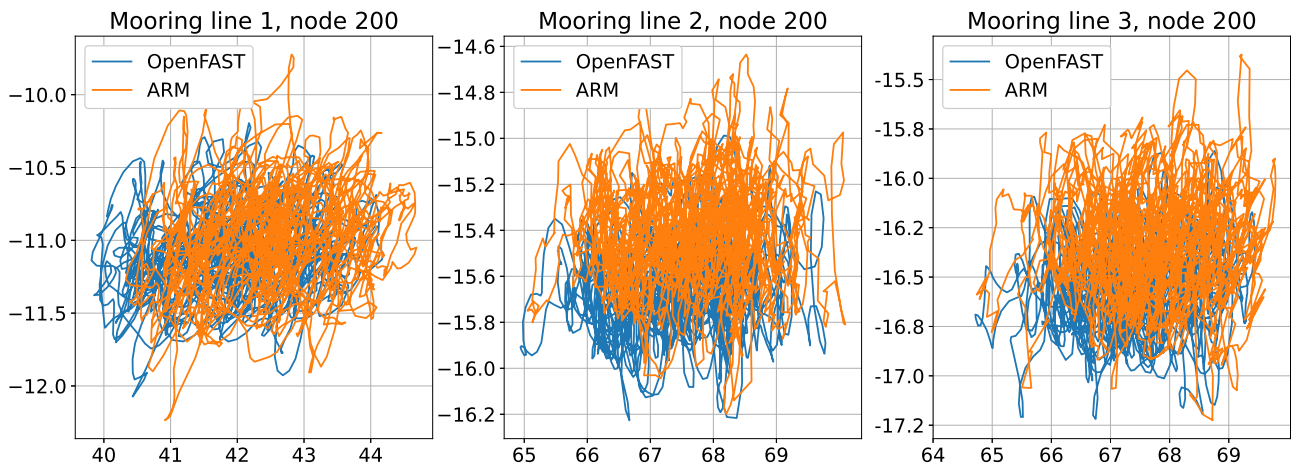


Figure 4.27: Nodal comparison for load case 10, fairlead.

For the fairlead node for all three mooring lines displayed in figure 4.27 show a very similar nodal motion. The nodal position over time stays within the same area of motion for both simulations.

## Line tension distribution

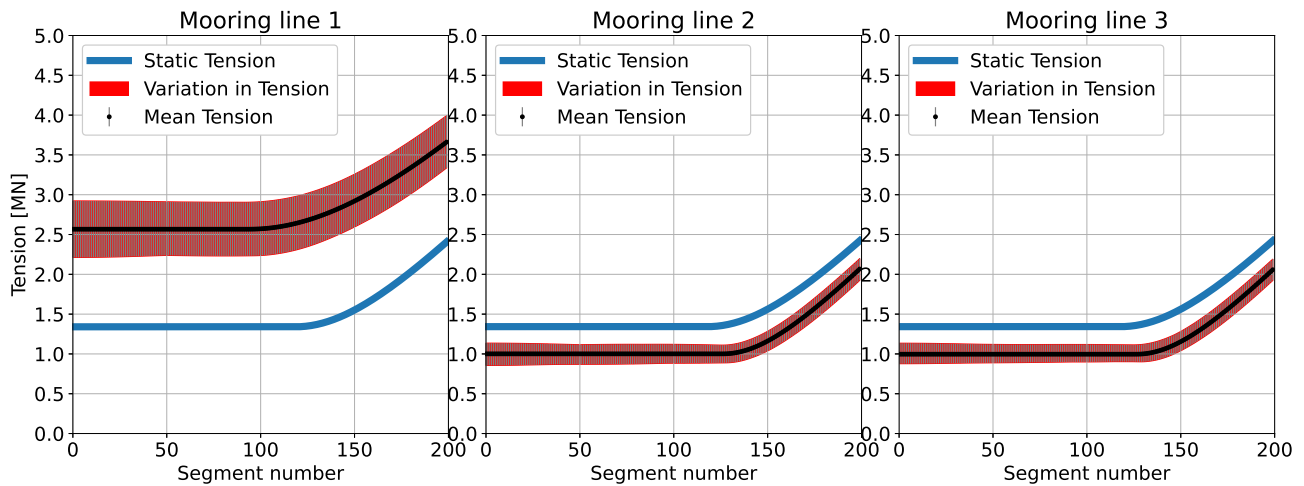


Figure 4.28: OpenFAST line tension variation, lines 1 through 3.

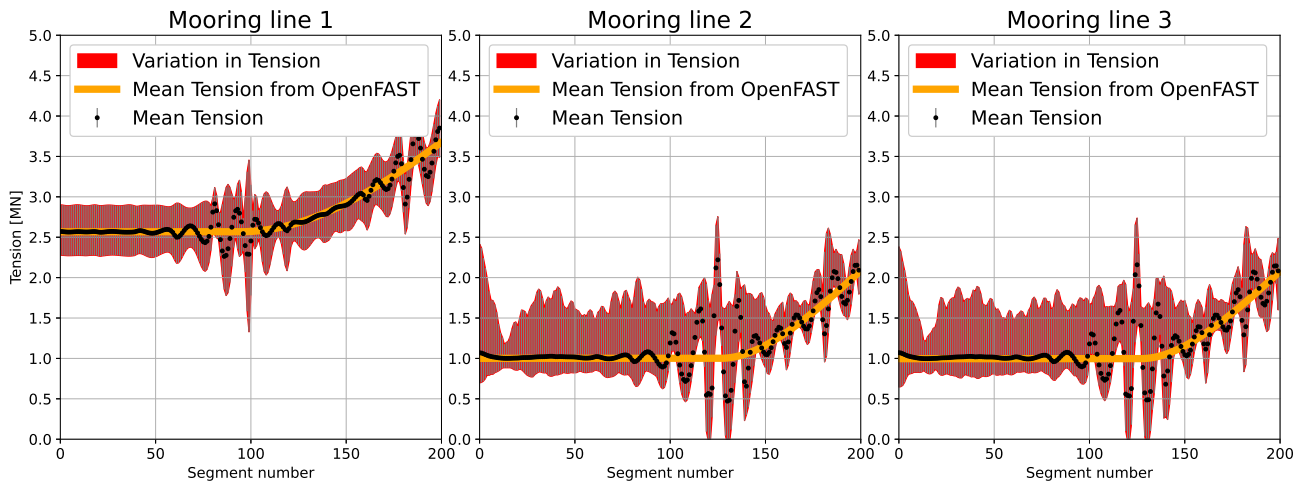


Figure 4.29: ARM line tension variation filtered, lines 1 through 3.

The tension results from both models displayed in figure 4.28 and 4.29 show a similar response as in load case 9. The variation in tension for line 1 shows good match between the OpenFAST and ARM simulation. For the resting line the max and min tension for both simulations are 2.8 and 2.3 MN respectively, and the mean tension in the line starts increasing from the touchdown point, due to the added tension from the weight of the line, as would be expected. The filtered results from ARM has more varying tension for line 2 and 3, and also more instability at the touchdown point for these lines.

### 4.3.5 Load case 11 - 50-year EWM

In this load case, the mean wind speed is 47.5 m/s. This is the EWM, turbulent 50-year model. This is above the cut-out wind speed for the turbine, which means the blades are pitched 90°, and the rotation of the rotor is stopped. In addition, waves at  $H_s$  of 10.7m and period of 14.2 seconds are introduced. This is the ESS, extreme sea state, with 50 year return period for this wind speed at this site.

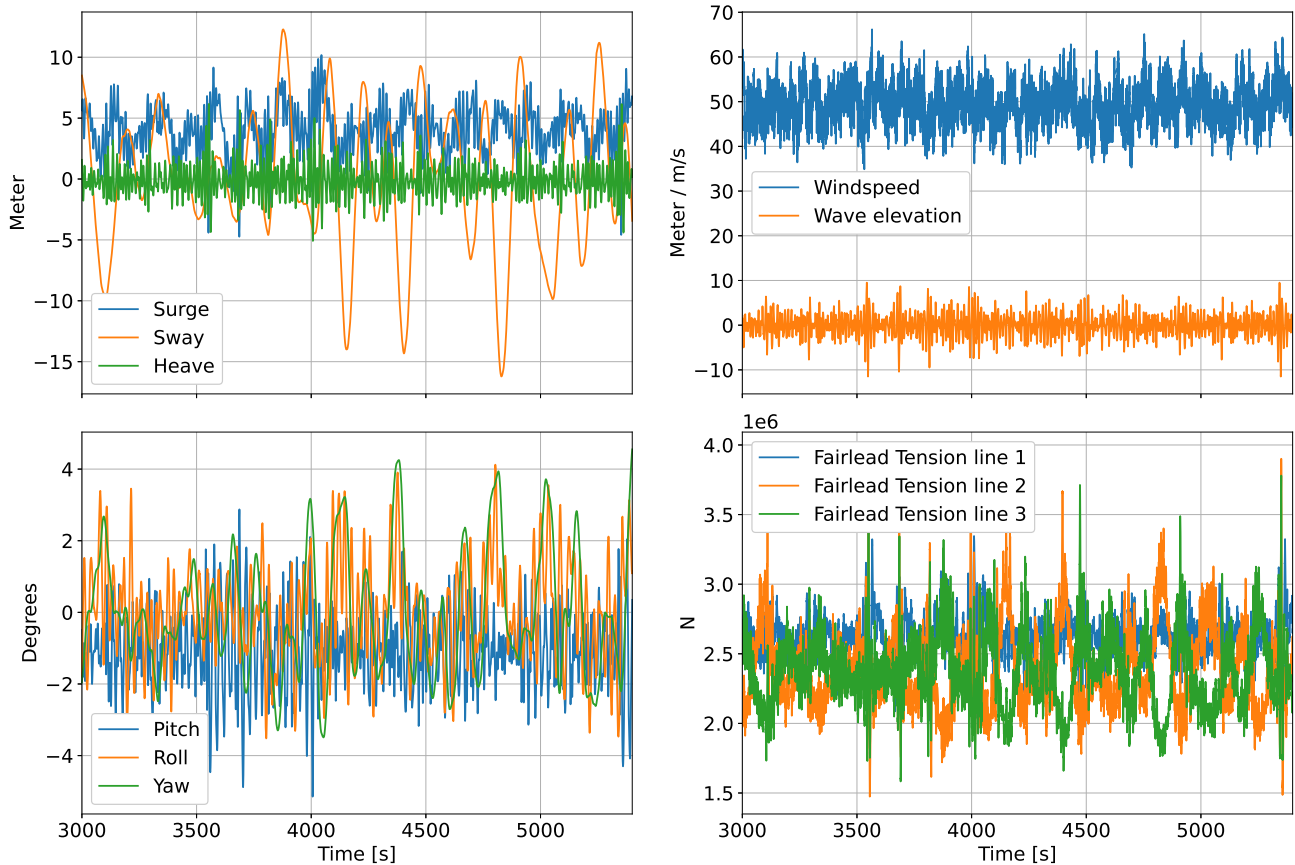


Figure 4.30: Platform motion with wind and waves, EWM 50-year model.

The platform is experiencing an average surge of 3.5m, and a large variation of sway motion. I was not expecting a sway variance of more than 25m, and I believe this is due to an interaction between the platform and the mooring lines. The FWT is swaying at its natural frequency. Due to the sway motion, fairlead 2 and 3 are experiencing the highest variation in tension.

#### Mooring line analysis

As before, I proceed with finding the mooring lines touchdown point.

	OpenFAST		ARM	
	1 <sup>st</sup> node lifted	Distance to anchor [m]	1 <sup>st</sup> node lifted	Distance to anchor [m]
Line 1	108	459.2	107	454.8
Line 2	102	433.7	101	429.3
Line 3	104	442.2	102	433.5

Table 4.10: Nodal lift off from seafloor.

As can be seen from table 4.10, ARM results have more movement in the line, such that the 1<sup>st</sup> node that is lifted from seafloor is closer to the anchor than for the OpenFAST results. It is worth noting that for this load case, the touchdown point for lines 2 and 3 are closer to the anchor than for line 1. I believe this is mainly due to the sway motion that the FWT experiences.

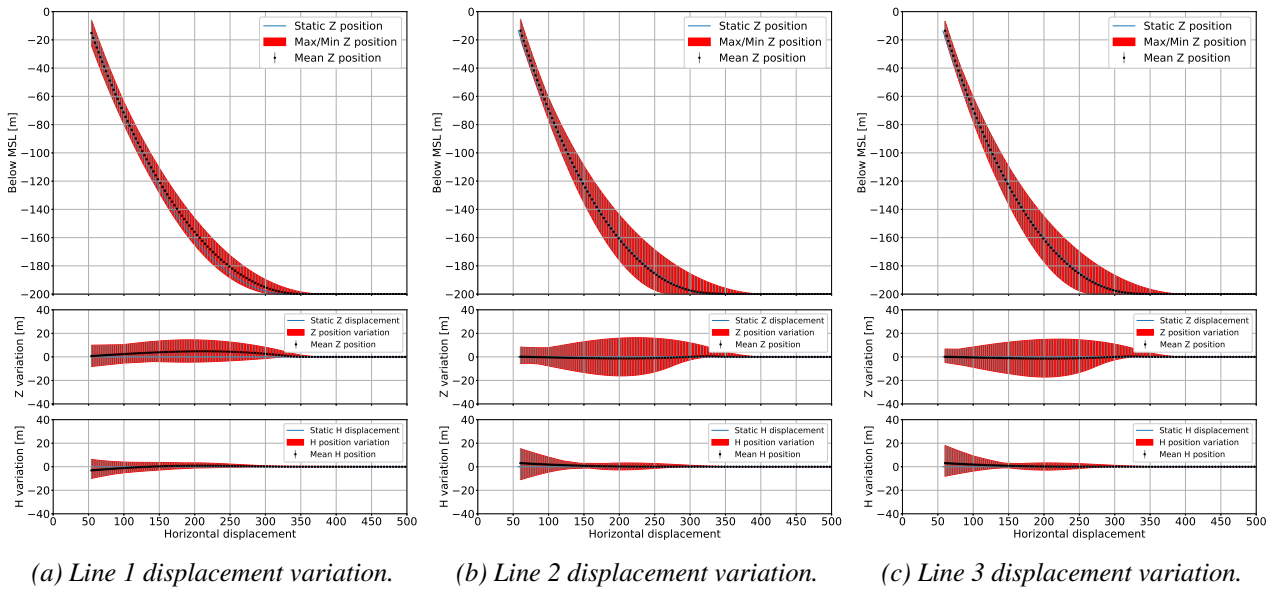


Figure 4.31: MoorDyn mooring line distribution from load case 11.

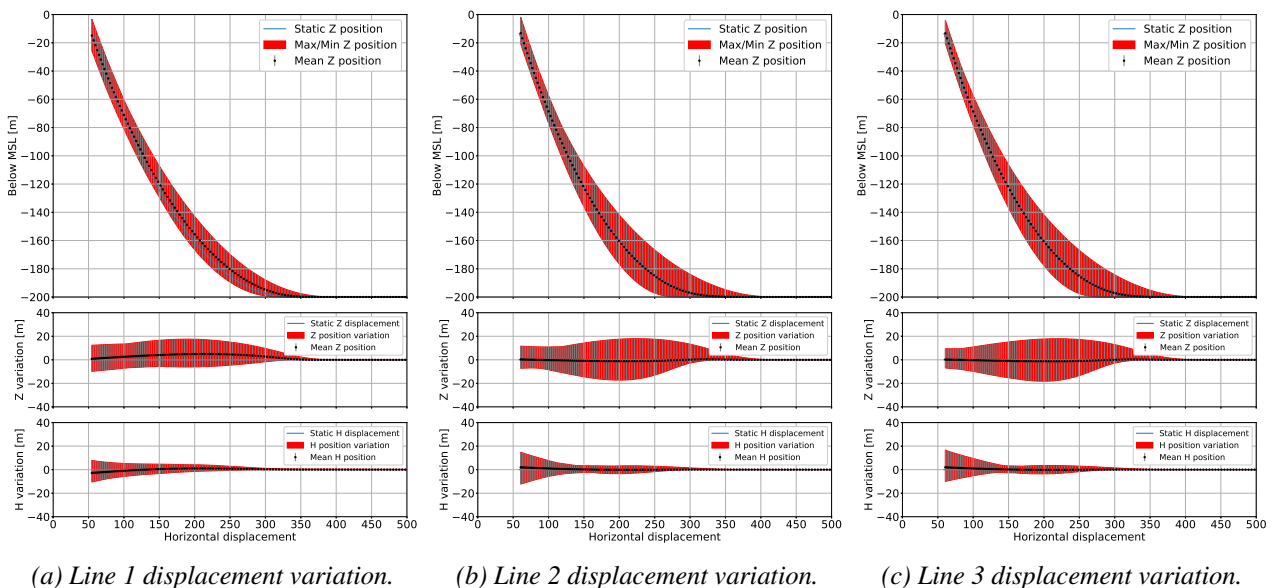


Figure 4.32: ARM mooring line distribution from load case 11.

The positional data for the mooring lines displayed in figures 4.31 and 4.32, shows also for this load case high degree of comparability. It can be observed that mooring lines 2 and 3 experience more movement compared to line 1, as was expected due to the sway motion of the platform.

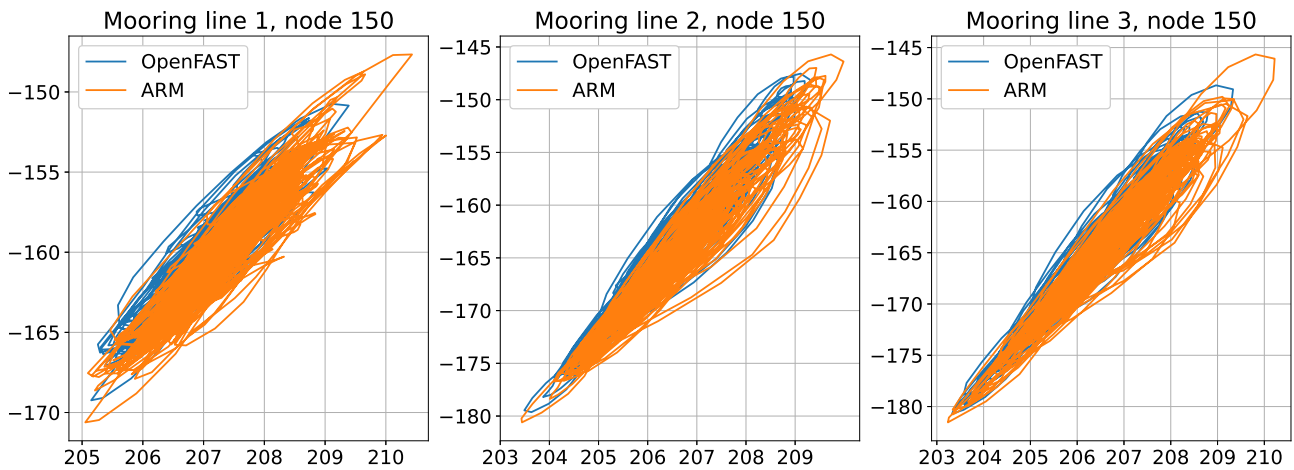


Figure 4.33: Nodal comparison for load case 10, node number 150.

For all three mooring lines, the node 150 movement shows a similar pattern, and the motion seems almost linear. There is very little offset between ARM and OpenFAST nodal position for this node.

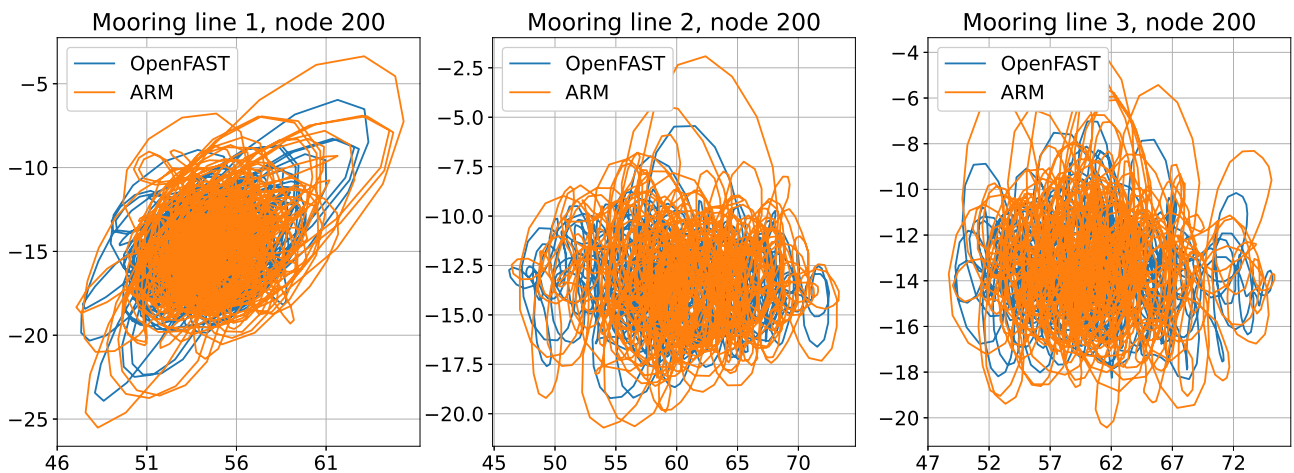


Figure 4.34: Nodal comparison for load case 10, fairlead.

The fairlead motion for all three mooring lines show a circular motion. The nodal comparison shows a high degree of comparability, similar to load case 9 and 10. The nodal motion stays in the same area for both ARM and OpenFAST simulation results.

## Line tension distribution

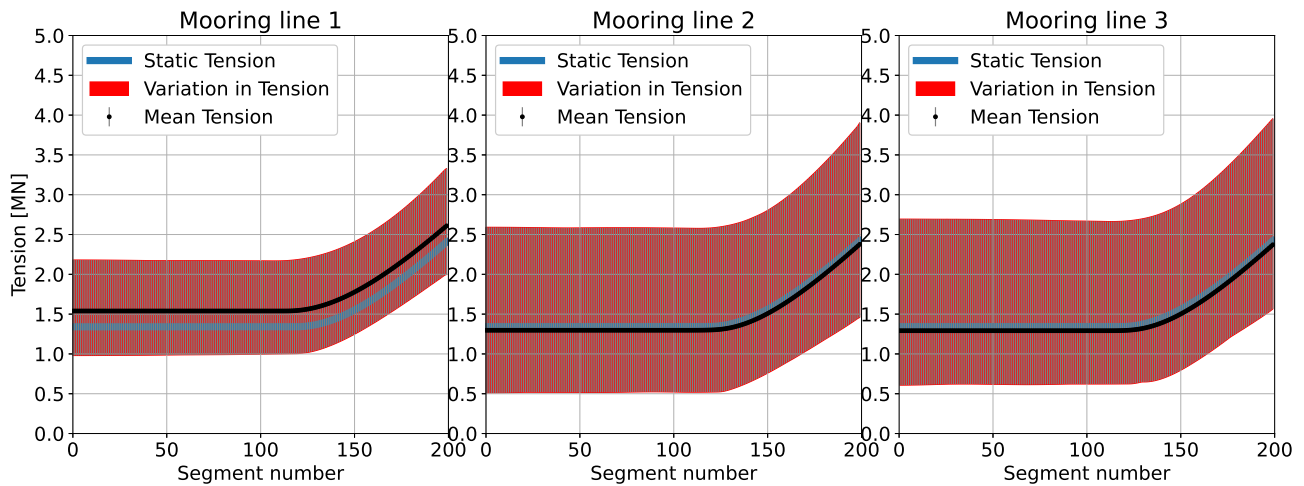


Figure 4.35: OpenFAST line tension variation, lines 1 through 3.

As expected, the tension for mooring line 2 and 3 shows a higher degree of variability, due to the sway motion.

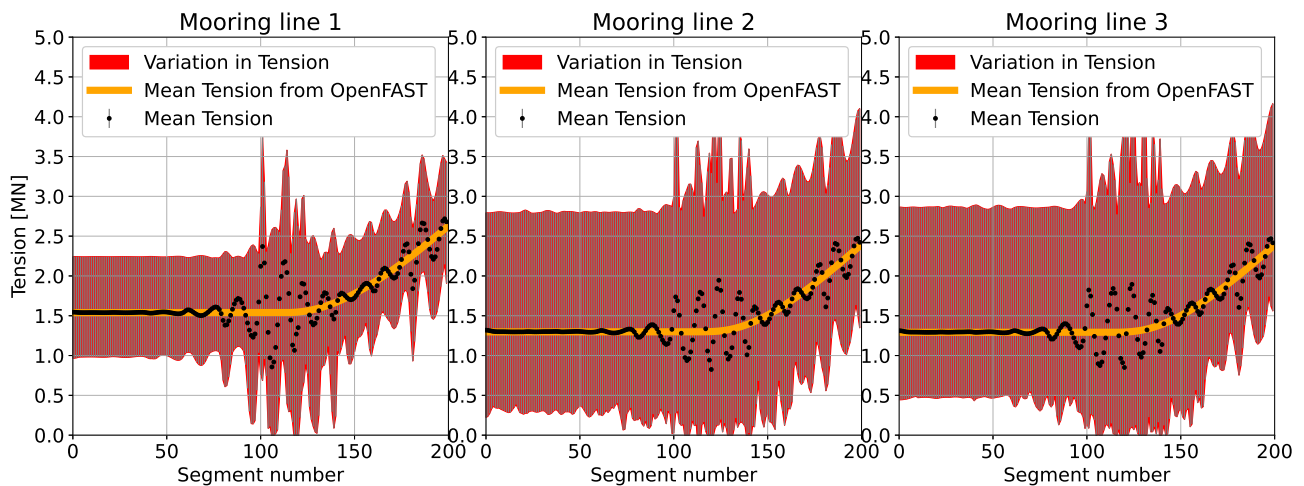


Figure 4.36: ARM line tension variation, lines 1 through 3.

The filtered ARM tension shows a very good comparison with OpenFAST, but the instability around the touchdown point is still a weakness for the new model, and needs to be addressed. The variation of tension for line 1 is the same for both OpenFAST and filtered ARM results. For line 2 and 3, filtered ARM results show a slightly higher variation in tension, with approximately 10% increased variation for the ARM results. This is an interesting observation, but it is difficult to state if this is due to the new advanced rod model capturing closer to real tension results, or if it is due to model instability.

# Chapter 5

## Conclusion and future work

### 5.1 Conclusion

This thesis has studied the potential for using an advanced rod model for mooring line analysis. The continuous development of the model which was carried out in this master thesis, has improved the models capability to act as a mooring line analysis tool. One critical factor which has been introduced is the barrier function, which acts as an impenetrable barrier at the seabed. The barrier function has also been further developed and refined during this thesis. Furthermore, the introduction of the increased polynomial degree and continuity order for the FEM isogeometric discretization has led to improved results, and the observation that the reduced time-step yields a better result for line tension, leading to applying a low-pass filter has also improved the models capabilities. It is important to take care when applying a filter to the results, as the low-pass filter could potentially remove some of the natural behaviour of the tension of a mooring line, and as such mask important results. I believe the best way for tension analysis with the current noise issue would be to run at reduced time-step, even though this will increase the simulation time.

The new ARM dynamic mooring line model developed shows good comparison with OpenFAST MoorDyn for positional data. The offset seen for the node 150 for all the dynamic simulations could be explained by the higher stiffness of the MoorDyn model compared to the new advanced rod model. Though both models use the same modules of elasticity, and both models neglect bending stiffness, the way the lumped parameter model is designed will increase stiffness due to lack of flexibility between the nodes. If the number of nodes had been increased towards infinity, the results from the two models should converge.

When analysing the tension from OpenFAST's MoorDyn mooring simulator, it becomes obvious that the mooring lines are critically damped, which yields a very smooth result for both mean, min and max tension. The ARM model does not have structural damping, only fluid dampening, which yields a more erratic tension results.

The instability of the tension results from ARM makes the current model in my opinion not suited for tension analysis. The oscillation amplitude of the instability reduced as the polynomial degree and continuity order of the FEM discretization was increased, but it was still visible. Also, the position of the instability shifted as the FEM discretization was changed, from node 181 to around touchdown point of the line. Due to this, I believe the instability is a spatial issue rather than a time issue, since it is visible on the mean measurement, and is visible regardless of the time-step of the simulation, and that it shifts position when changing the FEM discretization. It is worth mentioning that as the mean tension is reduced, the instability becomes more dominating. I believe this can be explained by considering a rope with varying tension. With low tension, the rope has high amplitude, but low frequency waves, but as the



tension is increased, the frequency increases, but the amplitudes of the waves are reduced. The low-pass filtering removes the high frequency noise observed on the 10 Hz data, and the filtered results are comparable to the MoorDyn results. The reason behind the instability in tension is not known, but it could be a numerical artifact like shear locking in the FEM analysis method, possibly due to the isogeometric discretization.

I believe that, with some further improvements, this model can be used for mooring line analysis in the future, if the instability issue can be resolved.

Regarding the mooring line results, the number of load cases chosen does not give enough data to give a conclusion for a complete mooring analysis, but in my opinion the mooring setup seems too conservative. Maximum tension seen in the load cases run from any model is 5 MN. In relation to the line breaking strength from table 2.6, this would be 22%. In addition, the closest touchdown point to anchor is for load case 9, line 1, 382m, which in my opinion is more than required. I think there could be potential cost saving for this FWT setup by choosing either a smaller chain diameter or reducing the chain length. Another possibility would be to look into a mixed mooring line with chain-synthetic rope-chain.

## 5.2 Future work

During my work with the use of the new ARM model for mooring lines, I have discovered both weaknesses and strengths with regards to the new model. I think the new model has potential to become a new and improved analysis tool for mooring lines, but there is still issues which needs to be resolved. The instability around the touchdown point, which is especially visible when looking at the stress measures, is in my opinion the main weakness of the current advanced rod model, and this will need to be addressed if ARM is to be used for mooring line analysis. I think more studies are needed to see if a different FEM discretization will improve the results, either by changing the number of control points for the isogeometric discretization, polynomial degree or continuity order, or by changing to a normal FEM discretization using nodes and meshes. I would also suggest to try to implement structural dampening to the new model, as this could help in reducing the models instability, and together with reducing the time-step in the simulation, help to give a better picture of the variation in the mooring line tension. In addition, the use of the barrier function will require some fine tuning, or potentially look into a new way of introducing the interaction between the mooring line and the seafloor.

The new model should also be updated to include ocean current forcing possibilities, and may also look into vortex induced vibrations on the mooring lines as part of the drag force.

To meet the mooring industry's increased interest in synthetic mooring lines, the new model should aim at incorporating the use of hyperelastic materials, and the design of complex mooring lines constituting more than one material.

Finally, I would like to suggest that instead of having the input parameter as force, I would recommend to use the fairlead position and to let the forces in the line be calculated by the model. This will require some reworking of the equations, but will make it easier to incorporate the model into coupled dynamic analysis tools in the future.

# Appendix A

## Mathematical derivation of the new advanced model

In this appendix, I will show the derivation of the Mass operator,  $\mathcal{M}$ , used in the expression of variation of kinetic energy, and the linear Strain operator,  $\mathcal{B}$ , used in the expression of variation of potential energy. Finally, I will show the derivation of the strong and weak form of the equation of motion for the rod.

### A.1 Mass operator

Let us proceed to find the Mass operator,  $\mathcal{M}$ .

$$T = \underbrace{\frac{1}{2} \int_0^L \dot{\boldsymbol{\varphi}} \cdot \dot{\boldsymbol{\varphi}} A_\rho ds}_{\text{Translation energy}} + \underbrace{\frac{1}{2} \int_0^L \dot{\mathbf{d}} \cdot \dot{\mathbf{d}} I_\rho ds}_{\text{Rotation energy}} \quad (\text{A.1})$$

We know that  $\mathbf{d} = \frac{\boldsymbol{\varphi}'}{|\boldsymbol{\varphi}'|}$ , and we need to replace the  $\dot{\mathbf{d}}$  with an expression with  $\boldsymbol{\varphi}$ .

We know that  $|\boldsymbol{\varphi}'| = (\boldsymbol{\varphi}' \cdot \boldsymbol{\varphi}')^{\frac{1}{2}}$ .

We will start by differentiating  $\mathbf{d}$ ,

$$\mathbf{d} = \frac{\boldsymbol{\varphi}'}{|\boldsymbol{\varphi}'|} = \boldsymbol{\varphi}' (\boldsymbol{\varphi}' \cdot \boldsymbol{\varphi}')^{-\frac{1}{2}} \quad (\text{A.2})$$

$$D\mathbf{d} = D\boldsymbol{\varphi}' (\boldsymbol{\varphi}' \cdot \boldsymbol{\varphi}')^{-\frac{1}{2}} + \boldsymbol{\varphi}' \left( -\frac{1}{2} (\boldsymbol{\varphi}' \cdot \boldsymbol{\varphi}')^{-\frac{3}{2}} 2\boldsymbol{\varphi}' \cdot D\boldsymbol{\varphi}' \right) \quad (\text{A.3})$$

$$D\mathbf{d} = (\boldsymbol{\varphi}' \cdot \boldsymbol{\varphi}')^{-\frac{1}{2}} \left[ I - \frac{\boldsymbol{\varphi}' \otimes \boldsymbol{\varphi}'}{(\boldsymbol{\varphi}' \cdot \boldsymbol{\varphi}')^{\frac{1}{2}} (\boldsymbol{\varphi}' \cdot \boldsymbol{\varphi}')^{\frac{1}{2}}} \right] D\boldsymbol{\varphi}' \quad (\text{A.4})$$

$$D\mathbf{d} = \frac{I - \mathbf{d} \otimes \mathbf{d}}{|\boldsymbol{\varphi}'|} D\boldsymbol{\varphi}' \quad (\text{A.5})$$

$$\dot{\mathbf{d}} = \frac{d}{dt} \mathbf{d} = \frac{I - \mathbf{d} \otimes \mathbf{d}}{|\boldsymbol{\varphi}'|} \frac{d}{dt} \partial_s \boldsymbol{\varphi} = \frac{I - \mathbf{d} \otimes \mathbf{d}}{|\boldsymbol{\varphi}'|} \partial_s \dot{\boldsymbol{\varphi}} \quad (\text{A.6})$$

$$\dot{\mathbf{d}} \cdot \dot{\mathbf{d}} = \left( \frac{I - \mathbf{d} \otimes \mathbf{d}}{|\boldsymbol{\varphi}'|} \partial_s \dot{\boldsymbol{\varphi}} \right) \cdot \left( \frac{I - \mathbf{d} \otimes \mathbf{d}}{|\boldsymbol{\varphi}'|} \partial_s \dot{\boldsymbol{\varphi}} \right). \quad (\text{A.7})$$

Let us call  $\frac{I-\mathbf{d}\otimes\mathbf{d}}{|\varphi'|}$  for matrix  $\mathbf{A}$ , and  $\mathbf{I}\partial s$  for matrix  $\mathbf{B}$ . Then we can write equation A.7 as,

$$\dot{\mathbf{d}} \cdot \dot{\mathbf{d}} = (\mathbf{A}\mathbf{B}\dot{\varphi}) \cdot (\mathbf{A}\mathbf{B}\dot{\varphi}) = (\mathbf{A}\mathbf{B}\dot{\varphi})^T (\mathbf{A}\mathbf{B}\dot{\varphi}) = \dot{\varphi} \cdot (\mathbf{B}^T \mathbf{A}^T \mathbf{A} \mathbf{B} \dot{\varphi}) \quad (\text{A.8})$$

$$\mathbf{A} = \mathbf{A}^T, \text{ and } \mathbf{B}^T = \partial s^T \quad (\text{A.9})$$

$$\mathbf{A}^T \mathbf{A} = \left( \frac{I-\mathbf{d}\otimes\mathbf{d}}{|\varphi'|} \right) \left( \frac{I-\mathbf{d}\otimes\mathbf{d}}{|\varphi'|} \right) = \frac{I-\mathbf{d}\otimes\mathbf{d}}{|\varphi'|^2} \quad (\text{A.10})$$

this comes from:  $(\mathbf{a}\otimes\mathbf{b})(\mathbf{c}\otimes\mathbf{d}) = (\mathbf{a}\otimes\mathbf{d})(\mathbf{b}\cdot\mathbf{c})$ , and since  $\mathbf{d}\cdot\mathbf{d} = 1$  by definition

$$\dot{\mathbf{d}} \cdot \dot{\mathbf{d}} = \dot{\varphi} \cdot \left[ \partial s^T \left( \frac{I-\mathbf{d}\otimes\mathbf{d}}{|\varphi'|^2} \partial s \dot{\varphi} \right) \right]. \quad (\text{A.11})$$

Then we can use this expression for  $\dot{\mathbf{d}} \cdot \dot{\mathbf{d}}$  in the rotation energy part,

$$T = \underbrace{\frac{1}{2} \int_0^L \dot{\varphi} \cdot \dot{\varphi} A_\rho ds}_{\text{Translation energy}} + \underbrace{\frac{1}{2} \int_0^L \dot{\mathbf{d}} \cdot \dot{\mathbf{d}} I_\rho ds}_{\text{Rotation energy}} \quad (\text{A.12})$$

$$T = \frac{1}{2} \int_0^L \left[ \dot{\varphi} \cdot (A_\rho \mathbf{I}) \dot{\varphi} + \dot{\varphi} \cdot \left( I_\rho \partial s^T \left( \frac{I-\mathbf{d}\otimes\mathbf{d}}{|\varphi'|^2} \right) \partial s \right) \dot{\varphi} \right] dl \quad (\text{A.13})$$

$$T = \frac{1}{2} \int_0^L \dot{\varphi} \cdot \underbrace{\left( (A_\rho \mathbf{I}) + I_\rho \partial s^T \left( \frac{I-\mathbf{d}\otimes\mathbf{d}}{|\varphi'|^2} \right) \partial s \right)}_{\text{Mass operator}} \dot{\varphi} dl \quad (\text{A.14})$$

$$\mathcal{M}(\varphi') = \left( (A_\rho \mathbf{I}) + I_\rho \partial s^T \left( \frac{I-\mathbf{d}\otimes\mathbf{d}}{|\varphi'|^2} \right) \partial s \right) \quad (\text{A.15})$$

$$T = \frac{1}{2} \int_0^L \dot{\varphi} \mathcal{M}(\varphi') \dot{\varphi} dl \quad (\text{A.16})$$

. By some advanced mathematical steps, it can be shown that the variation of kinetic energy can be described as follows,

$$\delta \mathbf{T}(\varphi) = \int_0^S \delta \hat{\mathbf{T}}(\dot{\varphi}, \dot{\mathbf{d}}; s) ds \quad (\text{A.17})$$

$$= - \int_0^S \delta \varphi^a \mathcal{M}(\varphi')_{ab} \ddot{\varphi}^b + \hat{\Gamma}(\mathcal{M}(\varphi')_{abc} \dot{\varphi}^b \dot{\varphi}^c) ds \quad (\text{A.18})$$

$$= - \int_0^S \delta \varphi \mathcal{M}(\varphi') \hat{\nabla}_\varphi \dot{\varphi} ds. \quad (\text{A.19})$$

$\hat{\nabla}_\varphi$  is the covariant derivative, while  $a, b$  and  $c$  are indices with values 1, 2 and 3.

## A.2 Strain Operator

Next we will find the strain operator. This will be used in the expression for potential energy. Known facts,

$$\begin{aligned} D\mathbf{d} &= \frac{I-\mathbf{d}\otimes\mathbf{d}}{|\varphi'|} D\varphi', & \mathbf{d}' &= \frac{I-\mathbf{d}\otimes\mathbf{d}}{|\varphi'|} \varphi'' \\ U &= \frac{1}{2} \int_0^L \boldsymbol{\varepsilon} \cdot \boldsymbol{\varepsilon} E A ds + \frac{1}{2} \int_0^L \boldsymbol{\kappa} \cdot \boldsymbol{\kappa} E I ds \\ \boldsymbol{\varepsilon} &= \varphi' - \frac{\varphi'}{|\varphi'|} = \varphi' - \mathbf{d}, & \mathbf{d} &= \frac{\varphi'}{|\varphi'|}, & \boldsymbol{\kappa} &= \mathbf{d} \times \mathbf{d}'. \end{aligned} \quad (\text{A.20})$$

I will proceed to find  $\delta\varepsilon$ ,

$$D\varepsilon = D\varphi' - Dd = D\varphi' \left( \mathbf{I} - \frac{\mathbf{I} - \mathbf{d} \otimes \mathbf{d}}{|\varphi'|} \right). \quad (\text{A.21})$$

Next I will find an expression for  $\kappa \cdot \kappa$ ,

$$\kappa \cdot \kappa = (\mathbf{d} \times \mathbf{d}') \cdot (\mathbf{d} \times \mathbf{d}') = \mathbf{d}' \cdot \mathbf{d}'. \quad (\text{A.22})$$

Here I have used the identity,

$$(\mathbf{a} \times \mathbf{b}) \cdot (\mathbf{c} \times \mathbf{d}) = (\mathbf{a} \cdot \mathbf{c})(\mathbf{b} \cdot \mathbf{d}) - (\mathbf{a} \cdot \mathbf{d})(\mathbf{b} \cdot \mathbf{c}), \text{ thus} \quad (\text{A.23})$$

$$(\mathbf{d} \times \mathbf{d}') \cdot (\mathbf{d} \times \mathbf{d}') = (\mathbf{d} \cdot \mathbf{d})(\mathbf{d}' \cdot \mathbf{d}') - (\mathbf{d} \cdot \mathbf{d}')(\mathbf{d} \cdot \mathbf{d}') \quad (\text{A.24})$$

$$\text{and since } \mathbf{d} \cdot \mathbf{d} = 1 \text{ by definition, and } \mathbf{d} \text{ is orthogonal to } \mathbf{d}' \longrightarrow \mathbf{d} \cdot \mathbf{d}' = 0 \quad (\text{A.25})$$

$$= \mathbf{d}' \cdot \mathbf{d}'. \quad (\text{A.26})$$

I want to find  $\delta U$ , and  $\delta U = \frac{1}{2}EA \int \delta\varepsilon \cdot \varepsilon dl + \frac{1}{2}EI \int \delta\kappa \cdot \kappa dl$ .

$$\delta\kappa = \delta(\mathbf{d} \times \mathbf{d}') = \delta\mathbf{d} \times \mathbf{d}' + \mathbf{d} \times \delta\mathbf{d}' = -\mathbf{d}' \times \delta\mathbf{d} + \mathbf{d} \times \delta\mathbf{d}'$$

What remains is to express  $D\mathbf{d}'$  by means of  $\varphi$ ,

$$\delta\kappa \cdot \kappa = \delta\mathbf{d}' \cdot \mathbf{d}', \text{ and } \mathbf{d}' = \frac{\mathbf{I} - \mathbf{d} \otimes \mathbf{d}}{|\varphi'|} \varphi'' \quad (\text{A.27})$$

$$\mathbf{d}' = \underbrace{(\mathbf{I} - \mathbf{d} \otimes \mathbf{d})}_{\mathbf{A}} \underbrace{(\varphi \cdot \varphi)^{-\frac{1}{2}}}_{\mathbf{B}} \underbrace{(\varphi'')}_{\mathbf{C}} \quad (\text{A.28})$$

$$D\mathbf{d}' = (D\mathbf{A})(\mathbf{B}\mathbf{C}) + \mathbf{A}(D\mathbf{B})\mathbf{C} + \mathbf{A}\mathbf{B}(D\mathbf{C}) \quad (\text{A.29})$$

$$D\mathbf{A} = (0 - D(\mathbf{d} \otimes \mathbf{d})) \quad (\text{A.30})$$

$$D(\mathbf{d} \otimes \mathbf{d})\mathbf{B}\mathbf{C} = (D\mathbf{d} \otimes \mathbf{d} + \mathbf{d} \otimes D\mathbf{d})\mathbf{B}\mathbf{C} \quad (\text{A.31})$$

$$(\mathbf{a} \otimes \mathbf{b})\mathbf{c} = (\mathbf{b} \cdot \mathbf{c})\mathbf{a} = (\mathbf{c} \cdot \mathbf{b})\mathbf{a} = (\mathbf{a} \otimes \mathbf{c})\mathbf{b} \text{ (Identity)} \quad (\text{A.32})$$

$$(D\mathbf{d} \otimes \mathbf{d} + \mathbf{d} \otimes D\mathbf{d})\mathbf{B}\mathbf{C} = (\mathbf{d} \cdot \mathbf{B}\mathbf{C})D\mathbf{d} + (\mathbf{d} \otimes \mathbf{B}\mathbf{C})D\mathbf{d} = \left[ (\mathbf{d} \cdot \mathbf{B}\mathbf{C})\mathbf{I} + \mathbf{d} \otimes \mathbf{B}\mathbf{C} \right] D\mathbf{d} \quad (\text{A.33})$$

$$\begin{aligned} (D\mathbf{A})\mathbf{B}\mathbf{C} &= - \left[ \left( \mathbf{d} \cdot \frac{\varphi''}{|\varphi'|} \right) \mathbf{I} + \mathbf{d} \otimes \frac{\varphi''}{|\varphi'|} \right] \left[ \frac{\mathbf{I} - \mathbf{d} \otimes \mathbf{d}}{|\varphi'|} D\varphi' \right] \\ &= - \frac{1}{|\varphi'|^2} \left[ (\mathbf{d} \cdot \varphi'')\mathbf{I} + \mathbf{d} \otimes \varphi'' \right] [\mathbf{I} - \mathbf{d} \otimes \mathbf{d}] D\varphi' \end{aligned} \quad (\text{A.34})$$

$$D\mathbf{B} = -\frac{1}{2}(\varphi' \cdot \varphi')^{-\frac{3}{2}} 2\varphi' D\varphi' = -\frac{\varphi' \cdot D\varphi'}{|\varphi'|^3}$$

$$\begin{aligned} (D\mathbf{B})\mathbf{A}\mathbf{C} &= \left( -\frac{\varphi' \cdot D\varphi'}{|\varphi'|^3} \right) (\mathbf{I} - \mathbf{d} \otimes \mathbf{d})(\varphi'') = -\frac{1}{|\varphi'|^2} (\mathbf{d} \cdot D\varphi') (\mathbf{I} - \mathbf{d} \otimes \mathbf{d}) \varphi'' \\ &= -\frac{1}{|\varphi'|^2} ((\mathbf{I} - \mathbf{d} \otimes \mathbf{d})\varphi'') \otimes \mathbf{d} D\varphi' \end{aligned} \quad (\text{A.35})$$

$$D\mathbf{C} = D\varphi''$$

$$\mathbf{A}\mathbf{B}(D\mathbf{C}) = \left( \frac{\mathbf{I} - \mathbf{d} \otimes \mathbf{d}}{|\varphi'|} \right) D\varphi''. \quad (\text{A.36})$$

With this expression, I can proceed to put it all together, and simplifying the equation yields,

$$\begin{aligned}
D\mathbf{d}' &= -\frac{1}{|\varphi'|^2} \left[ \left[ (\mathbf{d} \cdot \varphi'') \mathbf{I} + \mathbf{d} \otimes \varphi'' \right] [\mathbf{I} - \mathbf{d} \otimes \mathbf{d}] + ((\mathbf{I} - \mathbf{d} \otimes \mathbf{d}) \varphi'') \otimes \mathbf{d} \right] D\varphi' + \left( \frac{\mathbf{I} - \mathbf{d} \otimes \mathbf{d}}{|\varphi'|} \right) D\varphi'' \\
&= -\frac{1}{|\varphi'|^2} \left[ (\mathbf{d} \otimes \nabla_{\mathbf{d}'}(\varphi') + \nabla_{\mathbf{d}'}(\varphi') \otimes \mathbf{d}) + ((\mathbf{d} \cdot \varphi'') \mathbf{I})(\mathbf{I} - \mathbf{d} \otimes \mathbf{d}) \right] D\varphi' + \left( \frac{\mathbf{I} - \mathbf{d} \otimes \mathbf{d}}{|\varphi'|} \right) D\varphi'' \\
&= -\frac{1}{|\varphi'|^2} \left[ 2(\nabla_{\mathbf{d}'}(\varphi') \odot \mathbf{d}) + ((\mathbf{d} \cdot \varphi'') \mathbf{I})(\mathbf{I} - \mathbf{d} \otimes \mathbf{d}) \right] D\varphi' + \left( \frac{\mathbf{I} - \mathbf{d} \otimes \mathbf{d}}{|\varphi'|} \right) D\varphi''. \quad (\text{A.37})
\end{aligned}$$

Next is to find  $\delta\kappa$ ,

$$\delta\kappa = -\mathbf{d}' \times \delta\mathbf{d} + \mathbf{d} \times \delta\mathbf{d}' \quad (\text{A.38})$$

$$\begin{aligned}
D\mathbf{d} &= \frac{\mathbf{I} - \mathbf{d} \otimes \mathbf{d}}{|\varphi'|} D\varphi', \quad \mathbf{d}' = \frac{\mathbf{I} - \mathbf{d} \otimes \mathbf{d}}{|\varphi'|} \varphi'' \\
\delta\kappa &= -\left( \frac{\mathbf{I} - \mathbf{d} \otimes \mathbf{d}}{|\varphi'|} \varphi'' \right) \times \left( \frac{\mathbf{I} - \mathbf{d} \otimes \mathbf{d}}{|\varphi'|} D\varphi' \right) + \\
&\quad \mathbf{d} \times \left( -\frac{1}{|\varphi'|^2} \left[ 2(\nabla_{\mathbf{d}'}(\varphi') \odot \mathbf{d}) + ((\mathbf{d} \cdot \varphi'') \mathbf{I})(\mathbf{I} - \mathbf{d} \otimes \mathbf{d}) \right] D\varphi' + \left( \frac{\mathbf{I} - \mathbf{d} \otimes \mathbf{d}}{|\varphi'|} \right) D\varphi'' \right) \\
\delta\kappa &= -\frac{1}{|\varphi'|^2} [(\mathbf{I} - \mathbf{d} \otimes \mathbf{d}) \varphi''] \times [(\mathbf{I} - \mathbf{d} \otimes \mathbf{d}) D\varphi'] + \mathbf{d} \times \left( -\frac{1}{|\varphi'|^2} \left[ 2(\nabla_{\mathbf{d}'}(\varphi') \odot \mathbf{d}) + ((\mathbf{d} \cdot \varphi'') \mathbf{I})(\mathbf{I} - \mathbf{d} \otimes \mathbf{d}) \right] \right. \\
&\quad \left. \mathbf{d} \times \left( \frac{\mathbf{I} - \mathbf{d} \otimes \mathbf{d}}{|\varphi'|} \right) D\varphi'' \right) \\
&= -\frac{1}{|\varphi'|^2} (\varphi'' \times [(\mathbf{I} - \mathbf{d} \otimes \mathbf{d}) D\varphi']) - \frac{1}{|\varphi'|^2} \mathbf{d} \times \left( 2(\nabla_{\mathbf{d}'}(\varphi') \odot \mathbf{d}) D\varphi' \right) + \mathbf{d} \times \left( \frac{\mathbf{I} - \mathbf{d} \otimes \mathbf{d}}{|\varphi'|} \right) D\varphi'' \\
&= -\frac{1}{|\varphi'|^2} \left[ \varphi'' \times [(\mathbf{I} - \mathbf{d} \otimes \mathbf{d}) + \mathbf{d} \times (2(\nabla_{\mathbf{d}'}(\varphi') \odot \mathbf{d}))] \right] D\varphi' + \frac{1}{|\varphi'|^2} \mathbf{d} \times \left( \frac{\mathbf{I} - \mathbf{d} \otimes \mathbf{d}}{|\varphi'|} \right) D\varphi''. \quad (\text{A.39})
\end{aligned}$$

I can then define the linear strain operator  $\mathcal{B}(\varphi', \varphi'')$ ,

$$\mathcal{B}(\varphi', \varphi'') \delta\varphi = \begin{bmatrix} \delta\varepsilon \\ \delta\kappa \end{bmatrix} \quad (\text{A.40})$$

$$\mathcal{B}(\varphi', \varphi'') = \begin{bmatrix} \mathbf{I} - \frac{\mathbf{I} - \mathbf{d} \otimes \mathbf{d}}{|\varphi'|} & 0 \\ -\frac{1}{|\varphi'|^2} \left[ [\varphi'']_x [(\mathbf{I} - \mathbf{d} \otimes \mathbf{d}) + [\mathbf{d}]_x (2(\nabla_{\mathbf{d}'}(\varphi') \odot \mathbf{d}))] \right] & [\mathbf{d}]_x \frac{\mathbf{I} - \mathbf{d} \otimes \mathbf{d}}{|\varphi'|} \end{bmatrix} \begin{Bmatrix} \mathcal{D}_1 \\ \mathcal{D}_2 \end{Bmatrix}. \quad (\text{A.41})$$

Equation A.41 introduces the two differential operators  $\mathcal{D}_1$  and  $\mathcal{D}_2$  which refers to  $\mathcal{D}_\alpha = \frac{\partial \alpha}{\partial s^\alpha}$ , where  $\alpha = 1, 2$ . With the strain operator defined, the potential energy equation can be rewritten as follows,

$$U = \frac{1}{2} \int_0^L \varepsilon \cdot \varepsilon E A ds + \frac{1}{2} \int_0^L \kappa \cdot \kappa E I ds \quad (\text{A.42})$$

$$DU(\varphi) \cdot \delta\varphi = \int_0^S \delta\tilde{U}(\varepsilon, \kappa) ds \quad (\text{A.43})$$

$$= \int_0^S \delta\varphi \cdot (\mathcal{B}(\varphi', \varphi'')^T \sigma) ds. \quad (\text{A.44})$$

### A.3 Equation of motion

From equations 3.28 and 3.29 we can derive the equation of motion for the system based on the principles of Lagrangian and action integral. I will use the mass operator and strain operator in the kinetic and potential energy expressions. The derivation is as follows,

$$\mathcal{J}[\varphi] = \int_0^T \mathcal{L}[\varphi, \dot{\varphi}] dt \quad (\text{A.45})$$

$$\delta \mathcal{J} = \int_0^T \delta \mathcal{L}[\varphi, \dot{\varphi}] dt = 0, \quad \text{where} \quad \delta \mathcal{L} = \delta T - \delta U \quad (\text{A.46})$$

$$\delta T = - \int_0^S \delta \varphi \cdot \mathcal{M}(\varphi') \hat{\nabla}_{\dot{\varphi}} \dot{\varphi} ds \quad \text{and} \quad \delta U = \int_0^S \delta \varphi \cdot (\mathcal{B}(\varphi', \varphi'')^T \sigma) ds \quad (\text{A.47})$$

$$\delta \mathcal{L}[\varphi, \dot{\varphi}] = \int_0^S \delta \varphi \cdot \left( \mathcal{M}(\varphi') \hat{\nabla}_{\dot{\varphi}} \dot{\varphi} + \mathcal{B}(\varphi', \varphi'')^T \sigma \right) ds \quad (\text{A.48})$$

After some advanced mathematical steps, proven in *Romero and Gebhardt (2020)*, it can be shown that the strong form of the EoM becomes,

$$\int_0^T \delta \mathcal{L}[\varphi, \dot{\varphi}] dt = 0 \quad (\text{A.49})$$

$$\int_0^T \left[ \int_0^S \delta \varphi \cdot \left( \mathcal{M}(\varphi') \hat{\nabla}_{\dot{\varphi}} \dot{\varphi} + \mathcal{B}(\varphi', \varphi'')^T \sigma \right) ds \right] dt = 0 \quad (\text{A.50})$$

$$\text{and since } \delta[\varphi](s, 0) = \delta[\varphi](s, T) = 0 \quad (\text{A.51})$$

$$\int_0^S \delta \varphi \cdot \left( \mathcal{M}(\varphi') \hat{\nabla}_{\dot{\varphi}} \dot{\varphi} + \mathcal{B}(\varphi', \varphi'')^T \sigma \right) ds = 0. \quad (\text{A.52})$$

From the variational equation A.52, the strong form of EoM for the Kirchhoff rod can be recovered,

$$\mathbf{n}' + \left( \frac{1}{|\varphi'|} \mathbf{d} \times \nabla_{\mathbf{d}'} \mathbf{m} \right)' = \dot{\mathbf{p}} + \left( \frac{1}{|\varphi'|} \mathbf{d} \times \nabla_{\mathbf{d}} \pi \right)'. \quad (\text{A.53})$$

# Appendix B

## OpenFAST

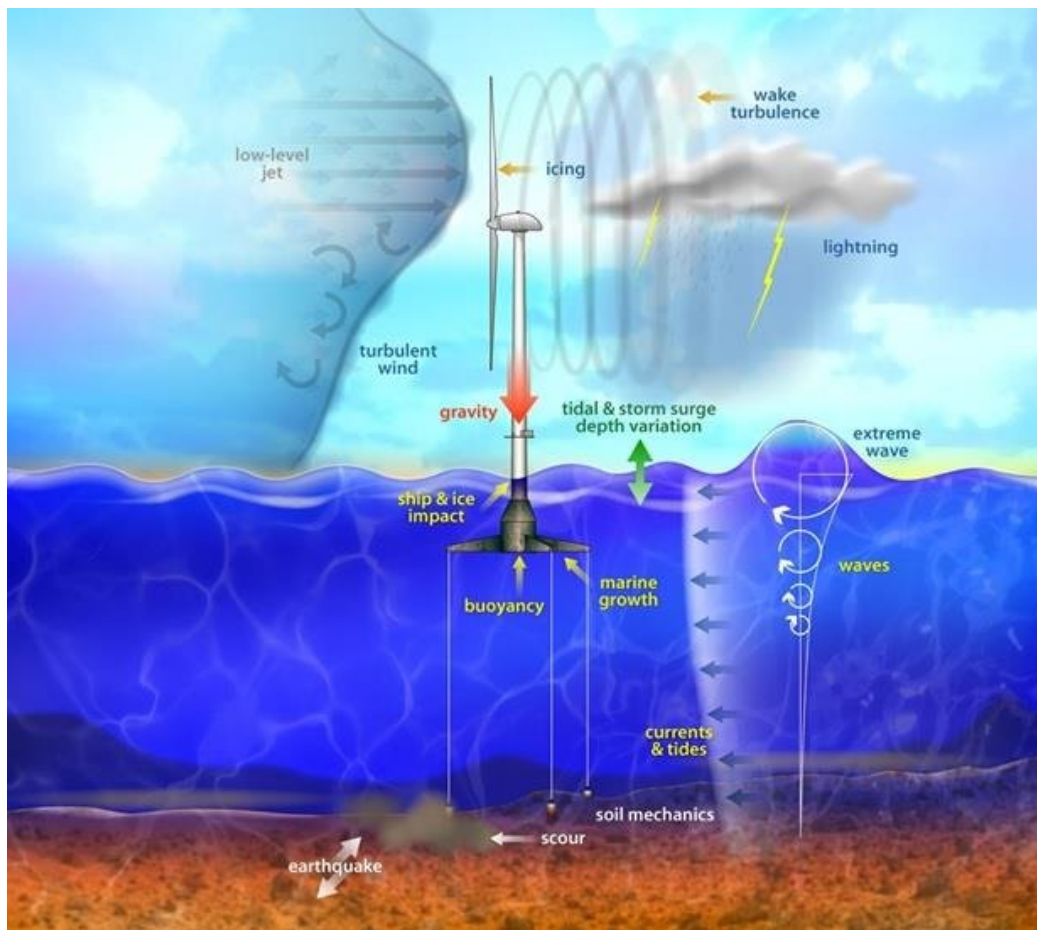


Figure B.1: Sketch of OpenFAST capabilities, courtesy of NREL

OpenFAST (Fatigue, Aerodynamics, Structures, and Turbulence) software is an open source code. It is a comprehensive aeroelastic simulator. It is capable of predicting both the extreme and fatigue loads of two- and three-bladed horizontal-axis wind turbines (HAWTs). It consists of several modules, each with a different purpose. Below I give a brief overview of the filestructure of the modules in OpenFAST.

## B.1 Filestructure for OpenFAST simulation

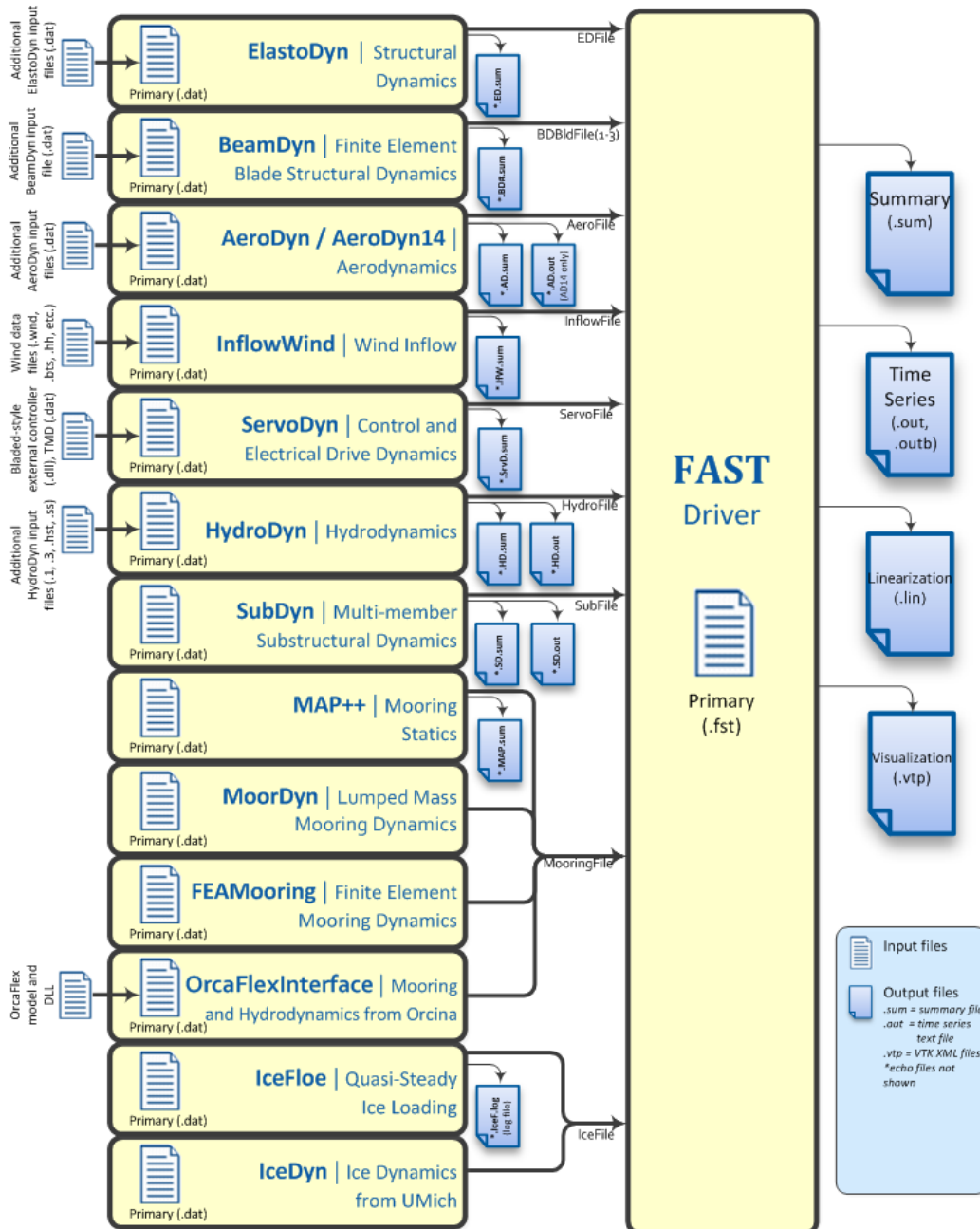


Figure B.2: Flow diagram of the filestructure and modules of OpenFAST, courtesy of NREL

The glue-code is controlled by the .fst file.

- .fst Contains:
  - Simulation control
  - Feature switches and flags (Selection for simulations to be performed)
    - \* ElastoDyn, Inflow, AeroDyn, ServoDyn, HydroDyn, SubDyn, MoorDyn, ComPice, MHK
  - Environmental conditions
  - Reference to input files



- Output
- Linearization
- Visualization
- ElastoDyn.dat Input file for CompElast, contains:
  - Simulation control
  - Degrees of Freedom
  - Initial condition
  - Turbine configuration
  - Mass and Inertia
  - Blade Reference to inputfiles for blade properties
  - Rotor-Teeter
  - Drivetrain
  - Furling
  - Tower - Reference to inputfiles for blade properties
  - Output
- BeamDyn.dat Input files for CompElast, contains:
  - Simulation control
  - Geometry parameter Twist etc.
  - Mesh parameter
  - Material parameter reference to input file Beamdyn\_Blade.dat
    - \* Blade parameters
    - \* Damping coeff
    - \* Distributed properties
  - Pitch Actuator parameters
  - Outputs
- Inflow file contains:
  - Simulation control
  - Parameters for steady wind conditions (type 1)
  - Parameters for uniform wind file can refer to file for timeseries (type 2)
  - Parameters for Binary TurbSim Full-Field files (type 3)
  - Parameters for Binary Bladed-style Full-Field files (type 4 or 7)
  - Parameters for HAWC-format binary files (type 5)
  - Scaling parameters for turbulence
  - Mean wind profile parameters
  - Output
- AeroDyn.dat Input file for CompAero, contains:

- General options
- Environmental conditions
- Blade-Element / Momentum theory options (Wakemodel 1 or 2)
- Dynamic Blade-Element / Momentum theory options (Wakemodel 2)
- OLAF cOnvecting LAgrangian Filaments (Free vortex Wake) (Wakemodel 3)
- Beddoes-Leishman Unsteady Airfoil Aerodynamics options (AFAeroMod 2)
- Airfoil information reference to airfoil input files
- Rotor / blade properties reference to AeroDy\_Blade.dat
- Tower influence and Aerodynamics
- Outputs
- ServoDyn.dat Input file for CompServo, contains:
  - Simulation control
  - Pitch control
  - Generator and Torque control
  - Simple variable-speed torque control
  - Simple induction gear
  - Thevenin-equivalent induction generator
  - High-speed shaft brake
  - Nacelle-yaw control
  - Aerodynamic flow control
  - Structural control
  - Cable control
  - Bladed interface reference DLL file for bladed interface
  - Bladed interface torque-speed look-up table
  - Output
- HydroDyn.dat Input file for CompHydro, contains:
  - Environmental conditions
  - Waves
  - 2nd order waves
  - Current
  - Floating platform
    - \* POTFile for potential flow model data
  - 2nd order floating platform forces
  - Platform additional stiffness
  - Axial coefficients
  - Member joints
  - Member cross-section properties

- Simple hydrodynamic coefficients (model 1)
- Depth based hydrodynamic coefficients (model 2)
- Member-based hydrodynamic coefficients (model 3)
- Members
- Filled members
- Marine growth
- Member output list
- Joint output list
- Output
- MoorDyn.dat Input file for CompMooring, contains:
  - Line types
  - Connection properties
  - Line properties
  - Solver options
  - Outputs

# Bibliography

- Allen, C., Viselli, A., Dagher, H., Goupee, A., Gaertner, E., Abbas, N., Hall, M., and Barter, G. (2020), Iea wind tcp task 37: Definition of the umaine volturnus-s reference platform. 2.6.2, 3.1, 4.2, 4.2.1, 4.2.1
- Baccouch, M. (2021), *A Brief Summary of the Finite Element Method for Differential Equations*, IntechOpen, Rijeka, doi:10.5772/intechopen.95423. 2.8.7
- Betz, A. (1920), Das Maximum der theoretisch möglichen Ausnutzung des Windes durch Windmotoren, *Zeitschrift für das gesamte Turbinenwesen*, pp. 307–309. 2.2
- Bhattacharya, S. (2019), Design of foundations for offshore wind turbines (accessed 07.11.2019), *Design of Foundations for Offshore Wind Turbines*, pp. 6p–6w, 697a. 2.1, 2.3.1
- Bjoerni, F. A., Lien, S., and Midtgarden, T. A. (2023), Life Cycle Cost Analysis of a Floating Wind Farm Located in the Norwegian Sea. 1.2
- Dixon, S. L. (1998), Fluid mechanics, thermodynamics of turbomachinery. 2.4
- DNV (2018), Metocean characterization recommended practices for u.s. offshore wind energy. 3.1.1
- DNV (2022), Floating offshore wind: The next five years. (document), 1, 1.1
- DNV RP-C205 (2014), Recommended practice - environmental conditions and environmental loads. 3.4.3
- Equinor (2023), Hywind Tampen, <https://www.equinor.com/energy/hywind-tampen/>, accessed: 2023-08-16. 1, 1.1
- EU Commision (2020), Offshore renewable energy for a climate-neutral europe, [https://energy.ec.europa.eu/topics/renewable-energy/offshore-renewable-energy\\_en/](https://energy.ec.europa.eu/topics/renewable-energy/offshore-renewable-energy_en/), accessed: 2023-11-13. 1
- EU Commission (2018), Eu green deal, [https://commission.europa.eu/strategy-and-policy/priorities-2019-2024/european-green-deal\\_en/](https://commission.europa.eu/strategy-and-policy/priorities-2019-2024/european-green-deal_en/), accessed: 2023-02-07. 1
- FEM Data streamliner, ANSYS (), [https://femds.com/FEM\\_Guidelines/Prevent\\_Shear\\_Locking/](https://femds.com/FEM_Guidelines/Prevent_Shear_Locking/), accessed: 2023-11-01. 2.8.8
- Foroghei, N., Poor, Z. F., and Darvishi, H. (2015), Cumhuriyet Üniversitesi fen fakültesi euler-lagrange equation, *Cumhuriyet University Faculty of Science Science Journal (CSJ)*, 36. 2.8.5

- Gaertner, E., Rinker, J., Sethuraman, L., Anderson, B., Zahle, F., and Barter, G. (2020), IEA Wind TCP Task 37: Definition of the IEA 15 MW Offshore Reference Wind Turbine, pp. 1–44. 2.2.1, 2.6.1, 3
- Gebhardt, C. G., and Romero, I. (2021), On a nonlinear rod exhibiting only axial and bending deformations: mathematical modeling and numerical implementation, *Acta Mechanica*, 232(10), 3825–3847, doi:10.1007/s00707-021-03038-w. 1.2, 1.2, 2.8.1, 3.4, 3.4.2
- Hall, M. (2015), Moordyn user’s guide. 2.7.6
- He, S., and Wang, A. (2021), Time and frequency domain dynamic analysis of offshore mooring, *Journal of Marine Science and Engineering*, 9, doi:10.3390/jmse9070781. 2.7.3
- IEC (2005), 61400-1, wind turbines - part 1: Design requirements reference. 2.6.1, 3.1.1, 3.1.1
- IEC (2009), 61400-3, wind turbines - part 3: Design requirements for offshore wind turbines. 3.1.1
- Jones, D. R., and Ashby, M. F. (2019), *Elastic Moduli*, 31-47 pp., Butterworth-Heinemann, doi:10.1016/B978-0-08-102051-7.00003-8. 2.8.2
- Jonkman, B., and Jonkman, J. (2016), Fast v8.16.00a-bjj. 3.3
- Jonkman, J. M. (2009), Dynamics of offshore floating wind turbines model development and verification, *Wind Energy*, 12(5), 459–492, doi:https://doi.org/10.1002/we.347. 3.3
- Jonkman, J. M., and Buhl Jr, M. L. (2005), Fast user’s guide - updated august 2005. 3.3
- Jonkman, J. M., Hayman, G. J., Jonkman, B. J., and Damiani, R. R. (2015), AeroDyn v15 User’s Guide and Theory Manual, *Renewable Energy*, (March), 46. 2.4, 3.3
- Kirchhoff, G. (1859), Ueber das gleichgewicht und die bewegung eines unendlich dünnen elastischen stabes., *Journal für die reine und angewandte Mathematik*, 56, 285–313. 2.8.1
- Kirchhoff, G. R. (1865), Uber das ziel der naturwissenschaften. (document)
- Leonhardt, E. (1883), Die internationale elektrische ausstellung wien 1883, *WOCHENSCHRIFT DES ÖSTERR. INGENIEUR- UND ARCHITEKTEN-VEREINES*. 1.1
- Lê, V. A. (2019), *Lagrangian mechanics : an advanced analytical approach*, THEi Wiley ebooks, ISTE : Wiley, London, England. 2.8.5
- Ma, K. T., Luo, Y., Kwan, T., and Wu, Y. (2019), Mooring system engineering for offshore structures, *Mooring System Engineering for Offshore Structures*, pp. 1–350, doi:10.1016/C2018-0-02217-3. 2.5, 2.5.2, 2.5.3, 2.7.1, 2.7.2, 2.7.3
- MacCamy, R., and Fuchs, R. (1954), Wave forces on piles: A diffraction theory. 2.4
- Masciola, M., Jonkman, J., and Robertson, A. (2013), Implementation of a multisegmented, quasi-static cable model, *Proceedings of the International Offshore and Polar Engineering Conference, 2013-March*(March), 315–322. 2.7.2, 2.7.6, 3.3
- Morison, J., Johnson, J., and Schaaf, S. (1950), The Force Exerted by Surface Waves on Piles, *Journal of Petroleum Technology*, 2(05), 149–154, doi:10.2118/950149-g. 2.4

- Nguyen, T.-H., Roccia, B. A., Hiemstra, R. R., Gebhardt, C. G., and Schillinger, D. (2023), Nonlinear dynamic analysis of shear- and torsion-free rods using isogeometric discretization, outlier removal and robust time integration. 2.8.8, 3.4.3
- Nielsen, F. G. (2021), *Floating support structures*, UIB. 2.4, 2.4.1, 2.5
- Odfjell (2023), Oceanwind, <https://odfjellocceanwind.com/>, accessed: 2023-11-18. 2.6
- Orcina (2023a), OrcaFlex Documentation, <https://www.orcina.com/webhelp/OrcaFlex/Default.htm/>, accessed: 2023-11-14. 2.7.4
- Orcina (2023b), Environment: Seabed data, <https://www.orcina.com/webhelp/OrcaFlex/Content/html/Environment,Seabeddata.htm>, accessed: 2023-10-25. 2.7.6
- Ørsted (2019), Making green energy affordable, <https://orsted.com/-/media/www/docs/corp/com/explore/making-green-energy-affordable-june-2019.pdf>, accessed: 2023-11-13. 1.1
- Ørsted (2022), Hornsea one, <https://hornseaprojectone.co.uk/>, accessed: 2022-02-23. 1.1
- Pereyra, B., Wendt, F., Robertson, A., and Jonkman, J. (2016), Assessment of first- and second-order wave-excitation load models for cylindrical substructures: Preprint. 2.4
- Pierson, W. J., and Moskowitz, L. (1964), A proposed spectral form for fully developed wind seas based on the similarity theory of s. a. kitaigorodskii, *Journal of Geophysical Research*, 69, 5181–5190, doi:10.1029/JZ069I024P05181. 3.1
- Rao, S. S. (2017), *The finite element method in engineering*, Butterworth-heinemann. 2.8.7
- Ridge, I., Banfield, S., and Mackay, J. (2010), Nylon fibre rope moorings for wave energy converters, doi:10.1109/OCEANS.2010.5663836. 2.8.3
- Roccia, B. A., and Gebhardt, C. G. (2023), On the use of a barrier function in kirchhoff rod formulations to simulate the contact with the seabed internal report-bergen offshore wind centre (bow). 3.4.1, 3.4.2, 3.4.4
- Romero, I., and Gebhardt, C. G. (2020), Variational principles for nonlinear Kirchhoff rods, *Acta Mechanica*, 231(2), 625–647, doi:10.1007/s00707-019-02562-0. 1.2, 1.2, 2.8.1, 3.4.2, A.3
- Sepideh, A. (2020), Jacob Bernoulli’s analyses of the Funicularia problem, *British Journal for the History of Mathematics*, 35(2), 137–161, doi:10.1080/26375451.2020.1741302. 2.5.1
- Silva, L. S., Cazzolato, B., Sergiienko, N. Y., and Ding, B. (2021), Nonlinear dynamics of a floating offshore wind turbine platform via statistical quadratization Mooring, wave and current interaction, *Ocean Engineering*, 236(July), doi:10.1016/j.oceaneng.2021.109471. (document), 2.5
- Spieß, F. (1975), *Joint North Sea Wave Project (JONSWAP) Progress – An Observer’s Report*, OFFICE OF NAVAL RESEARCH LONDON, England. 3.1
- Tran, T. T., and Kim, D. H. (2015), The platform pitching motion of floating offshore wind turbine: A preliminary unsteady aerodynamic analysis, *Journal of Wind Engineering and Industrial Aerodynamics*, 142, 65–81, doi:10.1016/J.JWEIA.2015.03.009. 2.3.2

- Us Energy Information Administration (2022), Levelized costs of new generation resources in the annual energy outlook 2022. 1.2
- Walton, T. S., and Polachek, H. (1960), Calculation of transient motion of submerged cables, *Mathematics of Computation*, 14(69), 27–46. 2.7.5
- WBG ESMAP (2023a), ESMAP Offshore wind, [https://www.esmap.org/esmap\\_offshore-wind](https://www.esmap.org/esmap_offshore-wind), accessed: 2023-01-05. 1.1
- WBG ESMAP, M. (2023b), ESMAP Offshore wind maps, [https://www.esmap.org/esmap\\_offshorewind\\_techpotential\\_analysis\\_maps](https://www.esmap.org/esmap_offshorewind_techpotential_analysis_maps), accessed: 2023-01-05. 1.1
- Wendt, F. F., Andersen, M. T., Robertson, A. N., and Jonkman, J. M. (2016), Verification and validation of the new dynamic mooring modules available in FAST v8, *Proceedings of the International Offshore and Polar Engineering Conference, 2016-January(August)*, 352–363. 2.7.4
- WindEurope (2021), Annual Report 2020, <https://windeurope.org/intelligence-platform/reports/>, accessed: 2023-05-09. 1.1